Electrocatalysts and their Supporting Materials for Proton Exchange Membrane Fuel Cells: Activity and Durability Studies

Permyakova, Anastasia Aleksandrovna

Publication date:
2013

Document Version
Publisher's PDF, also known as Version of record

Technical University of Denmark

Anastasia Aleksandrovna Permyakova

Electrocatalysts and their Supporting Materials for PEM Fuel Cells: Activity and Durability Studies

Department of Energy Conversion and Storage
Ph.D. Thesis, September 2013

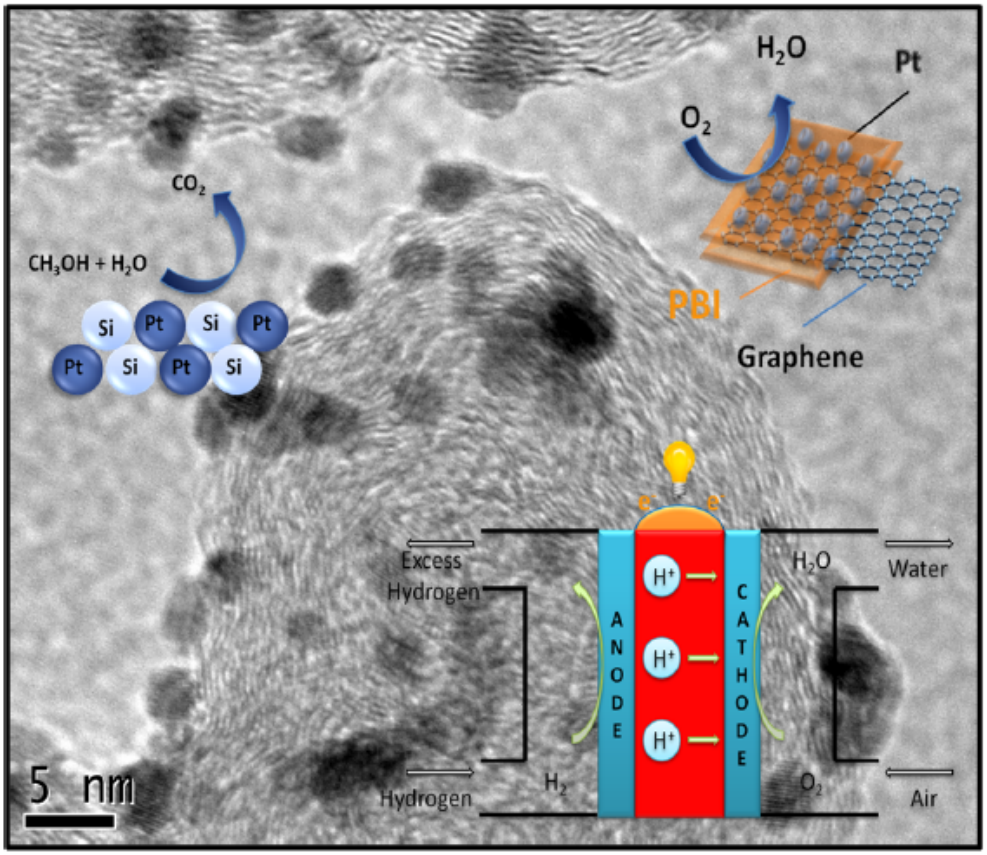

DTU Energy Conversion
Department of Energy Conversion and Storage

Anastasia Aleksandrovna Permyakova

Electrocatalysts and their Supporting Materials for Proton Exchange Membrane Fuel Cells: Activity and Durability Studies

Ph.D. Thesis, September 2013

Submitted in partial fulfilment of the requirements for the degree of Doctor of Philosophy in Chemistry

Electrocatalysts and their Supporting Materials for Proton Exchange Membrane Fuel Cells: Activity and Durability Studies

Author
Anastasia Aleksandrovna Permyakova

Department of Energy Conversion and Storage
Proton Conductors Group
Technical University of Denmark
Kemitorvet buildng 207
DK-2800 Kgs. Lyngby
Denmark

www.energi.kemi.dtu.dk
Tel: (+45) 45 25 23 12
Fax: (+45) 45 88 31 36
E-mail: anper@dtu.dk, anper@mit.edu

1st Edition 2013

Cover illustration
Schematic view of oxygen reduction and methanol oxidation electro-catalysis in PEMFCs, TEM image. © Anastasia A. Permyakova

"О, сколько нам открытий чудных
Готовят просвещенья дух
И опыт, сын ошибок трудных,
И гений, парадоксов друг,
И случай, бог изобретатель."

(1829, опубл. 1884)
Александр Сергеевич Пушкин (1799 - 1837)

"You never change things by fighting the existing reality. To change something, build a new model that makes the existing model obsolete."

Richard Buckminster "Bucky" Fuller (1895 – 1983)

To my mother

Acknowledgements

This thesis presents the work carried out during my PhD studies at the Technical University of Denmark (DTU) under the supervision of Professor Niels J. Bjerrum, Associate Professor Jens Oluf Jensen and Associate Professor Qingfeng Li. The main part of work was done at the Department of Energy Conversion and Storage, Proton conductors group in the time period from March 2010 to August 2013. A significant part of the work was conducted in Massachusetts Institute of Technology (MIT, Cambridge, MA, USA) under the supervision of Professor Yang Shao-Horn, during my research stay as a visiting Ph. D. student in 2012 for two periods (totalling of eight months).

I would like to greatly acknowledge all my supervisors. First of all, Professor Niels J. Bjerrum for giving me the opportunity to work in his group, for his professional and wisdom guidance and for his efforts in helping me successfully complete the PhD program.

I would like to thank my co-supervisor, Head of Proton Conductors Section, Associate Professor Jens Oluf Jensen for always taking the time for discussions, his inspiration and great enthusiasm in the field of science and for always supporting me in my (sometimes unrealistic) research plans and ideas. Also, I would like to thank him for his daily support and immense kindness during the difficult times.

I would also like to thank Associate Professor Qingfeng Li for taking on the responsibility of being my co-supervisor, for giving his valuable feedback on my research and writing, and for providing challenging ideas.

I am especially grateful to Professor Yang Shao-Horn for welcoming me in her group - The Electrochemical Energy Laboratory (EEL) at MIT, for her great influence on my research and scientific development in the field of electrochemical energy and for providing me with the opportunity to study together with highly experienced professionals in the field.

Throughout the whole work period, a great amount of input was obtained from collaboration with colleagues and friends from DTU, MIT and other places.

I would like to thank visiting student Kaiti Zolton, from Case Western Reserve University and Maria Teresa Romero Sánchez from Danish Power Systems for their assistance with some of the experimental work in Chapter 3.

I would like to thank MIT graduate student Alex Binghong Han, who helped me with experimental and data analysis (particularly with XPS) in Chapter 4, who is also an equal contributor to our paper based on the chapter.

I would like to thank PhD student Anne-Charlotte Johansson from DTU Nanotech for providing me with ALD deposited Pt film samples as discussed in Chapter 5.

I would like to thank Lektor Irina Petrushina (DTU Energy Conversion) and Professor. Marcel A. J. Somers (DTU Mechanical Engineering) whose innovative spirit led to the contribution of a number of great ideas.

I would like to thank Professor Nini Pryds (DTU Energy Conversion) for introducing to the arc-melting process.

I would like to thank Research Specialist Dr. Scott Speakman from the Center for Materials Science and Engineering for assistance with the X-ray diffraction measurements during my time at MIT.

I would like to thank my colleagues and friends from the EEL group at MIT, namely: Dr. Jin Suntivich, Dr. Seung Woo Lee, Dr. Zhichuan Xu, Dr. Tian Ming, Dr. Yi-Chun Lu, Dr. Lei Wang, Kevin May, Kelsey Stoerzinger and Jennifer Sell - for providing new ideas and collaboration. Dr. Marcel Risch - for his kind assistance with Raman measurements, Dr. Alexis Grimaud - for fruitful discussions, and Professor Yu-ju Lin - thank you guys for your friendship. It was a very exiting journey, full of inspiration and great experience.

I warmly thank all current and former PhD students and personnel of the Proton Conductors Section, DTU Energy conversion for always been there to help and for creating a good working atmosphere, especially: Kirsten Munkgaard Thomsen, Dr. Lars Nilausen Cleemann, Claus Burke Mortensen and Chao Pan; Dr. Martin Kalmar Hansen - for his sarcastic vision of life; Anton Vassiliev - for been perfect officemate, Tatiana Anfimova and Dr. Yury Y. Gorbanev - for fun get-togethers; Antonio Luis Tomás García - for being a great friend, providing active advices and durable support.

Lastly but most importantly, I would love to thank my mother Nina Vladimirovna Permyakova and my grandmother Dina Agaphonovna Bilibina for their selfless love, support and patience through all these years. They have giving the most but asked the least for return. Thank you for the encouraging my desire of knowledge and adventure.

Anastasia Aleksandrovna Permyakova
DTU, Copenhagen, September 23, 2013

Abstract

This thesis describes investigations conducted exploring the activity, stability and durability of supported nano-particulate, bulk and thin film electrocatalysts used in proton exchange membrane fuel cells (PEMFCs). The effects of different factors and conditions on the reactions involved in oxygen reduction, carbon monoxide and methanol electro-oxidation reactions were explored. Employed catalysts were characterized electrochemically and physiochemically using techniques such as: cyclic voltammetry, rotating disk electrode technique, SEM, TEM, EDS, XPS, TGA/DTA, Raman, XRD, FTIR-IR among other methods.

The thesis begins with an introduction in Chapter 1 providing an overview of fuel cells, their associated reaction mechanisms, catalysts and catalysts supports.

Chapter 2 presents the theoretical background to the study including equipment and the techniques used to analyse the catalysts. Subsequently examples of electrochemical characterization for electrochemical surface area are given followed by a description of rotation disk electrode (RDE) principles and set-up. Next the determination of oxygen reduction activity and carbon monoxide electro-oxidation voltammetry are described in addition to long-term durability procedures.

A significant part of the PhD study involved development of electrochemical instrumentation and techniques, such as: RDE and set-up, oxygen reduction, methanol and CO electro-oxidation, long-term durability procedures, etc. The techniques employed by the author were self-taught or learnt by working with experienced collaborators during the first years of the PhD study. In the advanced stages of the project these techniques were employed by the DTU Proton Conductor group on a daily basis.

In addition the author attained a high level of proficiency in operating the following instruments: TEM (FEI Tecnai T20 G2), EDS, AFM, XRD (PANalytical Multipurpose Diffractometer) and FTIR-IR.

Chapter 3 describes the results of synthesis and testing of the Pt nanoparticulate catalyst supported by PBI wrapped Graphene for oxygen reduction reaction in PEMFCs. The physiochemical material's characterisation, preparation procedures for thin film RDE electrodes, catalyst's ink composition, oxygen reduction reaction activity, electrochemical surface area and durability studies are also described in detail.

Finally Chapter 4 presents the results obtained regarding novel, bulk Pt-Si alloy catalysts used in methanol and carbon monoxide electro-oxidation. The work described was conducted in collaboration with The Electrochemical Energy Lab (EEL), Massachusetts In-

stitute of Technology (MIT), U. S. Preparation and structural characterisation methods used for bulk and surface compositions of Pt-Si alloys is also presented. Electrochemical characterisation showed a gradual improvement of activity for carbon monoxide and methanol electro-oxidation when higher Si contents were employed in the Pt-Si alloy.

Chapter 5 describes the preparation, material characterisation and initial electrochemical measurements of methanol electro-oxidation for ALD deposited Pt films on Si(100) and Pt-Si alloys on Si(100). ALD deposited Pt films on Si(100) were subsequently annealed at various temperatures to obtain Pt-Si alloy film on Si(100). Obtained alloys were subsequently characterised as potentially highly active methanol electro-oxidation catalysts, based on conclusions from Chapter 4.

Chapter 6 consists of concluding remarks and describes prospective future research.

Chapter 7 contains Appendixes.

Synopsis

Denne afhandling beskriver gennemførte undersøgelser, som omhandlende aktiviteten, stabiliteten og holdbarheden af ”supported” nano-partikler, ”bulk”- og tyndfilms - elektrokatalysatorer brugt i proton exchange membran brændselsceller (PEMFCs). Virkningen af forskellige faktorer og betingelser i reaktionerne, der involverede oxygen reduktion, carbonmonoxid og metanol elektro-oxidationsreaktioner er blevet undersøgt. De anvendte katalysatorer blev karakteriseret elektrokemisk og fysisk-kemisk ved brug af teknikker såsom: cyklisk voltammetri, roterende ”disk” elektrode teknik, SEM, TEM, EDS, XPS, TGA/DTA, Raman, XRD, FTIR-IR samt andre metoder.

Afhandlingen begynder med en introduktion i kapitel 1, der giver et overblik over brændselsceller, deres tilhørende reaktionsmekanismer, katalysatorer og katalysator-bærere.

Kapitel 2 præsenterer den teoretiske baggrund for projektet samt udstyr og teknikker brugt til at analysere katalysatorerne. Efterfølgende er der givet eksempler på elektrokemisk karakterisering af elektrokemiske overfladeområder fulgt af en beskrivelse af roterende ”disk” elektrode (RDE) principper og opsætning. Dernæst er bestemmelse af oxygen reduktion aktivitet og carbonmonoxid elektro-oxidations voltammetri beskrevet i forbindelse med levetids procedurer.

En væsentlig del af phd-projektet indebar udvikling af elektrokemisk instrumentering og teknikker såsom: RDE og opsætning, oxygen reduktion, methanol og CO elektro-oxidation, levetids procedurer, osv. Teknikkerne der anvendtes af forfatteren var selvlærte eller indlærte ved samarbejde med erfarne medarbejdere gennem de første år af phd-projektet. I de fremskredne stadier af projektet blev disse teknikker anvendt dagligt af DTU Proton Conductors gruppen.

Derudover opnåede forfatteren et højt færdighedsniveau i at betjene følgende instrumenter: TEM (FEI Tecnai T20 G2), EDS, AFM, XRD (PANalytical Multipurpose Diffractometer) og FTIR-IR.

Kapitel 3 beskriver resultaterne af syntese og afprøvning af Pt nano-partikel katalysatoren som er understøttet af PBI dækket grafen til oxygen reduktion reaktioner i PEMFCs. Fysisk-kemisk materiale karakterisation, fremstillingsprocedurer for tyndfilm RDE elektroder, katalysator ”ink” sammensætning, oxygen reduktions reaktionsaktivitet, elektrokemisk overflade – og levetidsstudier er også beskrevet i detalje.

Endelig præsenteres i kapitel 4 de opnåede resultater angående de nye ”bulk” Pt-Si legeringskatalysatorer brugt i methanol og carbonmonoxid elektro-oxidation. Det omtalte arbe-

jde er udført i samarbejde med The Electrochemical Energy Lab (EEL), Massachusetts Institute of Technology (MIT), U. S. Fremstilling og strukturelle karakterisation metoder brugt til ”bulk” og overflade sammensætning af Pt-Si legeringer er også repræsenteret. Elektrokemisk karakterisation viste en gradvis forbedring af carbonmonoxid og methanol elektro-oxidation når et højere Si indhold blev anvendt i Pt-Si legeringen.

Kapitel 5 beskriver fremstillingen, materiale karakteris og indledende elektrokemiske målinger af methanol elektro-oxidation for ALD Pt- film på Si(100) og Pt-Si legeringer på Si(100). ALD Pt- filmene på Si(100) blev efterfølgende opvarmet ved forskellige temperaturer for at opnå Pt-Si legerings-film på Si(100). De fremstillede legeringer blev efterfølgende karakteriseret som potentielt højaktive methanol oxidation katalysatorer baseret på konklusioner fra kapitel 4.

Kapitel 6 består af afsluttende bemærkninger og beskriver mulige fremtidige forskningsemner.

Kapitel 7 indeholder Appendikser.

Contents

List of Figures

List of Tables

Chapter 1

Introduction

1.1 A way to a sustainable future

Today our planet faces significant environmental and sustainability issues caused by the continuous growth of global society's present and future energy needs. Already enormous, these needs causing significant shifts in the composition of the world's energy demands in fuel. Rising energy needs mirrors an increasing global population, which currently comprises 7 billion and is expected to reach 8 billion by 2030 according to forecasts [10].

An increasing population has higher energy demands and predictions suggest an increase of about 30 percent from 2005 to 2030, Figure 1.1. Higher demands will eventually lead to total depletion of natural resources and eco-system degradation. Vehicles, industry and power plants emit harmful exhaust substances such as carbon dioxide (CO_2), sulfur dioxide (SO_2), nitrogen oxides (NO_x), etc. and at present the energy sector already produces more than 60 percent of total global CO_2 emissions [11].

It is clear that reduction of exhaust emissions and development of reliable, affordable energy sources through better efficiency, new technologies and a shift to cleaner fuels must be expanded in order to provide the energy needed for economic growth and societal development.

Is there a way to a sustainable future?

During the last few decades fuel cells have been identified as a potential key energy solution and alternative to standard sources of energy [2, 7, 12, 13]. Fuels cells operate with little to no carbon or other hazardous gas emissions and are therefore highly desirable as an energy source. In addition they are amongst the most efficient conversion devices currently available for converting hydrogen and other fuels into electricity. With their convenient size, low operational noise levels and efficiency fuel cells are ideal energy sources for a broad range

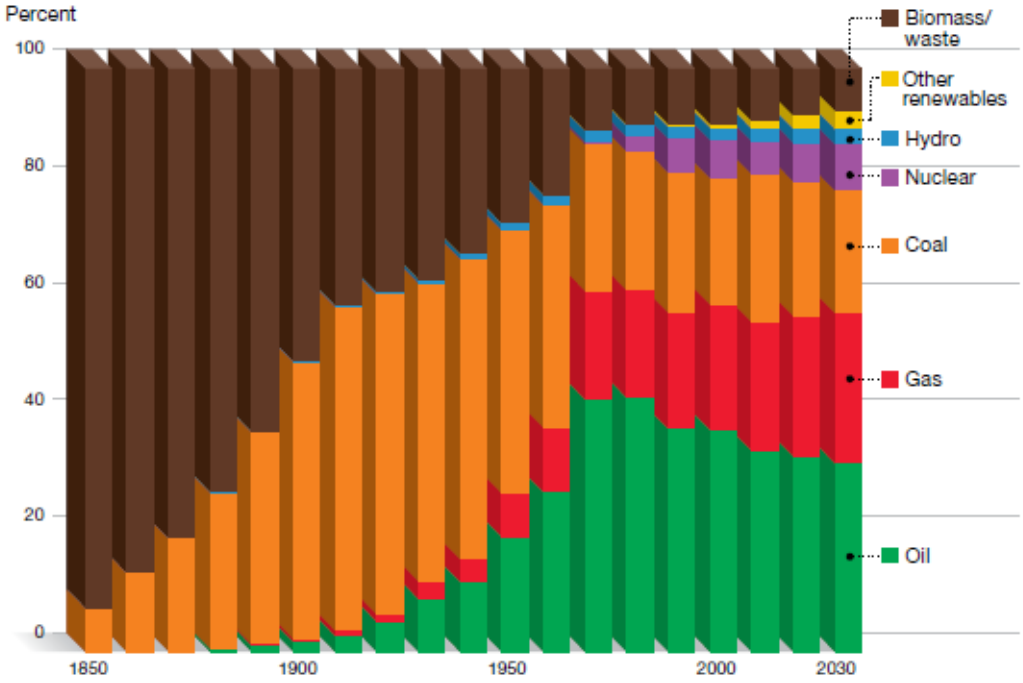

Figure 1.1: Global energy demand by fuel type 1850 - 2030 [1]

applications such as: transportation, heat and power production and distribution and energy storage systems. Finally, efficiency of fuel cells is independent of size and maintenance costs are low [2, 14–16] making them even more desirable as an energy source.

1.2 History of fuel cells

Over the last few years significant attempts have been made to develop fuel cell systems as a viable power source. The first report of electricity generation from the reaction of oxygen and hydrogen connected by electrodes was published in January 1839 by Swiss chemist Christian Friedrich Schönbein in Philosophical Magazine. One month later (in February 1839) Welsh judge and physical scientist Sir William R. Grove constructed the first prototype of a fuel cell describing his invention as a ”gas voltaic battery” [17]. Grove made his fuel cell by using platinum strip electrodes surrounded by tubes containing hydrogen and oxygen in a sulfuric acid solution. He established that an electric current running through water would split the individual molecules into hydrogen and oxygen and tried reversing the reaction - combining hydrogen and oxygen to produce electricity and water. The first fuel cell prototype utilizing porous electrodes was introduced by British scientists Ludwig Mond and his assistant Charles Langer in June 1889 [18]. Mond and Langer obtained a current of 2.8-3.5 $mAcm^{-2}$ at 0.73 V with cells of 700 cm^2 however observed a significant performance loss at the oxy-

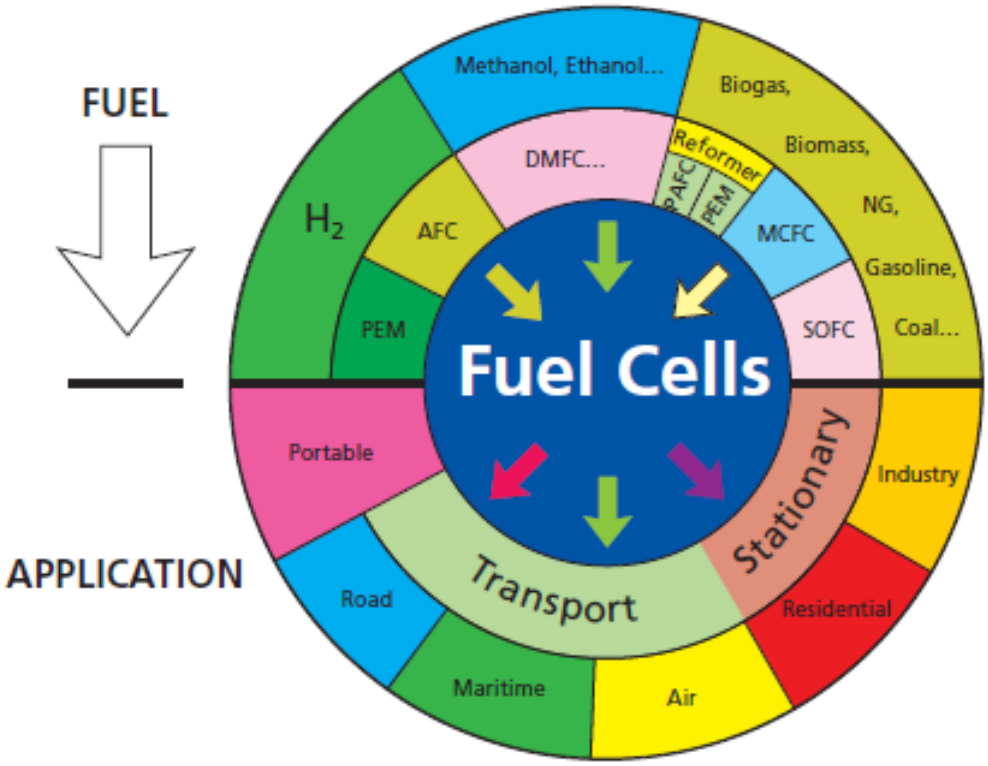

Figure 1.2: Fuel cell technologies, possible fuels and applications. Size of "sectors" has no connection with current or expected markets. [2]

gen electrode. Subsequently they employed Pt black as a catalyst and found that increasing Pt surface area leads to an increase of electrical current. In the years that followed these groundbreaking discoveries fuel cells have been modified with many different types of electrolytes and electrodes, such as the first use of phosphoric acid as an electrolyte by William White Jacques in 1890s. In 1932, whilst trying to find a more cost efficient electrode and less corrosive electrolyte Cambridge University Professor Francis T. Bacon modified Mond and Langer's fuel cell. The result was the "Bacon cell": the first alkaline electrolyte fuel cell utilizing pure hydrogen and oxygen able to operate at high pressure and temperature whilst allowing the use of inexpensive porous nickel electrodes.

It took 120 years from their inception before the potential application of fuel cells in defence and space exploration programs was identified. The first fuel cell used during a space mission was the polymer electrolyte membrane fuel cell (PEMFCs), developed by General Electric and used in Gemini V in 1965 [8]. The Gemini V PEMFC system was incredibly efficient, doubling performance of the battery systems used on previous missions.

Even so fuel cells from the 1960's and even today still tolerate technical barriers and high investment costs. Consequently a number of significant scientific and technical chal-

Table 1.1: Different fuel cell types and characteristics [7, 8].

Fuel cell type	Mobile ion	Operating temperature (°C)	Catalyst
Proton exchange membrane **(PEMFC)**	H^+	30-100	Pt
Direct methanol **(DMFC)**	H^+	20-90	Pt, Pt/Ru
Phosphoric acid **(PAFC)**	H^+	175-210	Pt
Alcaline **(AFC)**	OH^-	70-130	Ni, Ag, Pt
Molten carbonate **(MCFC)**	$CO_3{}^{2-}$	550-650	Ni
Solid oxide **(SOFC)**	O^{2-}	500-1000	Perovskites, Ni

lenges must be resolved in order to implement fuel cells as a key viable and clean energy technology for the future [7, 12]. One of the most significant challenges preventing fuel cell commercialization was overcome in the late 1980s and early 1990s, when platinum loading on the electrodes was reduced by factor of > 100 [8]. In spite of this advancement two major challenges still remain to be overcome; a slow reaction rate and the lack of hydrogen as a readily accessible fuel.

For these reasons many different fuels have been investigated resulting in new types of of fuel cells being developed with a range of applications. Six fuel cell types currently exist which can be divided into high and low temperature. The range of fuel cell technologies, possible fuels and applications currently available is shown in Figure 1.2. High temperature fuel cells, i.e. molten carbonate (MCFCs) and solid oxide (SOFCs) fuel cells, operate at temperatures between 500 - 1000°C. These cells do not require noble metal catalysts, however require long start-up times and large occupation volumes hence are usually only utilized for stationary applications such as power plants [19]. Low temperature fuel cells, i.e. alkaline (AFCs), phosphoric acid (PAFCs) and polymer electrolyte membrane (PEMFCs) fuel cells are usually small and light weight and therefore are more suitable for transport and portable applications. PEMFCs fuel cells are further divided to: direct methanol (DMFC), ethanol (EFC) and formic acid (FAFC) fuel cells, etc. The benefit of such fuel cells is easy handling and high energy density due to liquid fuel use (as opposed to hydrogen gas). However the downside is that low temperatures require noble metal catalysts such as platinum to generate a sufficient reaction rate, especially on the cathode side (i.e. for the oxygen reduction reaction or ORR). In addition improvement of the anode side of the fuel cell is necessary due to carbon monoxide produced as a by-product of the fuel oxidation. Carbon monoxide is a poison to platinum catalyst and effectively lowering the performance of the PEMFCs.

Normal operating temperatures of fuel cells defined by the nature of electrolyte are provided in Table 1.1.

1.3 General thermodynamics and kinetics of fuel cells

One of the main advantages of fuel cells is efficiency, which is much higher than any internal combustion engine. Unlike combustion systems, fuel cells produce electric energy directly from the chemical energy of fuel through an electro-chemical reaction thus are not limited by the Carnot cycle. The Carnot factor or oriental efficiency of the heat engine is expressed as:

$$\xi_{HE} = \frac{(T_h - T_c)}{T_c} \tag{1.1}$$

where T_h is the absolute temperature (K) of the hot inlet gas and T_c the temperature of the cold outlet gas and ξ_{HE} is the efficiency of the Carnot cycle [19].

1.3.1 Thermodynamics

A fuel cells maximum electrical efficiency can be expressed as the change in the Gibbs free energy:

$$\Delta G = -nFE^0 \tag{1.2}$$

nF in this case is the charge, where n is the number of electrons participating, F is the Faraday's constant and E^0 is the reversible cell potential [19].

If the overall reaction is at standard state, i.e. gases are at 1 bar pressure and temperature at 25°C equation 1.2 can be modified to:

$$\Delta G^0 = -nFE^{00} \tag{1.3}$$

with E^{00} as a cell voltage at standard conditions.

The thermodynamic efficiencies of a fuel cell can be described by the Gibbs-Helmholtz relation [19], where ΔH_r represent the heat delivered by chemical reaction or heat (enthalpy) released and ΔS_r is the reaction entropy:

$$\Delta G_r(P, T constant) = \Delta H_r - T\Delta S_r \tag{1.4}$$

Fuel cell efficiency is effected not only by changes in temperature but by fuel pressure and gas concentration.

For H_2/O_2 based fuel cell with the overall reaction is:

$$\text{“}2 + \frac{1}{2}O_2 \rightarrow H_2O (1.5)$$

Each of the reactant and product has an associated activity, a. By assuming activity is proportional to partial pressure at standard conditions, i.e., 25^{o}C, $p_{H_2} = p_{O_2} = 1$ bar, ideal gas behaviour applies and produced H_2O is in liquid form it can be assumed that $a_{H_2O} = 1$.

Consequently Gibbs free energy can be expressed as:

$$\Delta G_r = \Delta G_r^0 + RT ln \frac{a_{H_2} a_{O_2}^{1/2}}{a_{H_2O}} \tag{1.6}$$

The thermodynamic fuel cell efficiency is usually based on the higher heating value with the standard reaction enthalpy of liquid water formation. Therefore ΔH_r for equation 1.5 is -286 kJ/mol and ΔG_r is -237.1 kJ/mol at standard conditions (i.e., 25^{o}C, $p_{H_2} = p_{O_2} = 1$ bar producing H_2O_{liquid}). At these conditions, the theoretical efficiency of fuel cell is about 83%, which is significantly higher than the most of other energy conversion systems.

By substituting equations 1.2 and 1.3 into equation 1.6, the central equation describing the thermodynamics of fuel cells can be obtained. The Nernst equation describes the dependence of reversible cell voltage E in terms of reactant/product activities:

$$E = E^0 + \frac{RT}{nF} ln \frac{a_{H_2} a_{O_2}^{1/2}}{a_{H_2O}} \tag{1.7}$$

with R as the molar gas constant and T as the absolute temperature [8].

1.3.2 Kinetics

Although a comprehensive understanding of fuel cell thermodynamics is essential to screen responses to different environmental conditions, it is perhaps more important to understand fuel cell behaviour in practical applications, i.e. when undertaking electrical work. For example, how do reaction kinetics lead to fuel cell performance losses (i.e. voltage loss or activation loss)?

The Butler-Volmer equation describes kinetics of an electrochemical reaction in relation to the current density exponential increase with activation overpotential [14, 20]:

$$j = j_0 (e^{\alpha n F \eta_{act}/(RT)} - e^{-\beta n F \eta_{act}/(RT)}) \tag{1.8}$$

where j_0 is the exchange current density of an electrochemical reaction, α and β are the transfer coefficients, which expresses the symmetry dependence of the activation barrier,

η_{act} is the overpotential and n is the number of electrons transferred in the electrochemical reaction. Usually fuel cells operate at relatively high current densities which leads to a *totally irreversible* reaction process, thus the Butler-Volmer equation can be simplified to:

$$j = j_0 e^{\alpha n F \eta_{act}/(RT)} \tag{1.9}$$

In logarithmic form this equation is known as the *Tafel equation*:

$$\eta_{act} = a + b \log j \tag{1.10}$$

intercept a equal to $\frac{2.303RT}{\alpha nF} log\, i_0$ represents the kinetics of forward reaction (oxidation reaction). The so called *Tafel slope*, b, is equal to $\frac{2.303RT}{-\beta nF}$ and represents the backward reaction kinetics (reduction reaction) [21]. In H_2/O_2 fuel cells the most significant activation loses originate from the oxygen (cathode) kinetics, therefore there is a strong need to develop an electrocatalyst with a Tafel slope as small as possible.

1.4 The proton exchange membrane fuel cells

The main operating principle of fuels cells is conversion of chemical energy (of a fuel) into electrical energy. The electrochemically oxidized fuel subsequently generates water, heat and electricity. The overall redox reaction combines two half-cell reactions taking place at the anode and cathode electrodes, separated by an ion-conducting electrolyte (membrane). Direct voltage is delivered with electron transfers via the external circuit. The combination of anode and cathode with a memebrane in between produces a single membrane electrode assembly (MEA). The total voltage output of a single cell is constrained by the reversible potential of the two half-cell reactions. Therefore in order to achieve high operating voltages several electrically connected single cells usually form a fuel cell stack.

Proton exchange membrane fuel cells or polymer electrolyte fuel cells utilize solid polymer as electrolyte and are distinguished by fuel type used in the electrochemical reaction, e.g. hydrogen, hydrocarbons or methanol. The following section provides a short overview of the main characteristics associated with proton exchange membrane fuel cells operating on hydrogen fuel. It also describes the methanol fuel cell which has the same operating principle, but employs a methanol fuel.

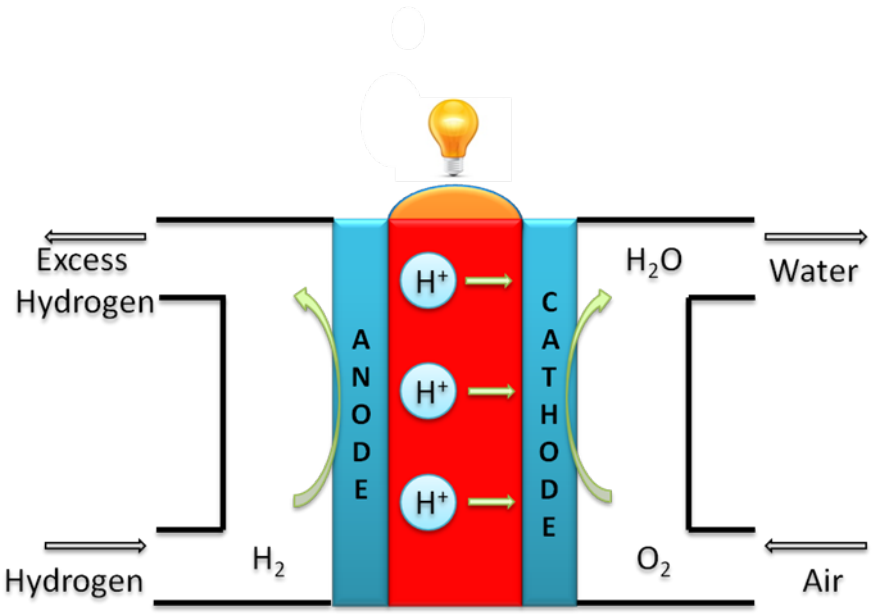

Figure 1.3: Operating principle of a proton exchange membrane fuel cell (PEMFC).

1.4.1 The proton exchange membrane fuel cells with H_2 as fuel

The PEMFC uses hydrogen as a fuel which is electrochemically oxidised at the anode side, whilst oxygen is reduced at the cathode side. A schematic illustration of the process is presented in Figure 1.3. H^+ ions (delivered from the anode through the membrane to the cathode side) recombine with oxide ions and electrons (delivered via the external electric circuit) producing water.

The overall reaction of the PEMFC is expressed in equation 1.11 to 1.13:

$$Anode : H_2 \longrightarrow 2H^+ + 2e^- \qquad E^0 = 0V vs.SHE \tag{1.11}$$

$$Cathode : \frac{1}{2}O_2 + 2H^+ + 2e^- \longrightarrow H_2O \qquad E^0 = 1.23V vs.SHE \tag{1.12}$$

$$Cell\ Reaction : H_2 + \frac{1}{2}O_2 \longrightarrow H_2O \qquad E^0 = 1.23V vs.SHE \tag{1.13}$$

The half-cell standard potential for the hydrogen oxidation reaction (HOR) at the anode side is defined as 0.0 V. The standard potential for the oxygen reduction reaction (ORR) at the cathode side is 1.23 V, resulting in a standard reversible cell potential of 1.23 V at 298 K, 1 bar and pH = 0.

To facilitate the electrochemical reaction at the interface between the electrolyte and the electrodes (both cathode and anode), a catalyst layer is used. The state-of-the-art catalyst for both HOR and ORR reactions is platinum based. Electrochemical reactions and therefore the produced current are proportional to the surface area of the catalyst. Therefore, it is highly desirable to maximize catalyst surface area whilst minimizing the cost by substitution of pure platinum or by reducing the catalyst's loading. Thus, the use of platinum nanoparticles with high surface and volume ratio, fixed on a supporting material as supported catalysts is a powerful method. The material support commonly used is a high-surface-area carbon, which allows distribution and stabilization of platinum nanoparticles on the surface. This method gives rise to a very high surface area and prevents segregation of platinum nanoparticles. In addition a high electron conductivity pathway between the catalyst and the current collector is also provided.

In this set up the membrane serves as a gas separator, electron insulator and proton conductor. The first proton exchange membranes used in PEM fuel cell applications were sulfonated polymers, such as the perfluorinated sulfonic acid membrane (PFSA). Subsequently these membranes have emerged as the most effective membrane materials for use at temperatures below the boiling point of water due to chemical stability and hydrous proton conductivity [22]. Nafion, discovered in the late 1960s by Walther Grot of DuPont [8], is the most well know membrane material in PFSA family of materials. It consists of a tetrafluoroethylene backbone with perfluorovinyl ether side groups terminated by sulfonate moieties (Figure 1.4). The tetrafluoroethylene backbone is highly hydrophobic whereas the sulfonic acid groups are highly hydrophilic and dissociate into mobile hydrated H^+ ions and immobile ${SO_3}^{2-}$ ions. Therefore mobility of H^+ ions and thus the membrane conductivity strongly depends on the water content. Dehydration causes dramatic proton conductivity decay of up to several orders of magnitude, hence finding an optimal humidification level of the PFSA membrane is critical during fuel cell operation. Consequently operational temperatures are restricted to a maximum of 100°C at ambient pressure for this type of fuel cells.

1.4.2 The direct methanol fuel cell

Whereas oxygen for the cathodic reaction can be taken from the surrounding air, availability of hydrogen coupled to difficulties of storage (i.e. requires large volumes), production, distribution and the requirement for significant safety precautions (i.e. due to its highly explosive nature) presents a considerable challenge for its use. The use of a liquid fuel directly at the anode side can however solve some of the issues regarding safety, storage and replenishing hydrogen by reforming. In general all organic molecules could be considered potential

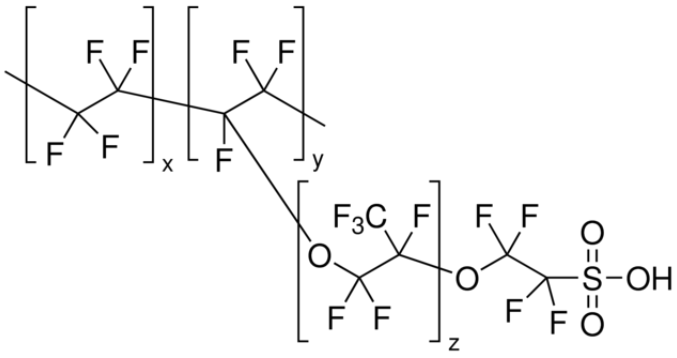

Figure 1.4: Chemical structure of Nafion.

candidates for a fuel source. Unfortunately however most compounds involve unwanted side reactions and high activation overpotentials giving rise to low rates of electrochemical reaction. The oxidation of methanol in contrast possesses a reasonable conversion rate. Consequently methanol is considered one of the most promising liquid fuels currently available as it is catalytically oxidized on a platinum surface, yielding CO_2 and six electrons per molecule.

The operation principle of a DMFC is similar to that of a regular H_2 fuelled PEMFC. The main difference is that a liquid mixture of water and methanol is utilized at the anode side. The electro-oxidation of methanol at the anode results in production of CO_2 and $6H^+$ ions. The standard potential of this reaction is 0.046 V. The oxygen reduction and water production proceed at the cathode side producing a standard reversible potential equal to 1.18 V, which is slightly lower than the one of a PEMFC (equation 1.14 to 1.16).

$$Anode : CH_3OH + H_2O \longrightarrow CO_2 + 6H^+ + 6e^- \qquad E^0 = 0.046V vs.SHE \tag{1.14}$$

$$Cathode : \frac{1}{2}O_2 + 2H^+ + 2e^- \longrightarrow H_2O \qquad E^0 = 1.23V vs.SHE \tag{1.15}$$

$$Cell\ Reaction : CH_3OH + \frac{1}{2}O_2 \longrightarrow CO_2 + H_2O \qquad E^0 = 1.18V vs.SHE \tag{1.16}$$

Despite the relative simplicity in utilizing methanol, it involves more complex oxidation reactions and proceeds much slower than oxidation of pure hydrogen. Therefore, it is clear that the slow rate of methanol oxidation is the most critical problem associated with the DMFC and requires immediate development of a suitable catalyst to increase the rate.

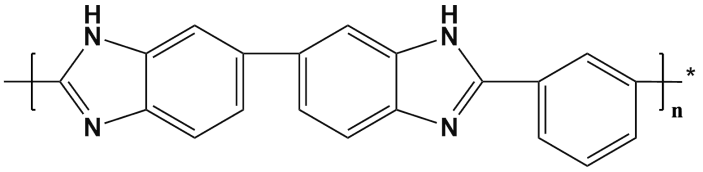

Figure 1.5: Chemical structure of PBI.

Platinum, the most efficient and widely used catalyst for hydrogen oxidation in PEM fuel cells, unfortunately suffers from rapid deactivation when used in conjunction with methanol, due to poisoning by intermediate reaction species. Bi-metal catalysts in contrast are known to give better performances under these conditions. An alloy of platinum and ruthenium in equal molar proportions for example is considered a very effective and powerful catalyst for electro-oxidation of methanol [23]. Pt-Ru crystals are usually dispersed on a high-surface-area carbon material, similar to catalysts used in normal PEMFC's.

Apart from the slow reaction rate of methanol electro-oxidation, DMFC faces an additional problem of fuel crossover when using the PFSA membranes, due to high methanol permeability. The methanol crossing over to the cathode side side causes a decrease in the cathode potential due to simultaneous oxygen reduction and methanol oxidation creating high efficiency losses. Moreover, PFSA membranes are expensive and have a strong dependence on hydration (as described previously). An alternative phosphoric acid doped poly[2,2;(m-phenylene)-5,5; bibenzimidazole] (PBI, Figure 1.5) membrane was first suggested as a potential electrolyte material for PEM fuel cells in the 1990s [24]. The proton conduction mechanism of phosphoric acid doped PBI membranes does not depend on the presence of water molecules within the membrane matrix. Hence, it has emerged as one of the most promising PEMFC and DMFC membrane materials for operation in the 100-200°C temperature range [25,26]. Operating at temperatures above 100°C gives a number of advantages including; simplified water management and cooling systems and facilitation of heat recovery [27]. Moreover, at greater than 100 degrees the tolerance of the electrocatalyst to impurities is improved [28]. The effects of impurities such as trace amounts of CO originating from impure hydrogen or reformatted fuel [29] or as a by-product from electro-oxidation of methanol in DMFCs is reduced.

1.5 Catalyst's reaction mechanisms for PEMFCs and DMFCs

This chapter gives an overview of the electrochemical reactions occurring at the anode (hydrogen and methanol electo-oxidation) and the cathode (oxygen reduction) compartments of a polymer electrolyte fuel cell. A brief description of the hydrogen electro-oxidation reaction is given before a more detailed discussion regarding methanol electro-oxidation and oxygen reduction reactions is provided as the main focus of the thesis.

1.5.1 The hydrogen oxidation reaction

The hydrogen oxidation reaction (HOR) in acid electrolyte is an uncomplicated, heterogeneous reaction requiring only minor catalyst loadings in order to proceed very fast, with very low activation losses when using platinum catalyst for the anode side of PEM fuel cell.

In an aqueous acid, the net hydrogen oxidation reaction is:

$$H_2 + 2H_2O \leftrightharpoons 2H_3O^+ + 2e^- \tag{1.17}$$

The reaction can proceed through a number of sequential and simultaneous steps (elementary reactions) involving many intermediate species [30–32]. General steps of the reaction are usually described by following equations 1.18 to 1.21:

$$H_2 \leftrightharpoons 2H_{ads} \qquad Tafel\ Reaction \tag{1.18}$$

Equation 1.19 describes the dissociative adsorption of H_2 without electron transfer (Tafel reaction) followed by the discharge of adsorbed hydrogen. This can occur via simultaneous electron transfer, depending on whether oxidation of H_{ads} or $H_{2,ads}$ takes place, respectively. Oxidation of H_{ads} proceeds via the Volmer reaction (equation 1.19) and oxidation of $H_{2,ads}$ via the Heyrovsky reaction (equation 1.20) mechanism.

$$H_{ads} + H_2O \leftrightharpoons H_3O^+ + e^- \qquad Volmer\ Reaction \tag{1.19}$$

$$H_{2,ads} + H_2O \leftrightharpoons [H_{ads} \cdot H_3O]^+ + e^- \leftrightharpoons H_{ads} + H_3O^+ + e^- \qquad Heyrovsky\ Reaction \tag{1.20}$$

equation 1.20 then can follow by reaction 1.21

$$H_{ads} + H_2O \leftrightharpoons H_3O^+ + e^- \qquad Volmer\ Reaction \tag{1.21}$$

The preferential pathway for the HOR mechanism on the hydrogen electrode depends on experimental conditions, e.g. the electrolyte medium, the current density and the catalyst surface (i.e. crystal orientation). Despite these factors cell voltage losses at the anode are negligible, even for very low platinum loadings. For example, at loadings of 0.05 mgPt/cm$_{electrode}{}^2$ losses have been reported at 5 mV [33]. Furthermore, some studies have shown that performance of the platinum anode in H_2/air PEM fuel cell is independent on platinum loadings varied between 0.4 and 0.05 mgPt/cm$^2{}_{electrode}$ [34].

And, some studies show that H_2/air PEM fuel cell performance of the Pt anode is independent on Pt loadings varied between 0.4 and 0.05 mgPt/cm$^2{}_{electrode}$ [34]. These observations could be a manifestation of very high HOR exchange current densities when using pure hydrogen and platinum as a catalyst.

1.5.2 The methanol oxidation reaction and CO poisoning

Methanol electro-oxidation reaction (MOR) has been the subject of a number of studies over the past 20 years suggesting a complex reaction mechanism [35–40].

The net methanol electro-oxidation reaction in acid solution is described in equation 1.22:

$$CH_3OH + H_2O \leftrightharpoons CO_2 + 6H^+ + 6e^- \tag{1.22}$$

, where water is consumed during formation of CO_2 - final product of complete electro-oxidation. The thermodynamic potential of this reaction is very close to the equilibrium potential of hydrogen. The methanol electro-oxidation reaction involves six electrons instead of two as for hydrogen electro-oxidation. However, compared with hydrogen electro-oxidation, methanol electro-oxidation is slower by several orders of magnitude.

The total electro-oxidation of methanol to CO_2 is generally accepted to occur through a dual pathway as shown in Figure1.6 [41].

The *indirect* or poisoning intermediate pathway involves the oxidation of methanol and formation of poisoning species, such as CO_{ad} (Figure 1.6 (1)-(2)).

In the *direct* or active intermediate pathway methanol is oxidized directly to form CO_2 without passing through a poisoning intermediate such as carbon monoxide (Figure 1.6 (3)-(5)). However, this mechanism does involve formation of intermediate species such as formic acid and formaldehyde. Consideration of the formation of these intermediate species is still

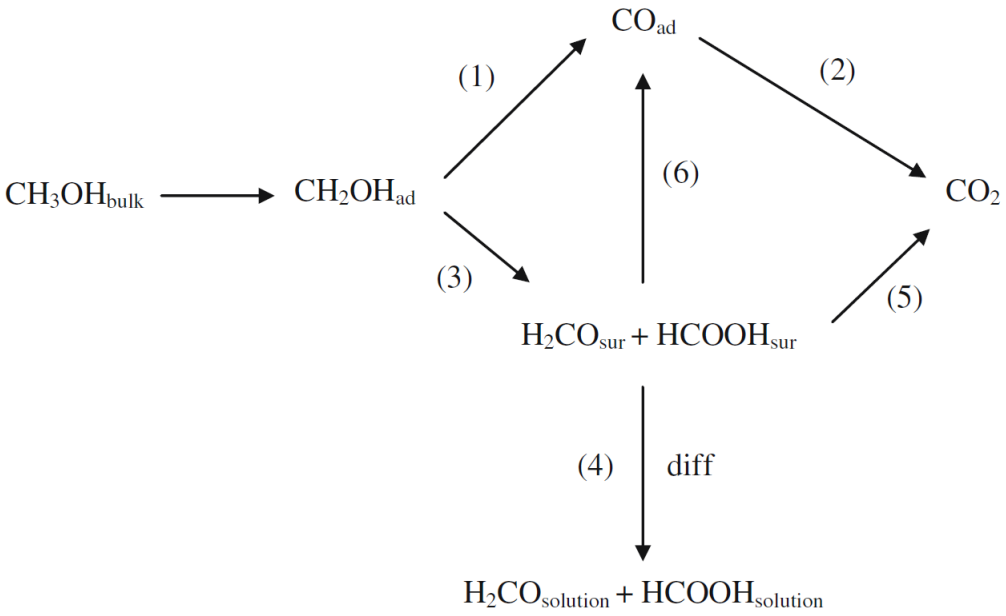

Figure 1.6: Schematic representation of the parallel pathway mechanism for methanol oxidation on platinum electrodes as proposed by Baltruschat et al. [3]

critical as it is well known that both substances can also form CO_{ad} (Figure 1.6 (6)) [39,42]. In particular formic acid is known to have a dual pathway of oxidation to CO_2 [43,44].

CO groups can be adsorbed in different ways on the catalyst surface simultaneously. The CO groups require two or one electrons per site to form CO_2 and follow *bonded* and *bridge-bonded* models, respectively [45].

The mechanism of the CO_{ad} electro-oxidation in acidic solutions, originally proposed by Gilman [46], assumes a *Langmuir-Hinshelwood* reaction type [40,47] 1.23 to 1.25. According to the *Langmuir-Hinshelwood* mechanism, CO_{ad} and a surface oxygen-containing species located on adjacent sites form CO_2. The oxygen-containing species is a result of water oxidation at the electrode surface and is usually a OH_{ad}:

$$H_2O + {}^* \rightleftharpoons OH_{ad} + H^+ + e^- \tag{1.23}$$

$$CO_{ad} + OH_{ad} \longrightarrow COOH_{ad} \tag{1.24}$$

$$COOH_{ads} \longrightarrow CO_2 + H^+ + e^- + 2^* \tag{1.25}$$

where * is a free site on the surface [30]. Reaction 1.23 and 1.25 are fast and reaction1.24 the rate-determining step which depends on surface diffusion rates of reactants according to a number of publications [48, 49].

A key determinant of the rate is the distribution and mobility of reactants on the catalyst surface. Two limiting cases are known for the overall reaction rate [47]. Firstly the *"mean-field approximation"*, whereby reactants are perfectly mixed on the surface and the reaction rate is proportional to the average coverage of the reaction species. This is reasonable if the surface diffusion is much faster than the reaction itself. Secondly the *"nucleation and growth model"*, where reaction species are assumed to be immobile. The reaction takes places mainly at interface between the two reacting phases, causing formation of CO islands which in turn ensures less free sites for the OH_{ad}. Formation of OH_{ad} is restricted to relatively few sites at lower potentials, therefore the actual rate of the CO_{ad} + OH_{ad} strongly depends on OH_{ad} coverage.

1.5.3 The oxygen reduction reaction

The oxygen reduction reaction (ORR) occurring at the cathode electrode is significantly more demanding and complex than the hydrogen oxidation process. It has much larger overpotentials and a number of consecutive and parallel reaction mechanisms and elementary steps occurring simultaneously. In the acidic electrochemical environment two reaction pathways are usually assumed, as described by equations 1.26 to 1.29 [30, 31].

I. Direct 4-electron pathway:

$$O_2 + 4H^+ + 4e^- \leftrightharpoons 2H_2O \qquad E^0 = 1.229V \tag{1.26}$$

II. Indirect (peroxide) pathway:

$$O_2 + 2H^+ + 2e^- \leftrightharpoons H_2O_2 \qquad E^0 = 0.67V \tag{1.27}$$

followed by either 2-electron reduction:

$$H_2O_2 + 2H^+ + 2e^- \leftrightharpoons 2H_2O \qquad E^0 = 1.77V \tag{1.28}$$

or a decomposition reaction:

$$2H_2O_2 \leftrightharpoons 2H_2O + O_2 \tag{1.29}$$

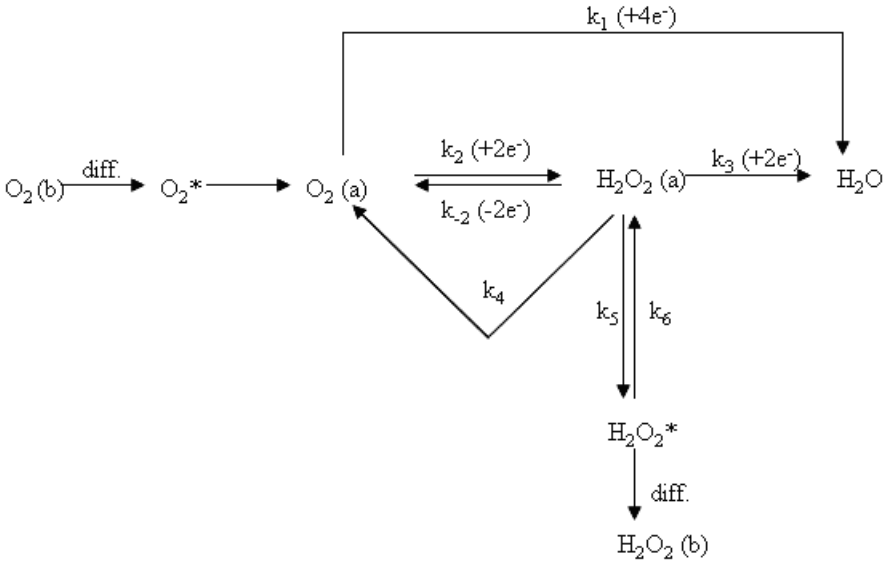

Figure 1.7: A reaction scheme for cathodic O_2 reduction proposed by Wroblowa et al [4].

The ORR can proceed via a direct pathway (I) to water or via a indirect pathway (II) involving formation of intermediate H_2O_2. A more complete analysis of the parallel processes can be carried out according to the general scheme of the ORR mechanism proposed by Wroblowa et al. [4], (Figure 1.7). The diffusion of O_2 from the bulk phase to the electrode surface region occurs first. The pre-adsorbed oxygen then follows the direct four-electron reduction pathway to water (k_1), or through a reverse two-electron reduction to intermediate H_2O_2 (k_2, k_{-2}) with subsequent reduction of adsorbed H_2O_2 to water (k_3). In addition, adsorbed hydrogen peroxide can be catalytically decomposed to reducible O_2 (k_4) and water, or be desorbed (k_5) into solution and subsequently adsorbed (k_6) back. Desorbed hydrogen peroxide can also diffuse from the surface region into the bulk.

Depending on the interaction of O_2 with the catalyst surface, oxygen reduction will either proceed via a two-site adsorption leading to direct four-electron reduction of oxygen to water, or end-on adsorption for the hydrogen peroxide route [5, 30]. In an acidic medium the first step is accepted to involve adsorption of O_2 on the surface, however the type of the site and configuration are uncertain. Possible oxygen adsorption states are schematically presented in Figure 1.8 with corresponding possible pathways for these three models shown in Figure 1.9.

The Griffiths model of Figure 1.8 (a) represents interaction of O_2 with two bonds on a single substrate atom and the Yeager (or Bridge) model (c) – a bridge-like adsorption of two bonds (with partially filled d orbitals) interacting with the π^* orbitals of O_2. Both

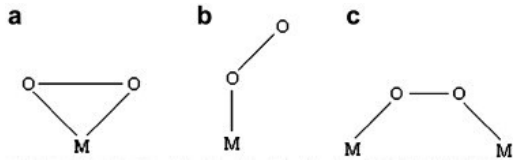

Figure 1.8: Models for the adsorption of oxygen on catalyst surfaces [5].

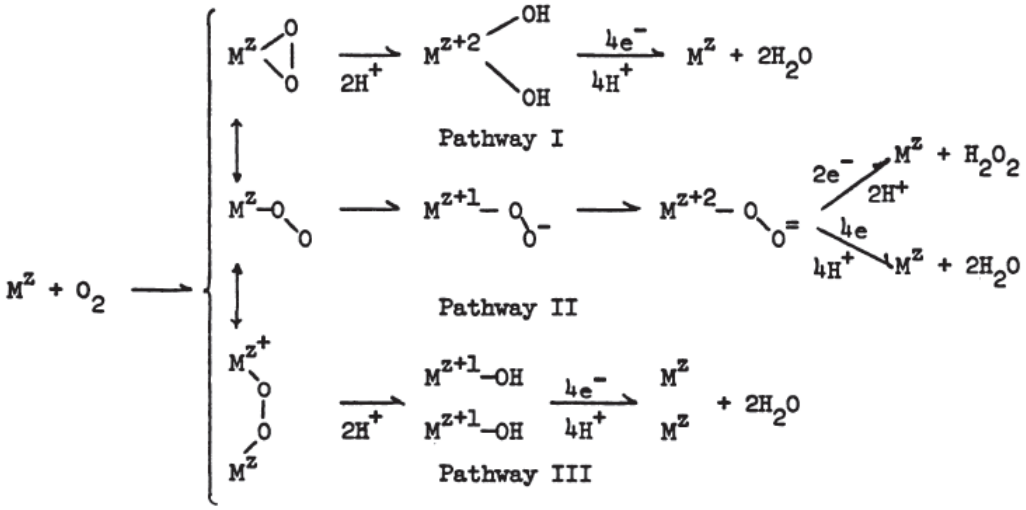

Figure 1.9: Models for the adsorption of oxygen on catalyst surfaces and corresponding ORR pathways [5].

(a) and (c) models include stretching of the O-O-binding due to adsorption on both sides allowing preferred decomposition of the O_2 molecule. For this reason a direct 4-electron pathway reduction to water is favourable for reaction pathways I or III (Figure 1.9). The Pauling model (b) has the end-on adsorption of the oxygen molecule through a single bond via its π orbital, leaving the O-O-binding almost unaffected. Therefore formation of H_2O_2 is favourable and reaction pathway II is preferred.

In addition to the described factors the ORR pathway strongly depends on pH, type of electrolyte and presence or absence of anions adsorbed to the catalysts surface.

1.6 Catalysts and catalyst's supports for PEMFCs

1.6.1 Catalysts for methanol and CO electro-oxidation

Strongly adsorbed intermediates prevent facile breaking of C-H and O-H bonds. Therefore an ideal catalyst for methanol oxidation should allow dissociation of the C-H bond as well as facilitate the reaction of the resulting residue with some form of O-containing species forming CO_2.

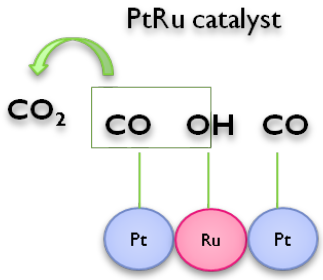

Figure 1.10: Schematic representation of the Pt-Ru electro-oxidation mechanism

At present no more effective catalysts are known for this purpose than Pt, in spite of its limitations arising from surface blockage by strongly adsorbed intermediates. Studies on well defined surfaces have helped identify the importance of electronic structure and surface atomic structure in governing activity in addition to increasing understanding of surface mechanisms [50, 51]. Increasing steps and kicks on the Pt single crystal surfaces has been shown to facilitate the activity of intermediate CO and methanol up to several orders of magnitude [40, 47]. For nanoscale catalysts with high-index surfaces it was also shown that surface steps play a significant role in enhancing intrinsic activity for CO and methanol electro-oxidation. For example, increasing steps on the (100) surfaces on Pt nanoparticles of $\backsim$2 nm has been previously shown to enhance intrinsic activity for CO and for methanol electro-oxidation up to $\backsim$200 % [40].

A more interesting alternative to pure Pt is the application of binary and ternary CO tolerant catalysts, usually based on the modification of Pt with another metal. A number of platinum alloys (Pt-M) have been suggested and subsequently found to show improved CO tolerance at relatively low potentials compared to pure Pt such as; Pt-Ru [38, 52–54] Pt-Sn [53, 55, 56], Pt-Rh [57, 58], Pt-Mo [59], Pt-Re [60], etc. The increased catalytic activity of these alloys towards methanol and CO electro-oxidation has been attributed to formation of hydrated oxides on the alloying transition metal. These hydrated oxides facilitate the oxidation of CO and provide free surface sites for oxidation of hydrogen.

At present an alloy of Pt-Ru with ratio 1:1 is recognised as the most promising catalyst for both methanol and CO electro-oxidation [30]. The enhanced effect of the Pt-Ru is primarily explained by a so-called bi-functional mechanism of reaction, which suggests joint activities of Ru and Pt. The Ru atoms nucleate oxygenated species through the activation of water whilst Pt adsorbs and dissociates methanol as schematically represented by Figure 1.10 following the *Langmuir-Hinshelwood* mechanism.

Despite these advantages, even well-alloyed Pt-M catalysts tend to suffer from the leaching of the base-metal under the acidic operating conditions of fuel cells which leads to inhi-

bition of methanol adsorption. Therefore, it is necessary to investigate alloying Pt with other non-metal elements such as Si, for instance. Si is relatively insoluble in most of acids and may provide new Pt-alloy catalysts for electro-oxidation of CO and small organic molecules such as methanol. The results of this work will be discussed in Chapter IV.

1.6.2 Catalysts for the oxygen reduction reaction

In order for the 4-electron oxygen reduction pathway to proceed with full conversion to water, without formation of H_2O_2 as an intermediate, two neighbouring adsorption sites for oxygen molecule are needed. Different materials induce the reaction to proceed via either 4-electron pathway or via a peroxide pathway, or in some cases a combination.

Pt is recognized as the most active material for catalysis of oxygen reduction in acidic electrolytes by promoting the 4-electron pathway. However, the preferred mechanism would be a series of 4-electron pathway combined with the peroxide intermediate mechanism [61]. The oxygen reduction activity in acid for polycrystalline Pt varies depending on crystal face orientation. In a sulphuric acid electrolyte the activity of oxygen reduction reaction is known to increase according to the following series; Pt(111) $<$ Pt(100) $<$ Pt(110) [61]. In contrast perchloric acid the activity proceeds according to; Pt(100) $<$ Pt(110) $<$ Pt(111) [62]. Variations in activity related to the crystal face in sulfuric acid arise from the specific adsorption of sulfate/bisulfate anions in the electrolyte, which induces a strong inhibitory effect on the Pt(111) surface making it 100 times more active than other crystal faces. Absence of sulfate/bisulfate anions in perchloric acid electrolyte results in much higher ORR activities for all three crystal faces [62].

Despite its stability and low overpotential in comparison to other metal catalysts, the ORR overpotential of state-of-the-art Pt catalyst is in general still very large. In addition, the desire for improvement of stability and durability for PEMFCs commercialization is high.

Lowering the cost and improving the ORR activity of Pt can be done by alloying it with other metals. Consequently 3d transition metals, i.e. Pt-M (M = Fe, Co, Ni, and Cu), together with partially de-alloyed core-shell catalysts, i.e. Pt-Cu nanoparticles, (which are found to be more active than pure Pt) have been studied intensively [63–72]. In these alloys, a Pt atomic overlayer is believed to form at the surface, laying above the transition metal core. The Pt overlayer is formed by either annealing in an inert or reducing atmosphere, or more typically, by leaching out the solute metal from the outer layer in the acidic electrolyte. This overlayer is typically several monolayers thick and stabilizes the catalyst for exposure to the severe electrochemical environment of a PEMFC. Recent studies of polycrystalline Pt alloys with early transition metals or rare earths, such as Pt_3Y [64], Pt_XLa [73, 74] and Pt_5Gd [67]

show an increase in ORR activity up to 5-fold in comparison to pure Pt at 0.9 V. These alloys were identified on the basis of density functional theory (DFT) calculations which showed a volcano-like relationship between the electrocatalystic activity and the d band energy of the metal [64] which was also confirmed experimentally. It is believed that the exceptionally negative heats of formation with which they are associated provide these alloys with high kinetic stability preventing de-alloying. Heat of formation determines the kinetic barrier for the solute metals diffusion through the alloy core and Pt overlayer. The ORR activity is explained by means of compressive strain effects that provide weakening of the OH binding energy, relative to P(111), of 0.3 eV. This is important as the OH^- species formed on the catalyst surface must not be bonded too strongly nor too weakly in order for H_2O desorption to be fast.

Pt ternary alloys also exhibit significant promise for increasing oxygen reduction activity. Pt-ternary alloys, i.e. Pt_3(MN) with M, N = Fe, Co, Ni, etc., demonstrate clearly the potential for ternary alloy catalysts to attain higher catalytic activities when compared to monometallic Pt or bimetallic Pt alloyst [75,76]. For example, $Pt_{85}Fe_{10}Co_5$ catalyst shows 3.5 times higher mass activity towards ORR than that of pure Pt [76]. However the most active Pt ternary system so far was investigated was found to be $Pt_3(CoNi)_1$, which exhibits an improvement factor of 4 compare to that of pure Pt. The ORR activity of these alloys can be explained by considering the *d* band center downshift of $\sim$0.1 eV compared to pure Pt [75]. Consequently there is a reduction of surface coverage caused by oxygenated species (e.g., OH^-) and thus an increase in the number of active sites accessible for molecular oxygen.

1.6.3 Catalyst's supports

As previously mentioned in Section 1.4, in order to reduce the amount of catalyst needed and obtain higher catalytic surface area (hence lower PEMFCs cost) an appropriate support is essential. This subsection will look into supports for ORR catalysts in relation to the experimental work described in Chapter 3.

Carbon support strongly effect fuels cell performance. The support influences not only catalyst utilization, but intrinsic catalyst activity. An ideal support for a catalytic material should posses; a high specific surface area, be corrosion resistant and stable, allow uniform dispersion and prevent sintering of the catalyst nanoparticles. Furthermore it should be able to; conduct electrons and heat, allow easy transport of reactants and products and be inexpensive [77]. The state-of-the-art Pt/C catalyst utilises a high surface area carbon black, e.g. microporous Vulcan^{TM} carbon XC-72R as a support. BET specific surface of XC is about 250 m^2/g) whilst average particle size is $\sim$30nm. The Pt particle size of Pt/C catalyst is usu-

ally about 3-5 nm. It is desirable that particle size should be as small as possible in order to obtain higher ORR activity however it should be not too small in order to avoid sintering of Pt nanoparticles. In some instances Pt nanoparticles supported on carbon black (Pt/C) have been found to decrease in particle size with increasing specific surface area, giving higher mass and specific ORR activity. However, this material suffers from fast durability degradation, making the implementation of new stable materials necessary in order to maintain longer term operation of fuel cells.

Numerous carbon materials were tested in order to substitute carbon black including; ordered mesoporous carbon [78], graphitized carbon [79], carbon nanofibers [80], carbon nonotubes [81–83], graphene [84–87], etc. For ordered mesoporous carbon (OMC) loaded with Pt, the ORR activity was found to decrease as carbon diameter decreased. This effect attributed to a higher electronic resistance [78], as well as higher surface area and more accessibility to carbon surface sites for Pt nucleation. The result was smaller and more uniformly distributed Pt nanoparticles [88]. However, mass transport limitations are evident for reactants (O_2, H^+) and products (H_2O) away from the Pt deposited deep within the pores [89]. In addition OMCs exhibited relatively low electronic conductivity [90]. This was however not the case for carbon nanotubes (CNTs) and nanofibers (CNFs). CNTs and CNFs were seen to posses high electrical conductivity and specific interaction between catalytic metals and CNT supports (the delocalized *p* electrons of CNTs and Pt *d*-electrons) resulting in higher catalytic activity. Specific surface area of CNTs and CNFs can be up to 900 m_2/g. Compared to carbon blacks, which contains a significant amount of organosulfur which can poison the catalyst, CNTs and CNFs have minor impurities. They are also free from deep cracks that exist in carbon black, where deposited Pt nanoparticles lose catalytic activity due to a lack of formation of an electrochemical triple phase boundary (TPB) [90]. The favourable structure and electrical properties of CNTs and CNFs bestow an increased level of mass transport of H_2O and O_2 in addition to a low electric resistance [91] further demonstrating their efficiency.

This is also true for graphene supports which are recently attracting more and more attention as one of the most effective carbon materials [92–94] the subject of which is fully discussed in Chapter 3.

1.7 List of publications

List of publications relevant to this thesis (See Appendix)

[95] A. A. Permyakova, B. Han, J. O. Jensen, N. J. Bjerrum, and Y. Shao-Horn. Pt-Si Alloys as Alternative Bifunctional Catalysts for CO and Methanol Electro-oxidation. *To be submitted to Journal of the American Chemical Society,* 2013.

[96] A. A. Permyakova, J. Suntivich, B. Han, J. O. Jensen, Q. F. Li, N. J. Bjerrum, and Y. Shao-Horn. Bifunctional Pt-Si Alloys for Small Organic Molecule Electro-oxidation. In *2012 MRS Fall Meeting & Exhibit conference, abstract, oral presentation,* Boston, MA, USA, November 2012.

[97] A. A. Permyakova, Q. F. Li, J. O. Jensen, and N. J. Bjerrum. Poly(benzimidazole)-functionalized Graphene Supported Pt Electrocatalyst and its Application in High Temperature PEM Fuel Cell. In *ECS 222nd Meeting (PRiME) conference, abstract, poster presentation,* Honolulu, Hawaii, USA, October 2012.

[98] A. A. Permyakova, J. O. Jensen, Q. F. Li, and N. J. Bjerrum. Poly(benzimidazole)-functionalized Graphene as a Stable and Durable Support for PEM Fuel Cell Electrocatalysts. In *3rd CARISMA International Conference, abstract, poster presentation,* Copenhagen, Denmark, September 2012.

[99] A. A. Permyakova. Interviewed by Charlotte Malasse. Smil! Du er på. In *DTU - Avisen, participation in interview for printed media,* January 2012.
http://emagstudio.win.dtu.dk/E-books/DTU-Avisen/DTUavis0112/

[100] D. Plackett, A. Siu, Q. F. Li, C. Pan, J. O. Jensen, S. F. Nielsen, A. A. Permyakova, and N. J. Bjerrum. High Temperature Proton Exchange Membranes Based on Polybenzimidazole and Clay Composites for Fuel Cells. *Journal of Membrane Science,* 383, 1-2: 78–87, 2011.

[101] A. A. Permyakova. Development of Improved Electrodes in High Temperature PEM Fuel Cells. *Participation in video presentation of the PhD project for the DTU Chemistry PhD School Symposium 2011,* Copenhagen, Denmark, October 2011.
http://www.youtube.com/watch?v=7Owp7MVKMOc

[102] A. A. Permyakova, Q. F. Li, J. O. Jensen, and N. J. Bjerrum. Development and Characterisation of Active and Durable Electrocatalysts for HT-PEM Fuel Cells 2. In *Advanced Studies of Polymer Electrolyte Fuel Cells, The book of 4th International Summer School: book article, poster presentation, pages 96–98, Eds: S. Mitsushima, T. Araki, K. Ota, V. Hacker, M. Siebenhofer, Yokohama, Japan. Publisher: Graz University of Technology*, September 2011. ISBN:978-3-85125-170-8.

[103] J. O. Jensen, Q. Li, Cleemann L. N. Vassiliev, C. Pan, A. A. Permyakova and N. J. Bjerrum. HT - PEMFCs in Denmark. In *PROCON Summer school, oral presen-*

tation, Changchun Institute of Applied Chemistry (CIAC) Chinese Academy of Sciences, Changchun, China, August 2011.

[104] A. A. Permyakova, Q. F. Li, J. O. Jensen, and N. J. Bjerrum. Development and Characterisation of Active and Durable Electrocatalysts for HT-PEM Fuel Cells. In *Hydrogen + Fuel Cells 2011 conference, abstract, poster presentation,* Vancouver, British Columbia, Canada, May 2011.

[105] A. A. Permyakova, Q. F. Li, J. O. Jensen, and N. J. Bjerrum. Half Cell Characteristics of High Temperature PEM Fuel Cell. In *DTU Chemistry PhD School Symposium 2010, abstract, poster presentation,* Gentofte, Denmark, November 2010.

1.8 Structure of the thesis

In the present thesis, tree main topics will be discussed;

In Chapter 3 will present the activity and durability studies conducted in relation to Pt nanoparticle PEM fuel cell electrocatalysts. The effects of the support material will be investigated and the principles for optimum design for improved catalysts determined. In particular a Graphene-PBI supported platinum nano-particulate catalyst for electrocatalystic reduction of oxygen will be described. Results will be compared by consideration of ORR activity along with cycling stability and electrochemical surface area (ECSA) of Pt/Graphene-PBI, Pt/Graphene and commercial 40% Pt/Vulcan XC 72R electrocatalysts. Next durability and activity results associated with the Pt/Graphene-PBI will be discussed in terms of particle size and distribution, ECSA and activity change.

In Chapter 4 the activity of the bulk Pt-Si catalysts towards carbon monoxide and methanol electro-oxidation for DMFC anodes will be investigated. Subsequently the performance attained from alloying Pt with other elements, such as non-metal silicon, will be discussed and the novel Pt-Si catalysts mechanism for carbon monoxide and methanol electro-oxidation reaction will be proposed.

In Chapter 5 Supported by the results of the Pt-Si alloy catalyst presented in Chapter 4, the potential properties of Pt-Si films deposited on the Si (100) substrate as anodes in miniature DMFCs will be investigated. For this purpose ways of preparing Pt-Si alloy thin films, their physical characterisation and attaining starting electrochemical measurements, i.e. methanol electro-oxidation reaction, are explored.

Chapter 2

Experimental methods and techniques

2.1 X-ray Diffraction

X-ray diffraction (XRD) is one of the most common techniques used for catalyst characterisation. Based on diffraction pattern, this technique allows identification of the periodic atomic structure, chemical composition, physical properties and determination of catalyst particle size of crystalline materials.

The dominant mechanism involves the exposure of the catalyst to monochromatic X-ray waves and measurement of the scatter produced by the atoms at an angle equal to θ. The scattered X-rays undergo constructive and destructive interference. Only when the constructive interference occurs – the so called *Bragg's law* is satisfied. The technique was developed by English physicists Sir W. H. Bragg and his son Sir W. L. Bragg in 1913 and is illustrated in figure 2.1. Using the following equation *Bragg's law* law can be described thus:

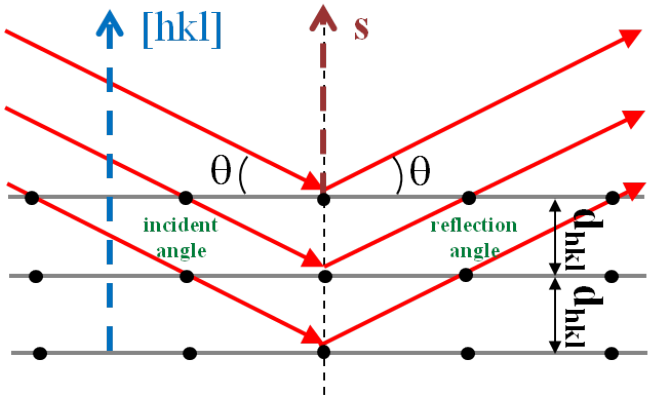

Figure 2.1: Schematic illustration of the Bragg's relation.

$$n\lambda = 2d_{hkl} \cdot sin\theta \tag{2.1}$$

where the variable d_{hkl} is the distance between atomic layers in a crystal, variable λ is the wavelength of the incoming X-ray beam and n is an integer. The space between diffracting planes of atoms determines peak positions. In addition, the direction perpendicular to a plane of atoms (the plane normal $[hkl]$) and the vector that bisects the angle between the incident and diffracted beam (diffraction vector S) must be parallel.

Depending on the size and shape of the studied material certain directions of possible diffraction may occur. The precise arrangement of atoms in the crystal structure determine the intensities of the diffracted waves. However, most materials are not single crystals, but polycrystalline aggregates or powders and therefore composed of various small crystallites in all possible orientations. Thus, to detect all randomly oriented crystallites and for the X-ray beam to see all possible inter-atomic planes, the experimental angle should be systematically changed. Only then can all possible diffraction peaks from the powder be detected.

For this reason different diffractometers were chosen for characterisation of powdered and bulk samples;

The diffractometer used in Chapter 3 for characterisation of the powdered electrocatalysts was a Huber G670 Guinier camera, (operated in transmission mode). Preparation of a powdered sample requires a thin layer of previously ground (if needed) catalyst mounted on scotch tape and attached to a sample holder. An ideal powder sample should have many crystallites in random orientations, as large and non-random crystallites lead to peak intensity variation. Consequently with such samples the measured diffraction pattern will be different from an ideal powder and will not agree with a reference database. For the best result crystallites should be $< 10\mu$m in size. The Cu Kα1 radiation source from a focusing quartz monochromator was applied with an imaging strip covering an interval from 5 to 100 degrees detection.

For bulk samples (Chapter 4) and thin film samples (Chapter 5) a Bruker D8 diffractometer with GADDS Area Detector was used. The most significant feature of this instrument is the inclusion of a Vantec 2000 2D detector which allows a large range of diffraction spaces to be observed simultaneously in addition to real-time imaging of multiple Debye diffraction rings. In the current study data was collected using Copper Kα radiation and a 15-75 degrees window in the 2θ range. Furthermore, for the bulk samples a Eularian cradle sample stage was used to spin the sample thereby increasing the amount of scattered X-rays observed in Debye diffraction rings. This methodology also increases the number of crystallites contributing to the measured pattern.

2.2 Electron microscopy

Electron Microscopes were developed due to overcome the magnification limitations of Light Microscopes (approximately 0.2 micrometers) and as a result of the desire to see the fine detail of various interior structures (requiring magnification of approximately 10,000x). In general, electron microscopy allows investigation of the morphology of materials and in case of particulate electrocatalysts, determination of size and shape. There are two common types of electrons microscopes. They operate in transmission and scanning mode, TEM and SEM respectively. Both techniques use accelerated electrons (in a vacuum) to create an image of the specimen. Electromagnetic and/or electrostatic lenses are used to control the path of the electrons. The resolution of a microscope is directly related to the wavelength of the irradiation used to form the image. The faster the electrons travel, the shorter their wavelength and the higher the resolution achieved. Increasing the acceleration voltage of the electron beam will in turn increase the resolution of the microscope.

The current passes through the electromagnetic lens (solenoid) inducing an electromagnetic field (Figure 2.2 and 2.3). Subsequently the electron beam passes through the centre of solenoids and down the column of the electron microscope towards the sample. Electrons in the microscope are controlled by changing the current through the lenses which are extremely sensitive to magnetic fields.

2.2.1 Transmission electron microscopy

Transmission electron microscopy (TEM) is used to analyse the microstructure of materials down to the atomic scale resolution, by utilization of a high energy electron beam which is transmitted through a very thin sample. The electrons in this technique are accelerated at several hundred kV and the resolution that can be attained is limited to approximately 1-2 Å. During the TEM imaging an individual layer of atoms are not observed, but rather many layers of atoms, even for very thin samples. The crystal lattice of a material is measured as an interference pattern between the transmitted and diffracted beams which allows the observation of planar and line defects, grain boundaries and interfaces, etc. The bright-field/dark-field imaging modes combined with electron diffraction also provide information about morphology, crystal phases and defects of a specimen [106]

Correct preparation of a specimen for TEM is critical and can take significant time. Samples must be approximately 1000 Å or less in thickness in the area of interest and 3 mm in diameter, due to equipment limitations. For powders one preparation possibility involves direct deposition onto a TEM-thin substrate. It may require grounding with a mortar and pestle

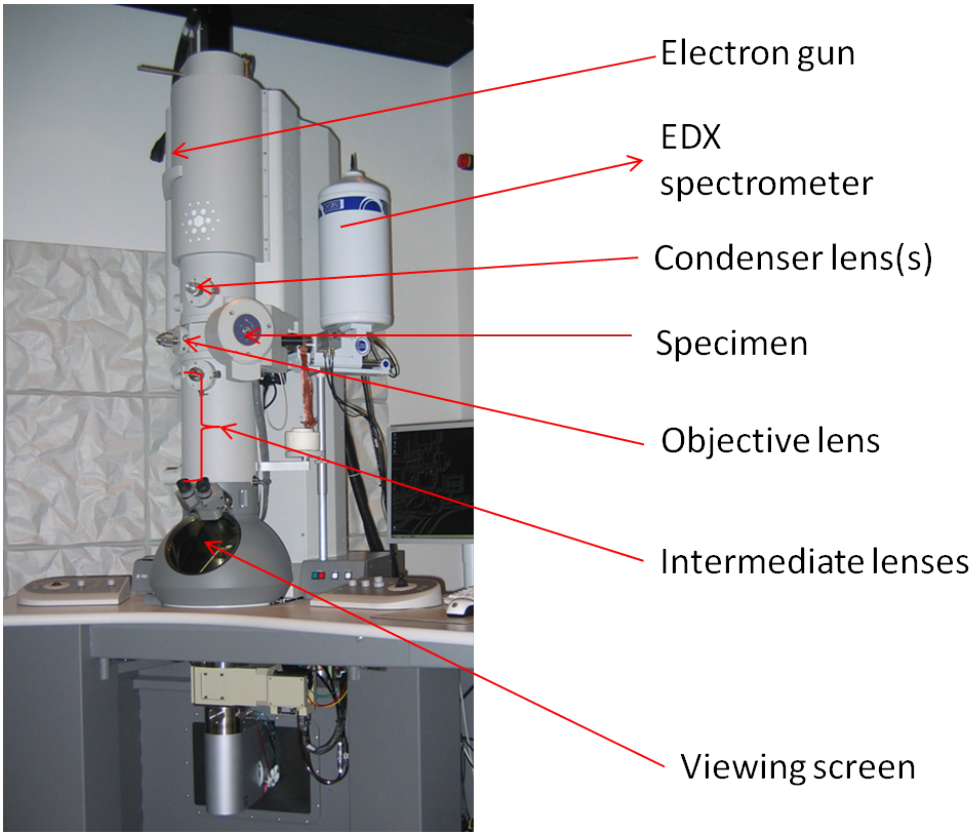

Figure 2.2: Transmission electron microscopy (TEM) setup overview.

to attain the correct particle size (approximately 500 nm or less) and removal of undesirable components (e.g. dust, etc.) using a solvent (typically ethanol or a mixture of the isopropanol and water). Use of a solvent also helps to disperse the powder on the sample holder (typically a carbon coated grid, such as Carbon Film 200 Mech Cu (50)) by submergence. For some samples additional sonication in a dispersant solution is required. Afterwards, the grid hosting the deposited sample is dried in air.

The TEM (Technai T20) used in Chaper 3 is shown in Figure 2.2. The TEM was operated using an accelerating voltage between 80 and 200 kV. The electron source was thermionic LaB6 and the optimal resolution 0.24 nm at 200 kV in bright-field. Imaging was conducted with a Gatan 894 2K UltraScan 1000 camera and 2K UltraScan 1000 FT camera detectors.

2.2.2 Scanning electron microscopy

Unlike TEM, scanning electron microscope (SEM) resolution is approximately one order of magnitude lower than the TEM resolution. Consequently areas ranging from approximately 1 cm to 5 microns in width can be imaged in scanning mode. However, SEM imaging

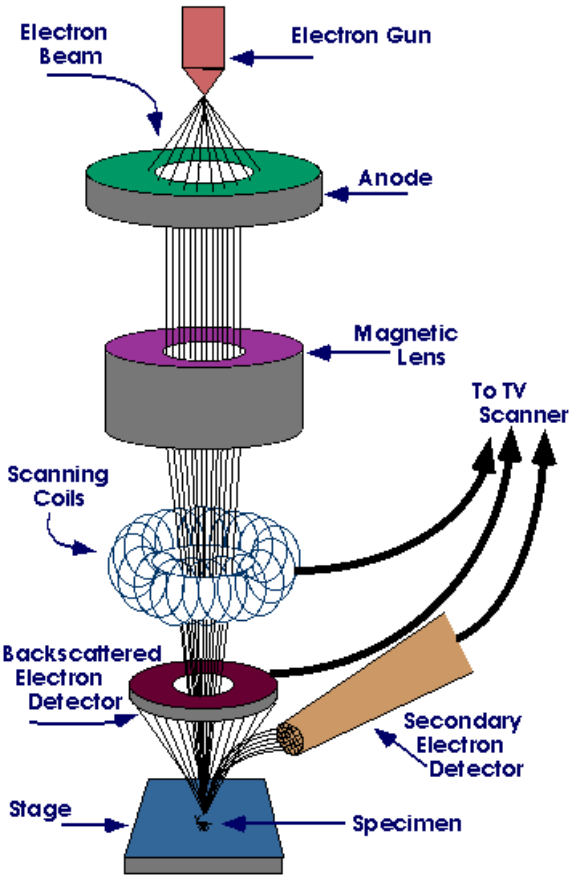

Figure 2.3: Scanning electron microscopy (SEM) schematic overview. Adopted from http://www.purdue.edu/rem/rs/sem.htm

relies on electron interactions at the surface rather than transmission and therefore it is most suitable for imaging of bulk samples. In addition it has a much greater depth of view then TEM, and can produce images that accurately represent the 3D structure of the sample, providing topographical information about the surface.

A schematic overview of the SEM gun is represented in the Figure 2.3. When using SEM an image is produced by excitation of a narrow electron beam onto the sample surface. This yields secondary or backscattered electrons which are emitted from the surface. Secondary electrons are most useful for checking the morphology and topography on samples. In contrast backscattered electrons are most useful for illustrating contrasts in composition in multiphase samples which is a result of heavy elements being more efficient scatterers making the image appear brighter [107].

The SEM used for bulk sample characterisation in Chapter 4 was a JEOL 6320FV Field-Emission High-resolution SEM. All metals are conductive and therefore require no preparation before being used. Non-metals however must be covered by a thin layer of conductive

material in order that they can be imaged. In the case of Chapter 4 no ”sputter-coating” was used.

2.2.3 Energy dispersive X-Ray spectroscopy

TEM and SEM are usually also capable of performing analyses of selected point locations on a sample when equipped with an Energy Dispersive X-ray Spectrometer (EDS, sometimes also referred as EDX) analyser. This technique is especially useful for qualitative or semi-quantitative chemical composition determination (except for elements with atomic number less than 5, such as: H, He, Li, or Be). In addition this technique can provide information on a samples elemental spatial distribution and relative abundance. EDS works by measuring the interactions between electromagnetic radiation and matter. X-rays emitted by the matter in response to collision with charged particles is analysed.

In Chapter 3 powdered samples were analysed using an EDS spectrometer - Oxford Instruments 80 mm2 X-Max SDD, MnKα resolution at 124 eV equippen in the Technai T20 TEM. The use of EDS in conjunction with TEM is sometimes adversely affected by correction factors due to the thin samples, very weak beam broadening (due to high spatial resolution with a beam diameter of few nm) and the use of high energy may give rise to artifacts.

In Chapter 4 the EDS equipped on the JEOL 6320FV Field-Emission High-resolution SEM was used to determine the compositions of the bulk samples. The spectra were collected up to levels of 10 keV for 10 min. Final results were collected from the average of three different spots on the sample.

EDS scans in SEM and TEM were thoroughly analysed and averaged from a large range of different sample positions.

2.3 Cyclic voltammetry

When studying a catalyst, cyclic voltammetry is a readily available technique which can be used to evaluate the surface composition, uniformity and surface area of a sample, etc. It is nearly always the technique of choice when making an initial study of a system [108].

In cyclic voltammetry, the potential applied to the working electrode is swept linearly with time between two chosen limits with a constant scan rate (Figure 2.4), while the response of current, i, is recorded as a function of the potential, E. Oxidation and reduction can be studied by adjusting the potential. During this process the electrons are transferred between the electrode and the molecules in the electrolyte. Figure 2.5 is a typical cyclic

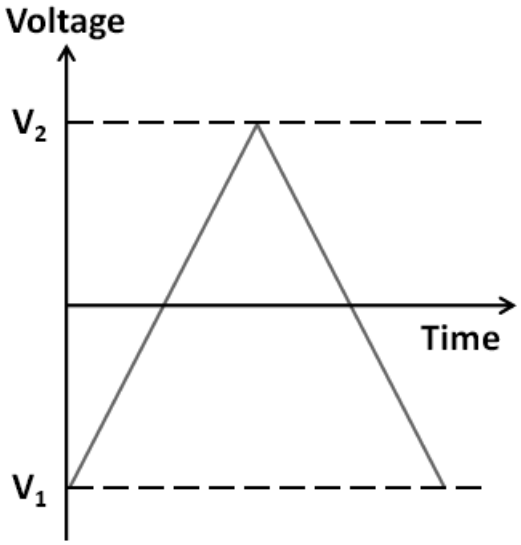

Figure 2.4: Typical cyclic potential sweep. Potential (V) vs. time. (s)

voltammogram of Pt/C in Ar-saturated 0.5 M H_2SO_4 at sweep rate 50 mV/s, recorded from 0.05 V to 1.25 V vs. RHE - forward scan and swept back form from 1.25 V to 0.05 V vs. RHE - backward scan.

There are generally three regions which can be distinguished in a metal CV;

First the hydrogen region *a* (Figure 2.5), where potentially increased hydrogen atoms are oxidized on Pt surface to form H^+ Subsequently H^+ is desorbed from the Pt surface (forward scan), and adsorbed on to the Pt surface (backward scan), following the reaction:

$$Pt + H^+ + e^- \rightleftarrows Pt - H_{ads} \tag{2.2}$$

Peaks (i) and (ii) are assigned to weakly and strongly bound hydrogen [109]. Using the ability of Pt to adsorb one hydrogen atom, the electrochemical surface area (ECSA) of a metal can be evaluated in acidic media, when the charge is passed to form a hydrogen monolayer.

The Pt-mass based ECSA (known as the nanoparticle dispersion) of a Pt nanoparticle catalyst can be calculated from; the charge density (q_{Pt}, mC) obtained from the cyclic voltammetry measurement, the charge required to reduce a monolayer of protons on Pt (Γ_H, 210 μC/cm^2) and the Pt catalyst loading in the electrode (L, g$_{Pt}$/cm$^2{}_{electrode}$) [110]:

$$ECSA(cm^2_{Pt}/g_{Pt}) = \frac{q_{Pt}}{\Gamma_H \cdot L} \tag{2.3}$$

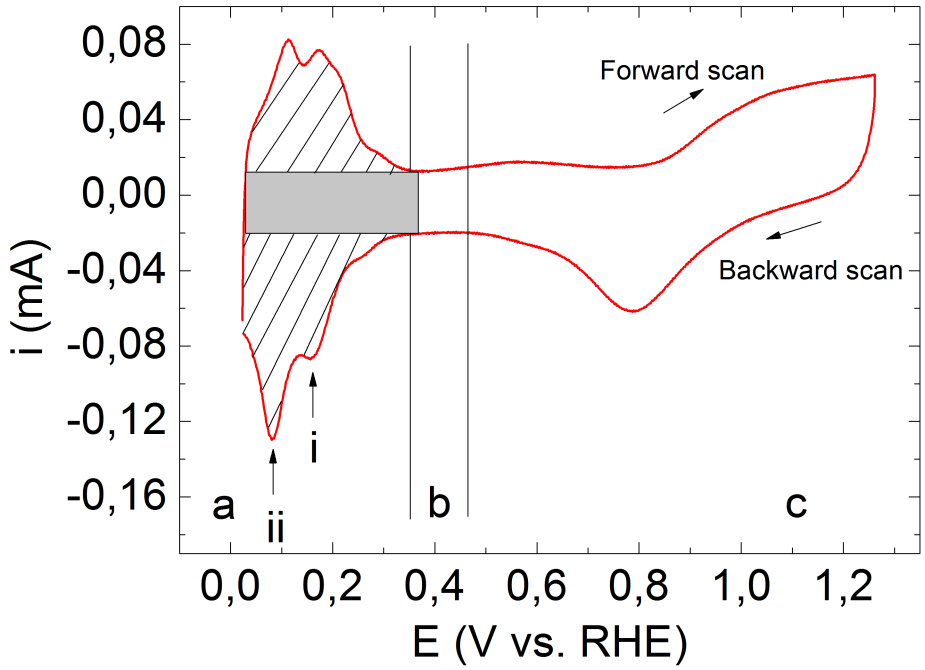

Figure 2.5: Typical cyclic voltammogram of Pt/C in Ar-saturated 0.5 M H_2SO_4 at 50 mV/s sweep rate.

The Pt surface area-specific activity (total ECSA) of either nanoparticle or bulk Pt catalyst can be calculated the same way. The only difference is the geometric area of the electrode (A, cm^2) is used for the calculations, instead of the Pt catalyst loading in the electrode (L, $g_{Pt}/cm^2{}_{electrode}$).

Generally adsorption peaks or the average of adsorption and desorbtion peaks are used for calculation of the ECSA (following subtraction of the double layer capacitive current). The electrical charge induced by double layer charging must be accounted for in the analysis to avoid overestimating the charge attributed to the electro-catalytic activity.

In the double layer region (region *b*, Figure 2.5), no electrochemical reaction occurs and the current recorded is due to the accumulation of the charges from the electrolyte of the polarised interface [108]. For the Pt catalysts supported on carbon, due to the large carbon surface area, double area capacitive current can also take place on carbon and estimated to be 8 ± 2 µF/cm^2 for Vulcan carbon [111].

In the oxide region (region *c*, Figure2.5), oxygen chemisorbtion takes place and oxides are formed following the reactions:

$$Pt + H_2O \longrightarrow Pt - OH_{ads} + H^+ + e^- \tag{2.4}$$

$$Pt - OH_{ads} \longrightarrow PtO + H^+e^- \tag{2.5}$$

Oxygen adsorption becomes increasingly irreversible (forward scan) as potential increases. Consequently reduction of the oxide layer is observed and finalized by oxide stripping (backward scan), when reversing the sweep direction.

2.4 CO electro-oxidation voltammetry

Carbon monoxide electro-oxidation is the most of the widely studied species in surface science.

The electro-oxidation of CO on Pt follows the reaction [32, 108]:

$$Pt - CO + H_2O \longrightarrow Pt + CO_2 + 2H^+ + 2e^- \tag{2.6}$$

Figure 2.6 show a typical cyclic voltammogram of Pt/C in Ar-saturated and CO-saturated 0.5 M H_2SO_4 at sweep rate 20 mV/s, recorded from 0.05 V to 1.3 V vs. RHE. As can be seen from the voltammogram, when the Pt surface is poisoned by CO, the current density is very small and the voltammetric features at low potentials are minimised (in the absence of the hydrogen desorption peaks). This is caused by CO strongly bonded to active Pt sites, preventing hydrogen adsorption at low potentials. CO electro-oxidation begins at $\backsim$ 0.68 V (vs. RHE). The position of the CO electro-oxidation peak depends on the nature and physical/structural properties of the catalyst surface [32, 112, 113]. Sometimes a small pre-peak can be observed prior to the main CO adsorption in a voltammogram. This feature can only be detected when all Pt surfaces become saturated with CO at low adsorption potentials. It has been suggested this is caused by weakly bonded CO molecules on the Pt surface of the adlayer [32].

The area under the CO stripping peak can also be used to calculate the electrochemical surface area of Pt:

$$ECSA(cm^2_{Pt}/g_{Pt}) = \frac{q_{Pt}}{\Gamma_{CO} \cdot L} \tag{2.7}$$

Since CO oxidation is a 2-electron process and assuming that CO forms a complete monolayer on the Pt disc, the charge it takes to oxidise one monolayer on one centimetre is equal to Γ_{CO}, 420 μC/cm^2, therefore ECSA can be calculated in a similar manner to that of hydrogen adsorption/desorption cyclic voltammogram.

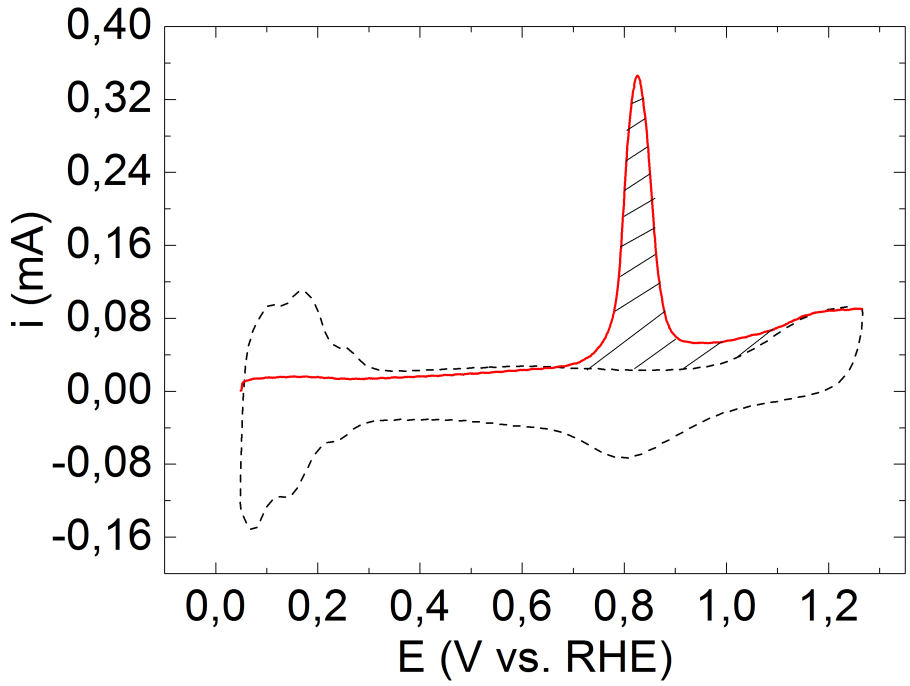

Figure 2.6: Typical CO stripping electo-oxidation voltammogram of Pt/C in Ar-saturated and CO-saturated 0.5 M H_2SO_4 at 20 mV/s sweep rate.

2.5 Rotating disk electrode

The rotating disk electrode (RDE) is a convective electrode technique of significant electrochemical importance for reactions that involve mass transport [21,30]. The advantage of this technique is that the steady state is achieved more rapidly than when using stationary electrodes. In this technique mass transfer to the electrode surface is faster as it is not determined by diffusion. When convection is present current densities 3-100 times greater than steady state diffusion can be achieved. As influence of mass transfer to electron-transfer kinetics is smaller than in the case of stationary electrodes, this technique can be used to study the fundamental kinetics of the oxygen reduction reaction. In addition the RDE technique is much simpler to implement and interpret than analogous electrochemical characterization methods in a PEM fuel cell, which can be time consuming and cumbersome. For these reasons RDE is often used to rapidly screen a range of catalyst compositions [114].

Figure 2.7 gives a schematic overview of an RDE setup. The RDE used in this work consisted of a flat glassy carbon disk electrode surrounded by an insulating material - e.g. Teflon. The electrode rotates with angular velocity, ω, in the solution along the rotation axis, z, which is perpendicular to the electrode surface. When the electrode spins it drags

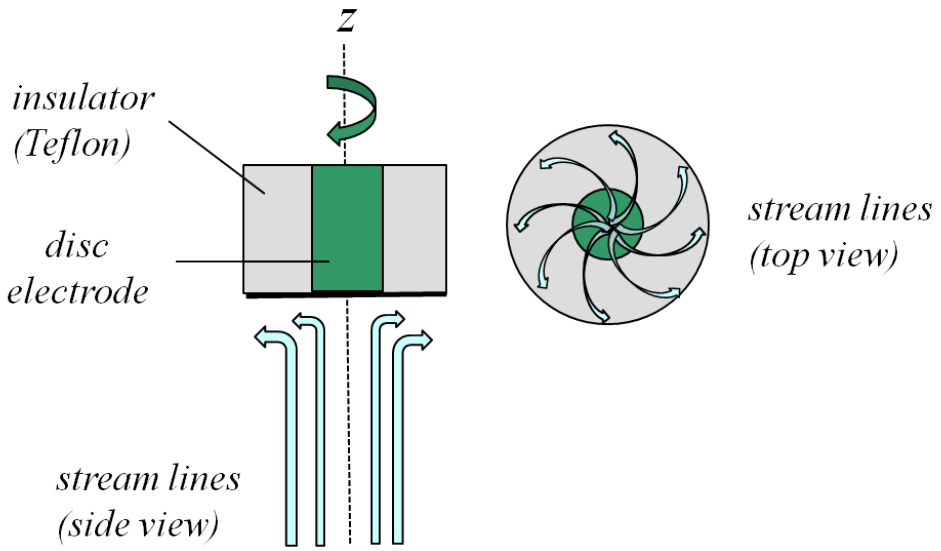

Figure 2.7: Schematic representation of rotating disc electrode and the radial flow of liquid (stream lines) during rotation. Side and top view.

the electrolyte to the surface of the electrode and the product is spun out from the surface of electrode, acting as a pump.

Consequently the electrolyte is divided into two zones [115]. The first region is a thin stagnant boundary layer covering the surface of the electrode with thickness δ. Here the reactant transports through this layer by diffusion, for which is the only mode of mass transport. A second reaction occurs outside of the thin layer area. Here strong convection occurs and all species concentrations are constant. Besides the electrolyte, reacting gas is purged in to the electrochemical cell to allow the oxygen reduction reaction mechanism to be measured. In combination with the slow electrocatalystic activity of the catalyst this gives a loss in the rate of electrochemical reaction. Therefore RDE helps to avoid poor mass transport of the reacting gas and allows precise quantification of electrocatalytic activity. The thickness of the surface layer, velocity of the electrolyte solution flow and flux of the gas flow to the electrode surface is precisely controlled by the rotation rate of the disc (100 - 5000 rpm). Therefore, the measured current i, the kinetic current i_k and the mass transport limited current i_D results in the Koutecky-Levich equestion:

$$\frac{1}{i} = \frac{1}{i_k} + \frac{1}{i_D} = \frac{1}{i_k} + \frac{1}{Bc_0\omega^{1/2}} = \frac{1}{i_k} + \frac{1}{0.62nFD^{2/3}\nu^{-1/6}\omega^{1/2}C_O^{\infty}} \tag{2.8}$$

where n is the number of transferred electrons, F is the Faraday constant, C_O^{∞} is the concentration of dissolved gas species (O) in the bulk solution, D is the diffusion coefficient

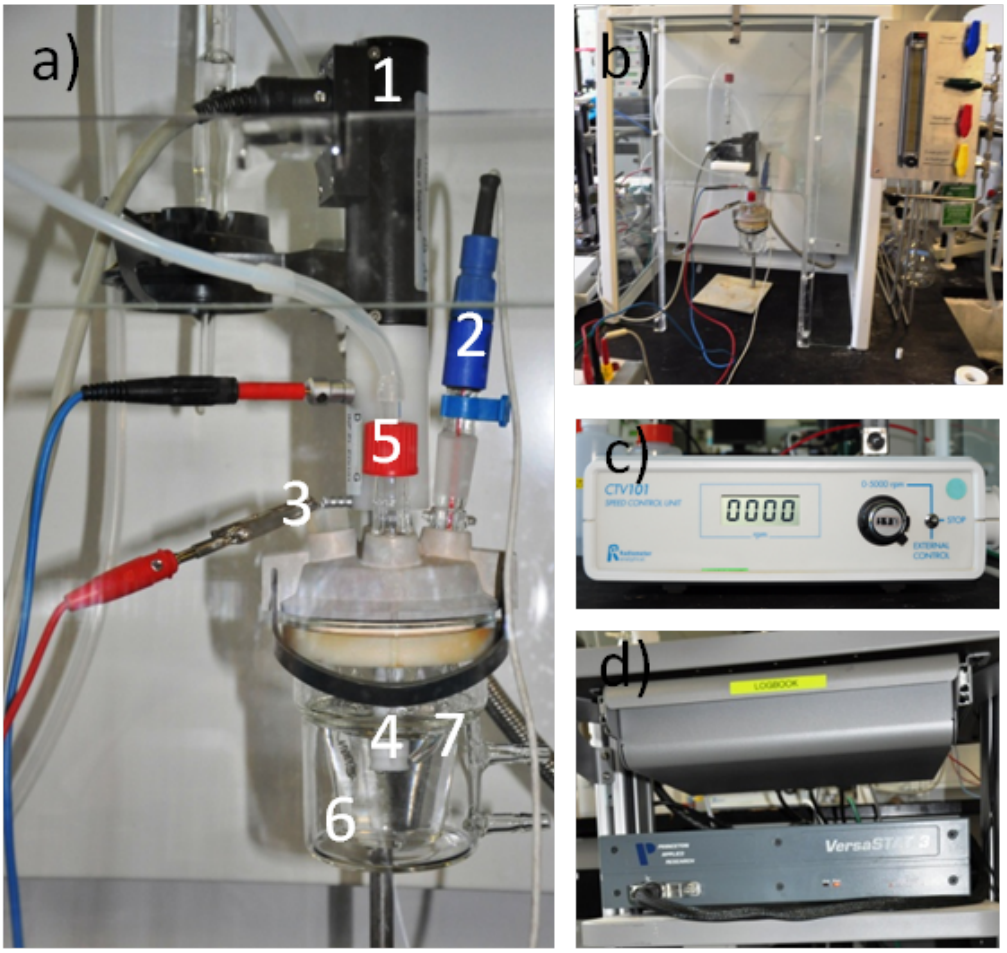

Figure 2.8: Rotating disk electrode setup: detailed view - a), setup overview - b), speed control unit - c), and potentiostat Versastat 3 - d).

of the gas, ν is the kinetic viscosity of the electrolyte and ω is the rotation rate. Plotting $\frac{1}{i}$ vs. $\frac{1}{\omega^{1/2}}$, what is known as the Koutecky-Levich plot, will generate a graph with a y-axis given by the value of $\frac{1}{i_k}$, and the slope $\frac{1}{Bc_0}$. Then the kinetic current i_k of the electrode can be determined and the number of transferred electrons can be found from the slope ($1/Bc_0$).

2.6 Rotating disk electrode setup

Figure 2.8 shows the rotating disk electrode (RDE) setup which was used for the electrochemical characterization and stability measurements at the Technical University of Denmark (detailed view - a), setup overview - b), speed control unit - c), and potentiostat Versastat 3 - d)).

A typical commercial three compartment glass cell from Radiometer Analytical (6) was used to create a three electrode setup with Pt wire as a counter electrode (3) and a saturated calomel electrode (Radiometer Analytical, REF421) as a reference electrode (2). The reference electrode was placed in a custom-made Luggin capillary filled with the electrolyte solution (7). The working electrode was a commercial glassy carbon electrode (GC electrode) from Radiometer Analytical (4) with a diameter of 5 mm. The electrolyte was purged with various gases through a frit (5). Radiometer Analytical rotator (1), Radiometer Analytical CTV101 speed control unit (controls the EDI101 rotation speed up to 5000 RPM) (c) and commercial potentiostat Versastat 3 (Princeton Applied Research) and were used during the conduct RDE experiments.

The RDE measurements were conducted in a 0.1 M $HClO_4$ electrolyte solution, prepared by dilution of 70-72 % $HClO_4$ (Sigma-Aldrich, 311421) with DI water. During gas purging the working electrode was kept outside the electrolyte. The working electrode was immersed into the electrolyte under potential control (0.06 V vs. RHE) and electrochemical measurements were started immediately. All measurements were conducted at room temperature.

2.7 Reference electrode calibration

In all measurements a saturated salomel electrode (SCE) (Radiometer Analytical, REF421) was used as the reference electrode. SCE was calibrated with respect to the potential of the Reversible Hydrogen Electrode (RHE). Calibration was performed in a high purity hydrogen saturated 0.1 M $HClO_4$ electrolyte with a Pt disk (Radiometer Analytical, A35T105) as the working electrode. Cyclic voltammetry (CV) was run at a scan rate of 10 mV/s and rotation speed of 1600 rmp. Subsequently the average of the two potentials at which the current crossed zero was taken to be the thermodynamic potential for the hydrogen electrode reaction. An example of the reference electrode calibration CV is shown in Figure 2.9.

2.8 Oxygen reduction reaction activity using cyclic voltammetry

For determination of the activity for the oxygen reduction reaction (ORR), cyclic voltammetry (CV) measurements were conducted using the RDE technique as shown in Figure 2.10. The intrinsic kinetic current at 0.9 V vs. RHE was separated from the mass transport diffusion limiting current between 0.2 and 0.5 V vs. RHE. All CV measurements were performed with a the rotating speed of 1600 rmp (revolutions per minute) and a scan rate of 10 mV/s

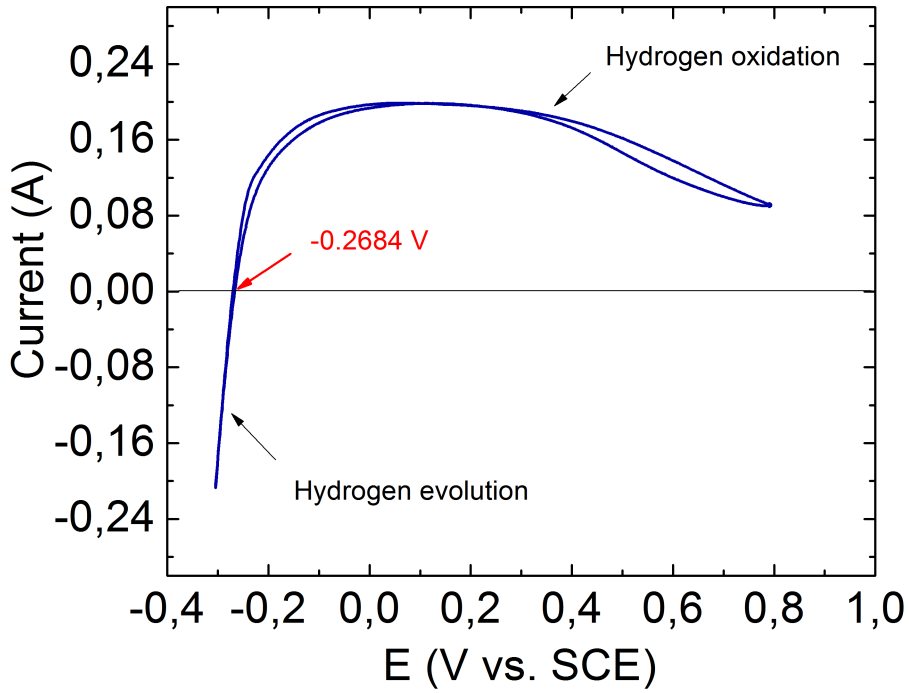

Figure 2.9: Typical reference electrode correction method. H_2-oxidation on Pt disk electrode at 1600 rmp in H_2 purged 0.1 M HCl_4.

in 0.1 M $HClO_4$ electrolyte purged with oxygen for at least 30 min at room temperature. All CVs were performed from the 0.06 vs. RHE potential to the open circuit potential to around 1.1 V vs. RHE. Positive going scans were then taken as the determinative once when comparing the measurements (Figure 2.10).

The Koutecky - Levich plot was found using the variation in rotation speed in a range between 400 and 2500 rpm in 0.1 M $HClO_4$ purged with oxygen for 30 min at room temperature. All reported activities were compared at 0.9 vs. RHE.

2.9 Electrochemical long-term durability experiments

In order to simulate long-term behaviour of the fuel cell electrocatalysts stability tests were performed with cycling voltammetry (CV) accelerated degradation tests. Experiments were conducted in 0.1 $HClO_4$ purged with Nitrogen for at least 30 minutes at room temperature.

2000 voltage cycles were performed form 0.06 to 1.0 V vs. RHE at scan rate 20 mV/s. During the run-time three CVs from 0.05 V to 1.0 V vs. RHE at scan rate of 10 mV/s were performed in each case after 500, 1000, 1500 and 2000 voltage cycles to determine the

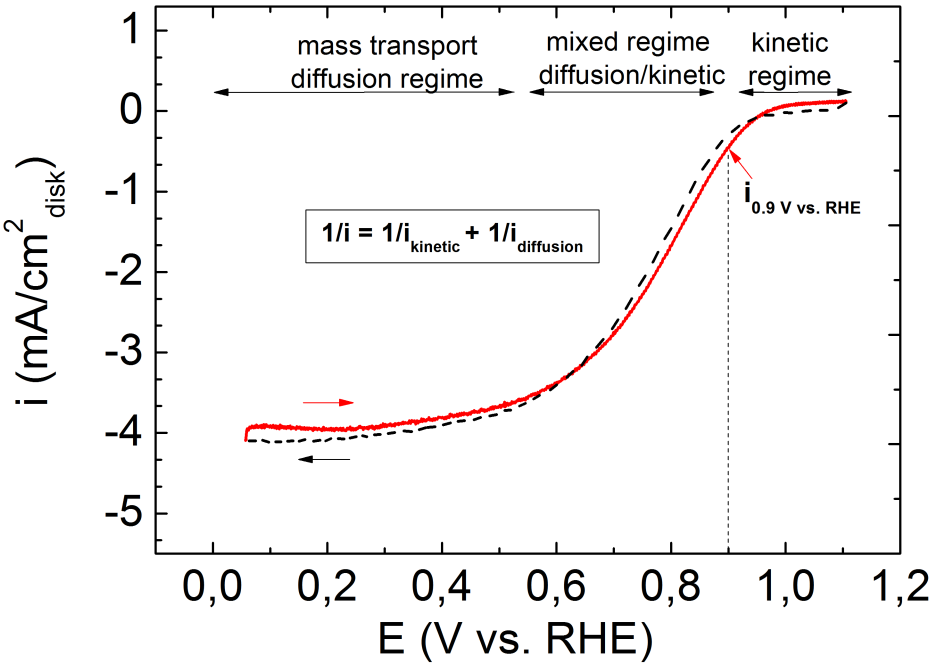

Figure 2.10: Analysis of a cyclic voltammogram sweep of Pt/C, 0.06 -1.1 V vs. RHE, 10 mV/s, 1600 rmp in oxygen saturated 0.1 $HClO_4$ at room temperature. Positive going scan - red line, negative going scan - black dash line

platinum electrochemical surface area (ECSA) prior to and post degradation cycling. The full procedure for potential cycling or durability degradation is shown schematically in 2.11.

2.10 Importance of the glassware cleaning for the high standard electrochemical measurements

It is essential in order to attain reproducible measurements of Pt specific activity to thoroughly clean the electrochemical cell (including glassware, stoppers, and o-rings) in order to remove cationic, anionic, and organic impurities. It is especially important when conducting oxygen reduction electrochemical measurements for a polycrystalline Pt disk or evaluating a low-surface-area catalyst. Polycrystalline Pt specific activity at E = 0.90 V should be approximately 1500-3000 $\mu A/cm^2$ [116]. In the current study the following methods were used to clean glassware.

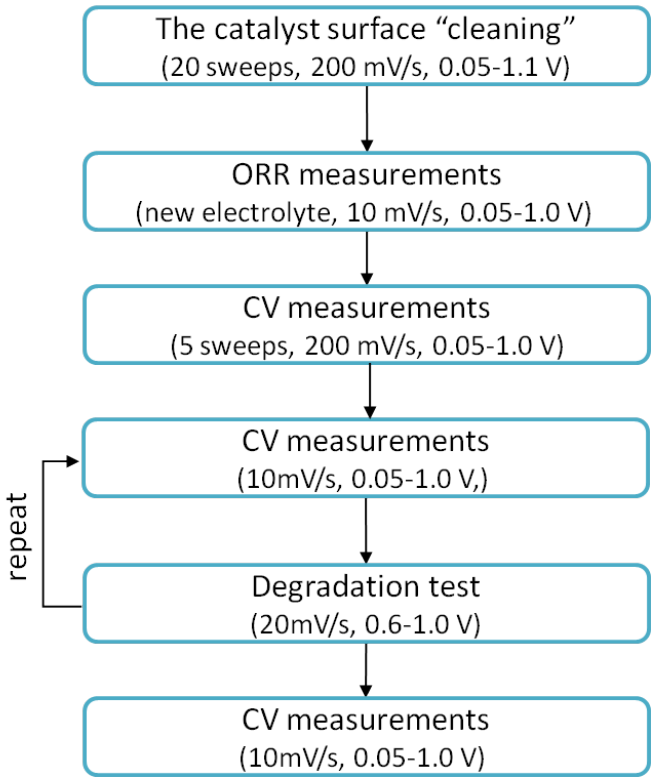

Figure 2.11: Schematical description of the long-term durability testing procedure.

Cleaning procedure for glassware

1. Rinse glassware with DI water (it might be necessary to use laboratory detergent before) and sonicate it in DI water to remove visible dirt.

2. Fill cell with 2/3 DI water and 1/3 of a suitable acid (can be sulphuric acid or other ratios). Soak for 1-2 hours in fume hood. Rinse with DI water. This step removes metal cations.

3. Fill cell with 2 M KOH (purity >90 %, flakes). Soak for 1-2 hours in fume hood. Rinse with DI water. This step removes organics and acids. It also corrodes the glassware!

4. Put glassware in larger beaker, fill with DI water and bring to boil. This step removes leftover KOH from previous step.

5. Test glassware and repeat/optimize procedure if necessary.

It is recommended to use this method weekly or monthly if the glassware is contaminated or when testing low surface area electrodes. It is also possible to use more simplified methods, described below.

Simplified cleaning method

Fill the electrochemical cell is with ∼100 mL of concentrated H_2SO_4 and leave it to soak overnight. Subsequently rinse at least 8 times with DI water

It is also recommended to keep the electrochemical cell and the glassware (used for electrochemical measurements) submerged in a DI filled reservoir between measurements, to prevent contamination. When using this method the DI water should be changed each time the cell is used in addition to comprehensive rinsing of the glassware following removal.

Polycrystalline Pt disks are highly sensitive to impurities. Thus, achievement of ORR activities comparable to the standard values for the polycrystalline Pt [34,64,117,118] indicates one has met or exceeded the cleanliness levels needed to obtain reliable data.

Chapter 3

PBI wrapped graphene as platinum nanoparticle based support

3.1 Introduction

As discussed briefly in the introduction, an increasing focus is being given on exploring the potential use of graphene supports in catalysis. This focus is a result of their favourable structure and electrical properties which act to enhance activity and stability of the catalyst [92–94].

Graphene has clear advantages compared to other carbon sources, e.g. carbon nanotubes or nanofibers. Graphene consists of atom-thick sheets of sp^2-bonded carbon, packed in a honeycomb structure. It possesses a high theoretical surface area (up to 2600 m^2g) and a high electronic conductivity (10^3-10^4 S/m). Furthermore graphene is an inherently mechanically and thermally stable, durable 2-D support. However, unfortunately Pt nanoparticles are difficult to deposit directly or evenly onto non-functionilized graphene surfaces (which do not have active functional groups). Moreover, Pt nanoparticles are readily sintered and detached and/or dissolved from such a support by ultrasonic or high speed agitation treatment employed during catalyst ink preparation. Therefore the observed low affinity between Pt and carbon atoms requires further investigation. These investigations should aim to obtain chemical and/or physical functionalization methods able to obtain high dispersion and homogeneous loading of Pt nanoparticles on the surface and determine methodologies which reinforce the binding strength between Pt and graphene. Chemical functionalization gives the prospect of Pt deposition on graphene by generation of functional groups. These strategies are effective, however an overall methodology has not yet been finalized. Furthermore chemically functionalized graphene surfaces (mostly formed by hush oxidative treatment)

are still easily destroyed reducing conductivity and durability of the support. Thus, when such a catalysts is used in the acidic environment present in PEMFCs it results in a low output performance.

Recently, many studies on CNTs and graphene have focused on their treatment by physical functionalization methods, such as introducing polymers on their surfaces. These methods were subsequently proved to be effective, showing no damage on the support structure whilst giving improved nucleation of Pt nanoparticles onto the inert graphene surfaces. Furthermore these methods also improved Pt nanopartcle distribution on the surfaces and prevented damage of the support material.

Several polymers have so far been investigated; e.g. polyaniline (PANI) [119] and poly(benzimidazole) (PBI) [120].

For PEMFCs with poly(benzimidazole) (PBI) as a membrane, it is favourable to use the same polymer for catalyst support functionalization. Previous studies have shown successful wrapping of CNTs supports by PBI, where the support acts as a highly efficient Pt nanoparticle adsorbent [120]. PBI wrapping has also been found to allow a high Pt loading to be achieved, inducing formation of so called triple-phase boundary nanostructures between CNTs, aromatic nitrogen incorporated in the PBI structure and Pt nanoparticles. This type of interaction induces a high activity towards oxygen reduction in acid media [121], as well as significantly greater durability [122] of CNTs.

While PBI wrapping of CNTs has shown promising results for use as a Pt catalyst support, no studies have currently been published which describe such a methodology for Pt deposited onto a PBI wrapped Graphene support, to the author knowledge at least. Thus, this Chapter will aim to address this gap in the literature and investigates the synthesis of a PBI wrapped Graphene support for use in conjunction with a Pt nanoparticle catalyst (Pt/Graphene-PBI). Characterisation of a bespoke laboratory made catalyst of this nature was undertaken in addition to a comparison between it, Pt deposited onto Graphene (Pt/Graphene) and a commercial 40% Pt/Vulcan XC 72R JM catalyst. Results were obtained for stability of the electrochemical surface area as well as oxygen reduction reaction activity and are subsequently discussed.

3.2 Synthesis of Pt/Graphene-BPI catalyst

Preparation of the Graphene-PBI support

A Poly(benzimidazole) (PBI) wrapped Graphene support was prepared using the following methodology [120]. A PBI (average molecular weight of 23 kDa supplied by Danish Power

Systems ApS) was dissolved in 5 mL of N,N-dimethylacetamide (DMAc, 99%, Sigma-Aldrich, CAS# 127-19-5, Lot# BCBL2233V) with 5.0 mg of Graphene powder added before sonication for 60 min (using a bath-type sonicator). The mixture was filtered and washed with DMAc to remove any unbound PBI. The obtained solid (Graphen-PBI) was dried under vacuum at 60°C for 20 hours.

Catalyst preparation by the polyol method

Synthesis of the Pt supported on Graphene (Graphene Supermarket, 12 nm Flakes, Grade AO-3, SKU SKU-NP-FLAO3-2G) and on PBI wrapped Graphene (or Graphene-PBI) were prepared using the polyol method [121]. This method involves reduction of a Pt precursor (hexachloroplatinic acid), which is subsequently dissolved in ethylene glycol at moderate temperatures. In this case ethylene glycol acts as both reducing agent and solvent, forming CO_2 and H_2O by-products in addition Pt [123] 3.2:

$$\mathrm{CH_2}OH - CH_2OH + 5/xPtO_x \leftrightharpoons 5/xPt^0 + 2CO_{2g} + 3H_2O_g \tag{3.1}$$

Synthesis of the catalysts conducted by dilution of the Pt precursor (H_2PtCl_6, hexachloroplatinic acid, Alfa Aesar, CAS# 16941-12-1; Lot# G19S028) in ethylene glycol (Sigma-Aldrich, CAS# 107-21-1, Lot# BCBH5230V) and NaOH (1.0 g, 1.93 mmol in 50 mL) whilst stirring. Transparent yellow platinum hydroxide colloidal solution was consequently obtained and heated at 160°C for 3 hours, with an N_2 gas flow passing through the reaction system to remove by-products and avoid O_2 exposure. The precursor was fully reduced after 3 hours and subsequently cooled to room temperature, resulting in a transparent dark brown and homogeneous colloidal solution of the Pt metal nanoclusters (Pt: 3.76 g/L, glycol 19.3 mmol/L) with no precipitate.

The resulting solution of Pt nano-clusters was then mixed with a certain amount of supporting material (Graphene or Graphene-PBI) to obtain a 40 wt.% Pt catalysts. Further, 0.1 M solution of HCl was added drop-wise to adjust pH (to pH < 4). The solution was subsequently heated for 3 hours at 90°C. Following the heating phase, the solution was filtered and the final product washed repeatedly with water before oven drying under vacuum at 60° C for 20 hours.

A schematic representation of the complete synthesis process for Pt supported on PBI wrapped graphene is shown in Figure 3.1.

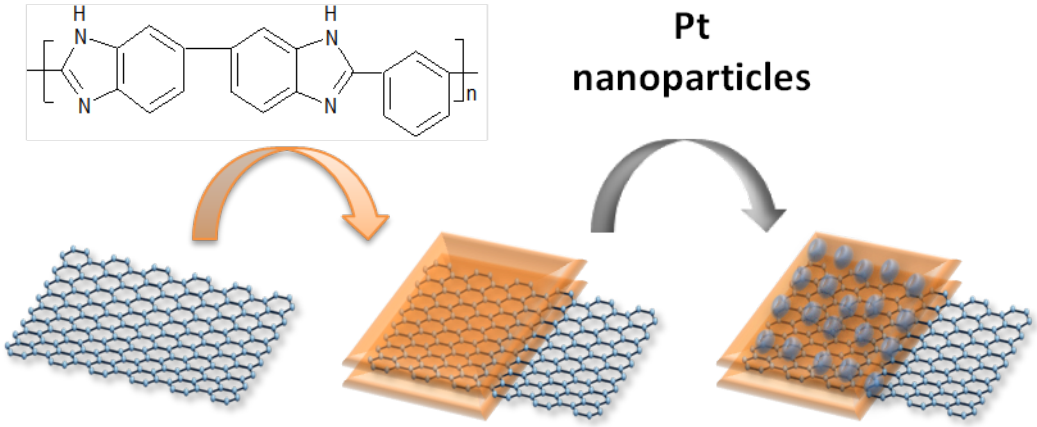

Figure 3.1: Schematic presentation of complete synthesis process for Pt supported on PBI wrapped graphene

3.3 Structural and compositional characterisation

3.3.1 Characterisation of Graphene-PBI support

Synthesized PBI wrapped graphene support was characterized by Attenuated Total Reflectance Fourier Transform Infrared (ATR-FTIR) and TGA/DTA, acquired using a Netzsch STA 409 PC TGA/DTA analysis.

ATR-FTIR spectroscopy was conducted using a Perkin Elmer Spectrum One FTIR spectrometer equipped with a universal ATR sampling accessory. IR spectra for Graphene (blue line), PBI (red line) and Graphene-PBI support (black line) are shown in Figure 3.2. The strong absorption band observed from 2500 to 3600cm^{-1} is most likely a result of the N–H groups of the imidazole ring. Here, the sharp peak centred at around 3420cm^{-1} may correspond to the stretching vibration of the isolated non-hydrogen bonded N–H group. The broad peak with the highest absorption intensity around 3080cm^{-1} can likely be attributed to the stretching vibration of the N–H groups involved in hydrogen bonding. The band at around 1620cm^{-1} usually corresponds to C=N and C=C stretching vibrations. These are the bands which correspond to the functional groups of PBI, thus confirming the desired synthesis was successful [124].

PBI wrapping of the Graphene support was also investigated by TGA and DTA analysis, which are shown in Figure 3.3. Thermograms were recorded at a heating rate of 10°C min in air. The TGA curve of the Graphene-PBI (Figure 3.3 a), black line) shows a two-step weight loss reduction. The first step (approximately 400°C) corresponds to the thermal degradation of the wrapped PBI whilst the second step (approximately 610°C) is attributable to that of the

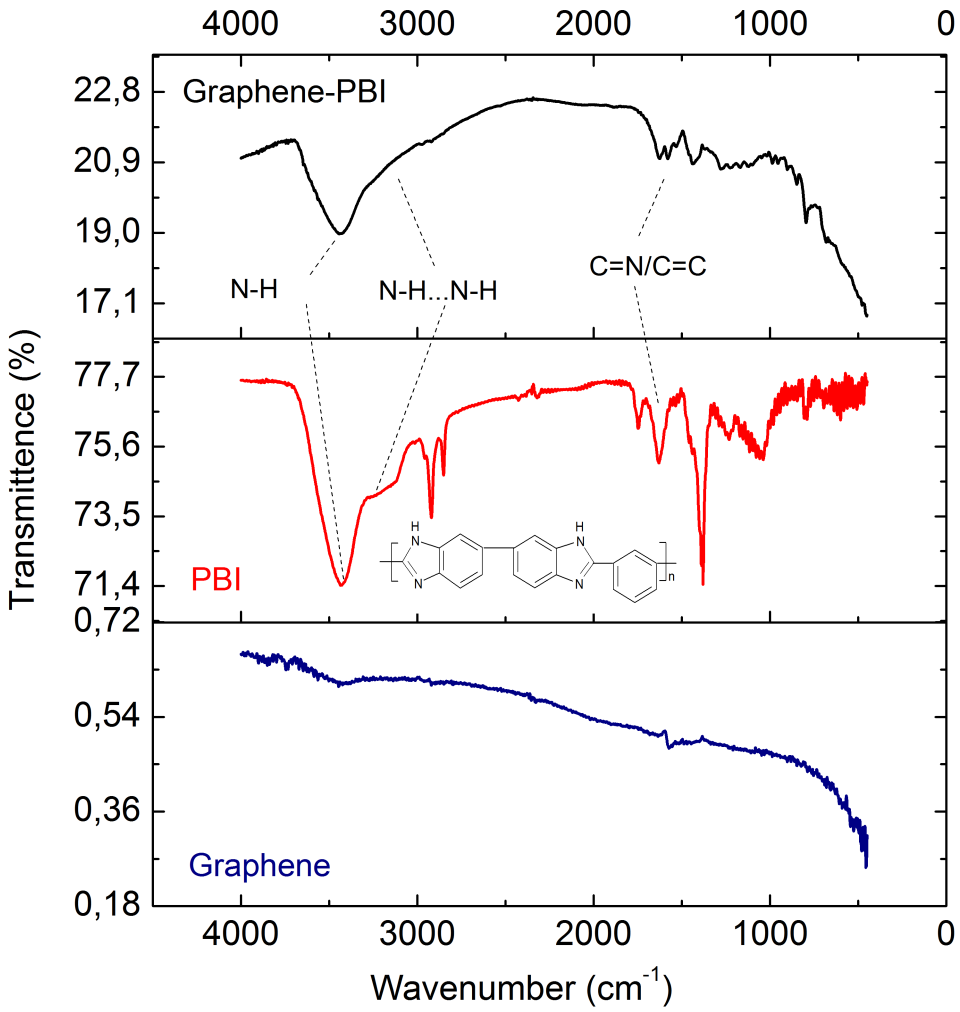

Figure 3.2: ATR-FTIR analysis of Graphene (blue line), PBI (red line) and Graphene-PBI support (black line).

Graphene [120]. The DTA curve of the Graphene-PBI (Figure 3.3 b), black line) follows that of the TGA; exothermic peaks are found centred around 460 and 750°C, corresponding to the PBI and graphene decomposition, respectively. The slight increase in temperature decomposition of Graphene-PBI in comparison to pure Graphene can be attributed to decomposition of the PBI coating.

The TGA curve of Graphene (Figure 3.3 a), red line) shows desorption of water and a broad exothermic peak at approximately 110°C. A further broad exothermic peak is then observed at around 590°C corresponding to decomposition of graphene, confirming the TGA assignment. This TGA/DTA analysis further confirms the presence of PBI wrapping of the graphene support.

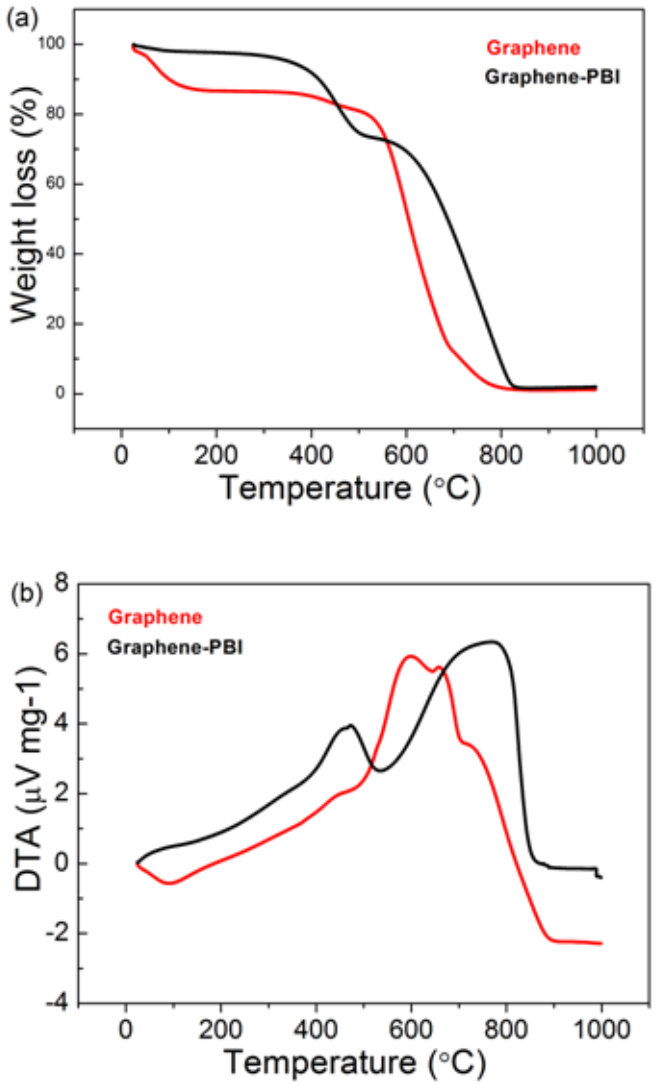

Figure 3.3: Analysis of Graphene (red line) and Graphene-PBI support (black line) TGA - a) and DTA - b).

3.3.2 Characterisation of Graphene-PBI supported Pt nanoparticles

After Pt was loaded onto Graphene and Graphene-PBI supports TEM, XRD and TGA/DTA analysis were carried out in order to fully characterize the catalysts.

X-Ray diffraction profiles of synthesized Pt/Graphene, Pt/Graphene-PBI, commercial 40% Pt/Vulcan XC 72R JM catalysts (for 12 hours) and Graphene-PBI support (for 2 hours) are shown in Figure 3.4. XRD spectra were obtained using a a Huber D670 diffractometer equipped with a Cu-Kα X-ray source for 12 hour.

Two phases were identified for the Pt/Graphene, the Pt/Graphene-PBI. The first phase possesses characteristic peaks of the face centred cubic (fcc) Fm3m space group of platinum, i.e. the (111), (200) and (220) reflections and is also common with the commercial 40%

Pt/Vulcan XC 72R JM. The second phase, typical only for the Pt/Graphene, the Pt/Graphene-PBI and the Graphene-PBI support and is characterized by a diffraction peak at around 2θ 26° likely related to the ordered graphitic structure; consistent with the (002) diffraction peak of an ideal graphite phase. Diffraction peaks of the Pt/Graphene and of the commercial 40% Pt/Vulcan XC 72R JM are sharper than those of Pt/Graphene-PBI indicating a larger crystallite size. Mean metal crystallite sizes for the electrocatalysts (calculated using the Scherrer equation) are given in Table 3.1. The crystallite sizes for 40% Pt/Vulcan XC 72R JM, Pt/Graphene and Pt/Graphene-PBI were 4.9, 5.0 and 2.7 nm, respectively.

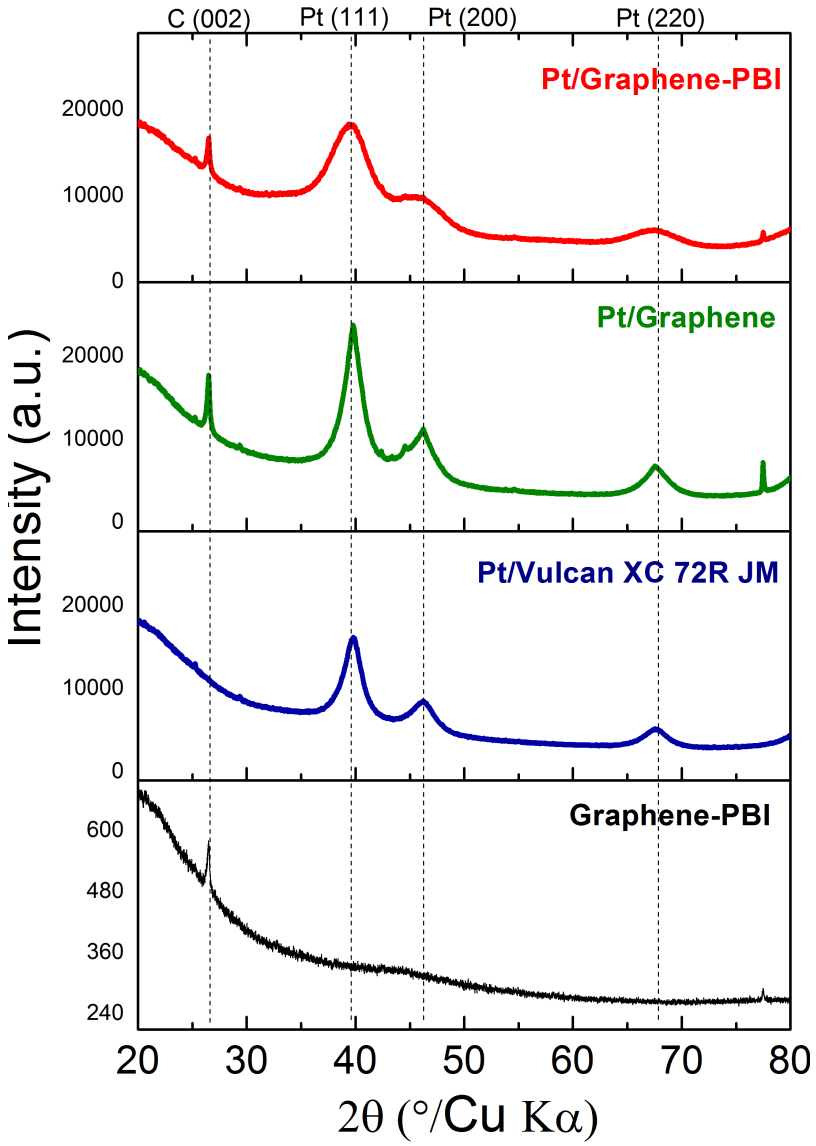

Figure 3.4: X-Ray diffraction profiles for the Pt/Graphene-PBI (red), Pt/Graphene (grean), commercial 40% Pt/Vulcan XC 72R JM (blue) and Graphene-PBI (balck).

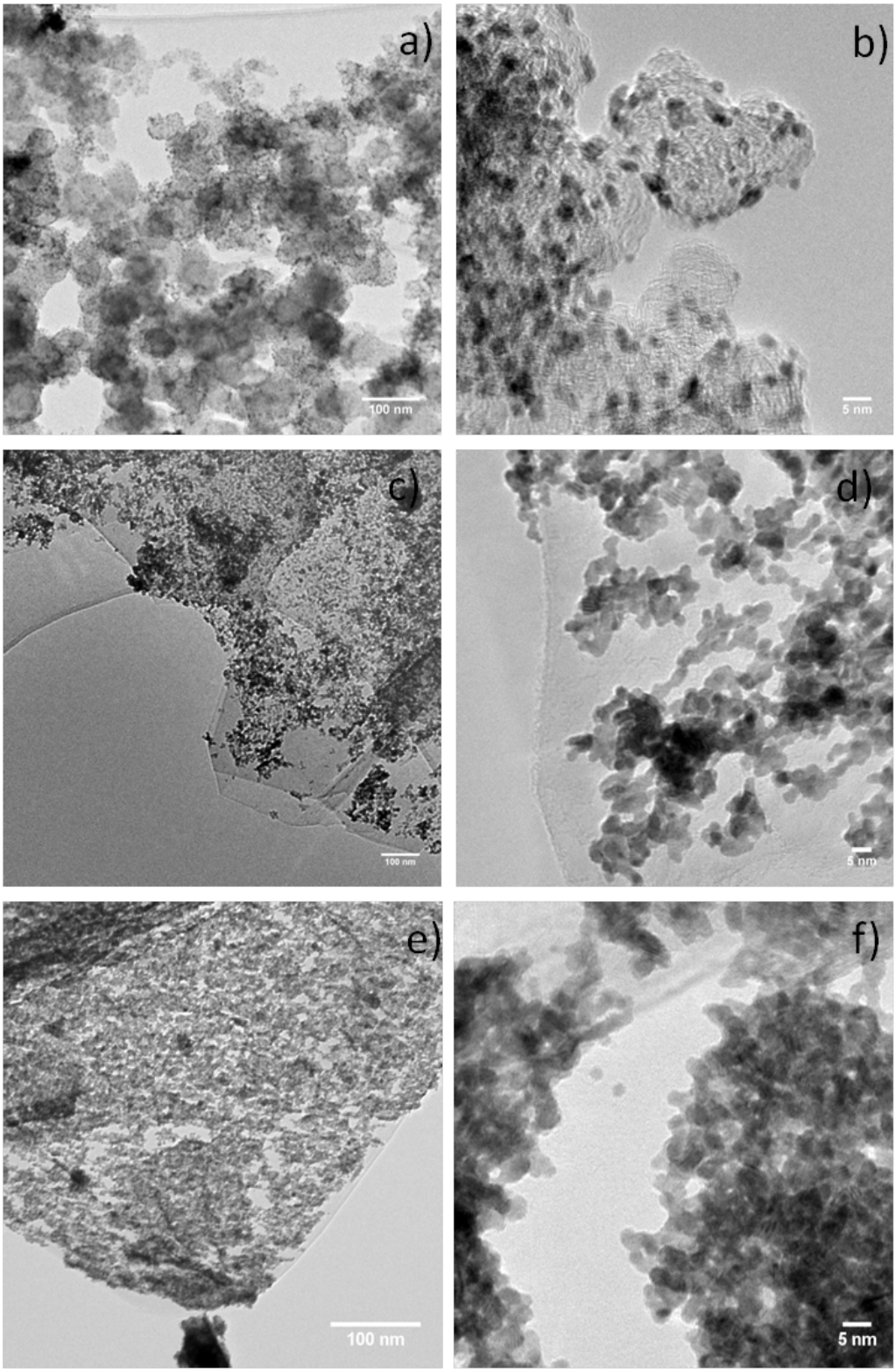

Figure 3.5: Typical TEM images of the 40% Pt/Vulcan XC 72R JM at 100 nm - a) and 5 nm - b) magnifications; Typical TEM images of the Pt/Graphene at 100 nm - c) and 5 nm - d) magnifications; Typical TEM images of the Pt/Graphene-PBI at 100 nm - e) and 5 nm - f) magnifications.

The Pt presence, nanoparticle size, distribution and morphology were further investigated by TEM. Images of the 40% Pt/Vulcan XC 72R JM, Pt/Graphene and Pt/Graphene-PBI at 100 nm and 5 nm magnifications are shown in Figure 3.5. Images taken for the Pt/Graphene-PBI composite show the Pt nanoparticles are relatively uniformly deposited in comparison to the 40% Pt/Vulcan XC 72R JM and, especially, to the homemade Pt/Graphene. Pt/Graphene show cluster-like microstructures. The high resolution TEM images of Pt/Graphene- PBI suggests many of the particles are highly crystallized. The effective loading of Pt is considered a result of a coordination reaction between the Pt ions and PBI [120]. The mean diameter of Pt nanoparticles determined from TEM pictures was approximately 4.5 nm, 4.8 nm and 3.0 nm for 40% Pt/Vulcan XC 72R JM, Pt/Graphene and Pt/Graphene-PBI, respectively.

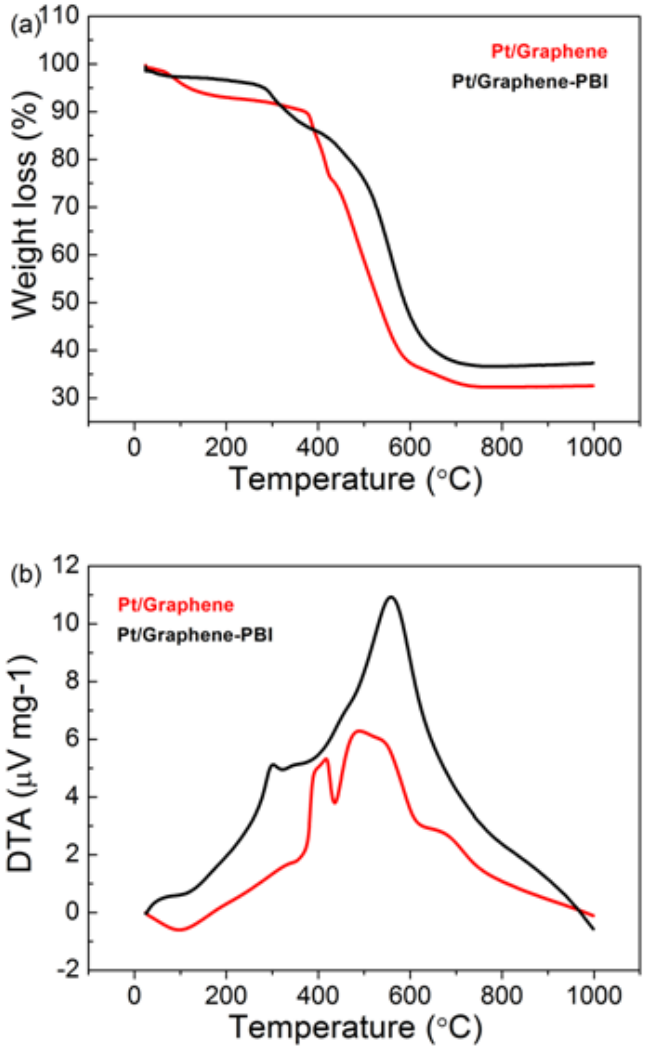

Figure 3.6: Analysis of Pt/Graphene (red line) and Pt/Graphene-PBI support (black line) TGA - a) and DTA - b).

TEM particle size results correlate with crystallite size obtained from the XRD analysis (Table 3.1). The combination of XRD and TEM results demonstrates that the PBI wrapping of Graphene induces an improved uniformity of Pt nanoparticles distribution as well as a reduction in size. Reducing of crystalline and particle sizes for the Pt/Graphene-PBI compared to Pt/Graphene could seem surprising whilst using the polyol method for synthesis of Pt nanoparticles, as the Pt particle size is formed before the Pt deposition onto support. However, as discusses previously metal nanoparticles tend to have difficulties to deposit on the non-functionalised graphene as there are not enough available active functional groups. Thus, once the attachment site is found, other particles will preferably gather to the same spot. This type of interaction leads to Pt nanoparticles sintering, re-combining and forming to a cluster-like structures; resulting in bigger final particle size than the initial, formed by polyol synthesis. In case of Pt/Graphene-BPI, PBI obviously gives enough active functional groups for the much even Pt nanoparticles attachment- distribution onto Grapnehe-PBI support.

TGA/DTA analysis for Pt/Graphene and Pt/Graphene-PBI were obtained in order to estimate the Pt loading (wt. %) on the supports. The TGA curve for Pt/Graphene-PBI showed a two-step weight loss reduction. The first step (at T = 300°C) was attributed to the oxidation of organic material (PBI). The second step (at T = 430°C) is characteristic of Graphene decomposition. The corresponding DTA (Figure 3.6, b)) curve exhibited a broad exothermic peak, centered at 600°C. An initial mass loss in conjunction with a broad endothermic peak is observed for the TGA and DTA curves respectively for Pt/Graphene in the temperature range 100-120°C. This likely corresponds to water desorption as previously discussed. In addition a broad peak is also observed within the DTA curve, characteristic of the Graphene decomposition. Pt nanoparticle loading is estimated to be 37 wt.% for Pt/Graphene-PBI and 32.5 wt.% for Pt supported on pristine Graphene.

The observed enhancement in Pt deposition efficiency (for the Pt/Graphene-PBI compare to the Pt/Graphene) together with increased homogeneity and reduced nanoparticle size is likely a result of Pt ion coordination on the PBI, as reported previously [120].

3.4 Electrochemical measurements

3.4.1 Preparation of the thin film electrodes for RDE study

To prepare the working electrode, thin catalytic film was deposited on a glassy carbon electrode surface. The preparation of the thin film electrode is shown in Figure 3.7. In steps 1) and 2), catalyst powder was mixed with de-ionized water and Nafion (5 wt. %). In steps 3)

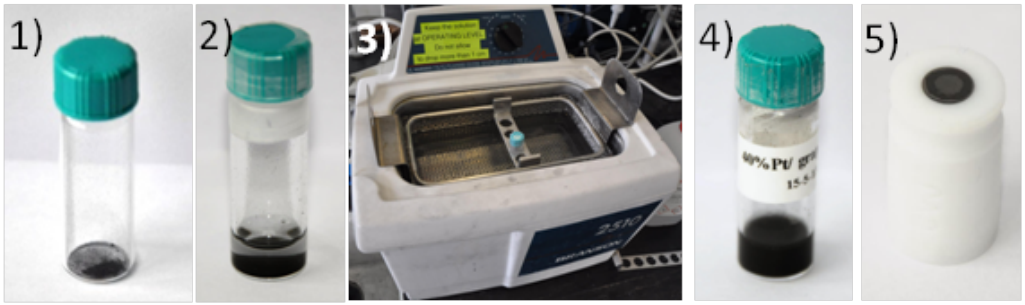

Figure 3.7: Preparation procedure of the thin film electrode

and 4), the mixture was sonicated for 30-60 min (Branson 2510), with sonication time varied for each catalyst.

After sonication (step 4), an aliquot of catalyst ink was pipetted onto the GC electrode which had been previously polished and cleaned. The GC electrode used in this study is 5 mm in diameter (0.196 cm^2 in surface) embedded in a Teflon cylinder (Radiometer analytical or home made). Prior to deposition the GC electrode was polished with Buehler Alpha Micropolish Alumina (1.0, 0.3 and 0.05 micron) before polishing using a Microcloth PSA 2-7/8" soaked with water. Polishing was performed until a mirror-like surface was obtained. Finally, the polished electrode was sonicated in de-ionized water for 15 min followed by sonication in alcohol and deionized water for a further 15 min to ensure a clean surface. The surface quality of each GC electrode was checked by optical microscope and, in case of contamination, the polishing and cleaning steps were repeated until a completely clean and smooth surface was achieved. Next, an aliquot of catalyst was pipetted onto the fine polished GC electrode (step 4) and dried under air or an N_2 atmosphere for 40 min. Obtained thin catalyst films (step 5) were checked using an optical microscope, with the electrode showing the greatest level of homogeneity being chosen for electrochemical measurements.

3.4.2 Choosing of the optimal ink composition

Pt loading was adjusted to achieve a thin film thickness of $\leq$ 0.2 µm on the surface of the glassy carbon electrode. This was achieved by loading 7-50 $\mu g_{Pt}/cm^2$ from an aliquot with a Pt:Vulcan carbon ratio of 10-50 wt.% Pt [32, 116, 125]. Thicker films may result in an increase in mass-transport resistance through the catalyst layer, due to incomplete access to the electrochemical area of the catalyst leading to incorrect data [116].

Different types of ink can be made and the composition of each must be optimized for each catalyst. For example, inherently hydrophobic catalysts may require inks with high alcohol (e.g., ethanol or isopropanol) to water ratios or only alcohol as well as a longer

sonication times in order to obtain optimal dispersion. In contrary, hydrophilic catalysts (such as state-of-the-art Pt/Vulcan catalysts) can be well dispersed in water mixed with 5 wt.% Nafion solution. The obtained ink solution is usually drop-casted onto the GC electrode in either one or two steps. Therefore, several methods were investigated in order to obtain the optimum catalyst ink which gave rise to homogeneous dispersion on the GC electrode. Each method is fully described in the following:

Non-alcohol ink dispersion methods

a) One step coating. This deposition method was used for the dispersion of the Pt on; Graphene, Graphene-PBI supports and 40% Pt on Vulcan Carbon from Johnson Matthey. 1 mg of catalyst was mixed with 30 µL of Nafion 5 wt.% and 700 µL of ultrapure water. The mixture was sonicated for 40 min before a 10µL drop was deposited onto the GC electrode (0,1963 cm^2) as described in previous section, yielding a Pt loading of 27,9 $\mu g_{Pt}/cm^2$.

b) Two steps coating. 1) Aqueous suspensions of 1 mg/mL were produced by ultrasonic dispersal of 1 mg of catalyst in pure water. A 10 µL aliquot of the ultrasonicated suspension was subsequently pipetted onto the GC electrode, yielding a Pt loading of 20,3 $\mu g_{Pt}/cm^2$ before being left to dry for approximately 40 min in a nitrogen atmosphere. 2) After evaporation of the water droplet, 20 µL of diluted Nafion (5 wt.% Aldrich) solution (1:100 suspension in water) was drop coated on top of the dried catalyst layer and left to dry for 20 mins more. Film thickness was estimated to be $\sim$0.2 µm [126].

Alcohol ink dispersion methods

c) One step coating. 5 mg of catalyst was dispersed in a mixture of 50 µL of Nafion 5 wt.% and 1 mL of ethanol (Sigma-Aldrich, $\geq$ 95,5 %, CAS number 64-17-5) by sonication. 4,2 μL of the obtained ink was drop coated on the GC electrode yielding a Pt loading of 40,75 $\mu g_{Pt}/cm^2$ for a catalyst with 40% content of Pt.

d) Two step coating. 1,2 mg of 40% Pt catalyst was mixed with 800 µL ultrapure water, 200 µL of isopropanol and 20 µL of Nafion 5 wt.%, then ultrasonicated for 45 min. 10 µL was used in a two step procedure; 5 µL was first drop-casted and dried and other 5 µL was then drop-casted, yielding a loading of 23,97 $\mu g_{Pt}/cm^2$ [127].

As an example, Figure 3.8 shows the difference for results obtained between methods a) and d) for the Pt/Graphene-PBI catalyst. Non-alcohol method a) was apparently more effective at dispersing the Pt than method d) (i.e. where isopropanol and water were used

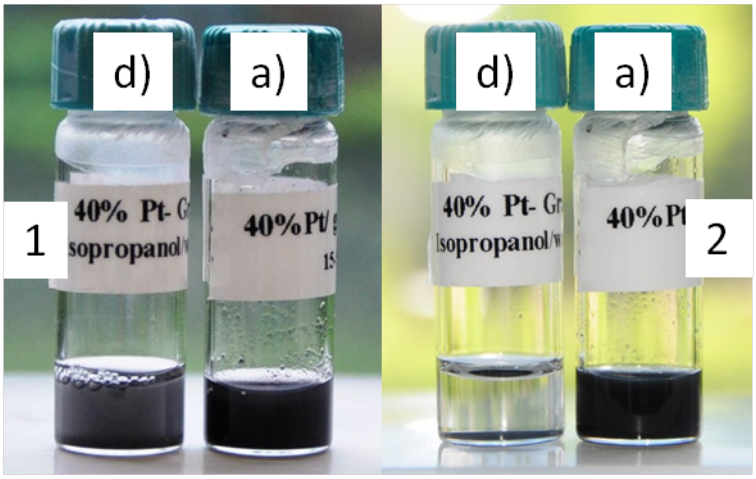

Figure 3.8: Example of applying different methods for the catalyst dispersion. Pt/Graphene-PBI catalyst dispersed by methods a) and d). Ink dispertion after 40 min of sonication - 1) and, then, after 24 hours left untouched - 2).

to disperse the catalyst). Figure 3.8 - 1) shows samples after 40 min of sonication, from which it can be seen that method a) provided superior dispersion in comparison to method d). Afterwards, samples were left untouched for 24 hours. Figure 3.8 - 2) shows these results, where it is clear method a) remains a relatively good dispersant in comparison to method d), where almost all nanoparticles became detached.

Several other types of the ink dispersion exist, including variations of those employed in this study which may be able to achieve the desired result. Furthermore, different dispersion agents could also be employed, e.g. PVP and Novec FC-4434. However, optimization of concentration is necessary to be able to negate adverse mass transport limitations.

3.4.3 Activity of Pt/Graphene-PBI for oxygen reduction

In the following section the Graphene-PBI supported Pt nanoparticle catalyst was assessed in regards to the ORR to compare its activity with a home made Graphene supported Pt and a benchmark commercial Vulcan XC 72R supported Pt nanoparticle catalyst. Figure 3.10 shows ORR measurements made in 0.1 M $HClO_4$ at room temperature. In figure 3.10 a) typical polarization curves are shown obtained by rotating disk electrode (RDE) for Pt/Graphene-PBI at various rotation speeds in oxygenated 0.1 M $HClO_4$ at room temperature. All polarization curves exhibit a plateau behaviour between 0.06 - 0.60 V vs. RHE, indicating a diffusion controlled regime. Current density increases with increasing rotation speed. Thus, oxygen diffusion to the catalytic reaction center must be the rate limiting process therefore the process is highly dependent on rotation rate. The diffusion controlled

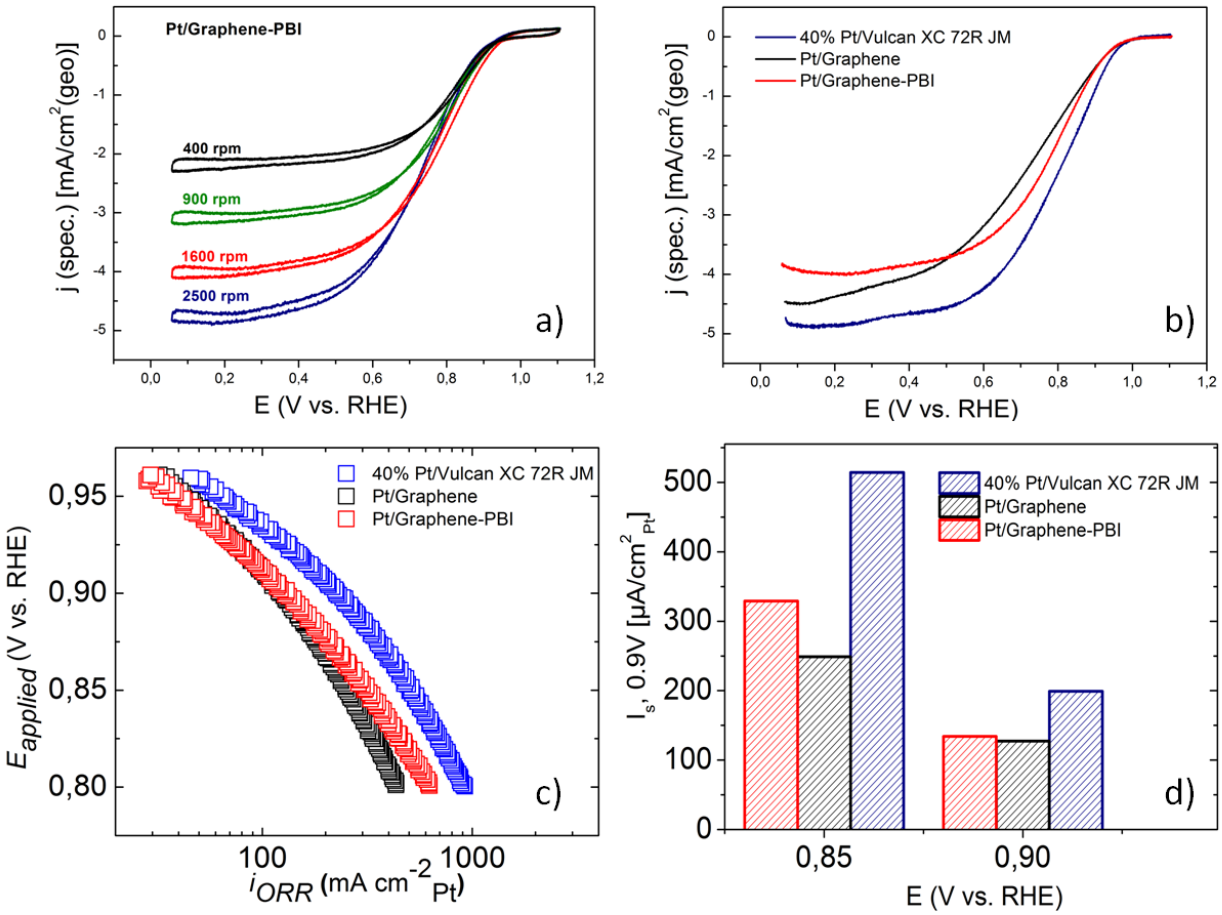

Figure 3.9: Oxygen reduction reaction (ORR) data analysis for Pt/Graphene-PBI, Pt/Graphene and 40% Pt/Vuclan XC 72R catalysts: a) Typical polarisation curves for Pt/Graphene-PBI at various rotating speeds, b) Background corrected polarisation curves for Pt/Graphene-PBI, Pt/Graphene and 40% Pt/Vuclan XC 72R normalazed to geometric surface area, c) Tafel plots for Pt/Graphene-PBI, Pt/Graphene and 40%Pt/Vuclan XC 72R, normalized to Pt ECSA, background and mass transport corrected, d) ORR Pt specific surface activity compared at 0.9 and 0.85 V vs. RHE for Pt/Graphene-PBI, Pt/Graphene and 40% Pt/Vuclan XC 72R catalysts. All mesurments were done in 0.1 M $HClO_4$ at room temperature.

regime does however appear to become a diffusion - kinetic controlled reaction at voltages higher than 0.6 V vs. RHE. Past 0.9 V vs. RHE, the voltammetric profile appears largely kinetically controlled, as sweeps become independent of rotation rate. Finally, the electrocatalytic conversion of oxygen drops to zero at the open circuit potential around 1.1 V vs. RHE.

Figure 3.9 b) shows the background corrected ORR curves collected at 1600 rpm for Pt/Graphene-PBI, Pt/Graphene and 40% Pt/Vuclan XC 72R catalysts normalized to geometric surface area. Figure 3.9 c) presents Tafel Plots for Pt/Graphene-PBI, Pt/Graphene and 40% Vuclan XC 72R, normalized to Pt ECSA. Figure 3.9 d) provides an overview of ORR

Pt specific surface activity at 0.9 and 0.85 V vs. RHE for Pt/Graphene-PBI, Pt/Graphene and 40% Pt/Vuclan XC 72R catalysts. Figure 3.9 c) and d) show the background and mass transport corrected intrinsic activity, j_k. For these figures measured ORR current density, j, was corrected for mass transport according to:

$$\frac{1}{j} = \frac{1}{j_k} + \frac{1}{j_d} \tag{3.2}$$

where j_d is the diffusion limited ORR current density obtained at a given rotation rate.

A summary is given in Table 3.1 reporting; platinum mass and surface area specific based activities, ECSA and particle and crystallite size of nanoparticles obtained from TEM and XRD, respectively.

The Pt/Graphene-PBI catalyst exhibited a more positive onset potential inferring a higher ORR catalytic activity than observed for the Pt/Graphene catalyst particularly at 0.85 V vs. RHE. At 0.9 V vs. RHE the difference is less pronounced, however still remains higher for Pt/Graphene-PBI. The data for the 40% Pt/Vuclan XC 72R commercial catalyst is in agreement with reported Pt activities and the ECSA of commercial platinum catalysts supported on conventional Vulcan XC 72R [63]. The results obtained from the home made Pt/Graphene and Pt/Graphene-PBI are comparable with those of the 40% Pt/Vuclan XC 72R.

With regards to Pt electrochemical surface area (ECSA), Pt/Graphene-PBI exhibits higher ECSA values than Pt/Graphene (Table 3.1). This enhancement of Pt/Graphene-PBI Pt surface specific activity and ECSA is likely a result of the advantages inherent in the Graphene-PBI support in comparison to an untreated Graphene support.

From the XRD and TEM studies it was shown that by applying PBI onto Graphene, Pt nanoparticles size reduced significantly in size compare to observed for Pt catalyst with a plain graphene as a support. The introduction of a PBI coating aided more even Pt deposition on the surface as is clearly seen from TEM images. In addition, Pt (wt.%) loading on the support enhanced from 32.5 wt.% to 37 wt.% when applying BPI wrapping as revealed by TGA results. Thus, our study suggests these factors can enhance the catalytic activity of the composite catalyst and ECSA.

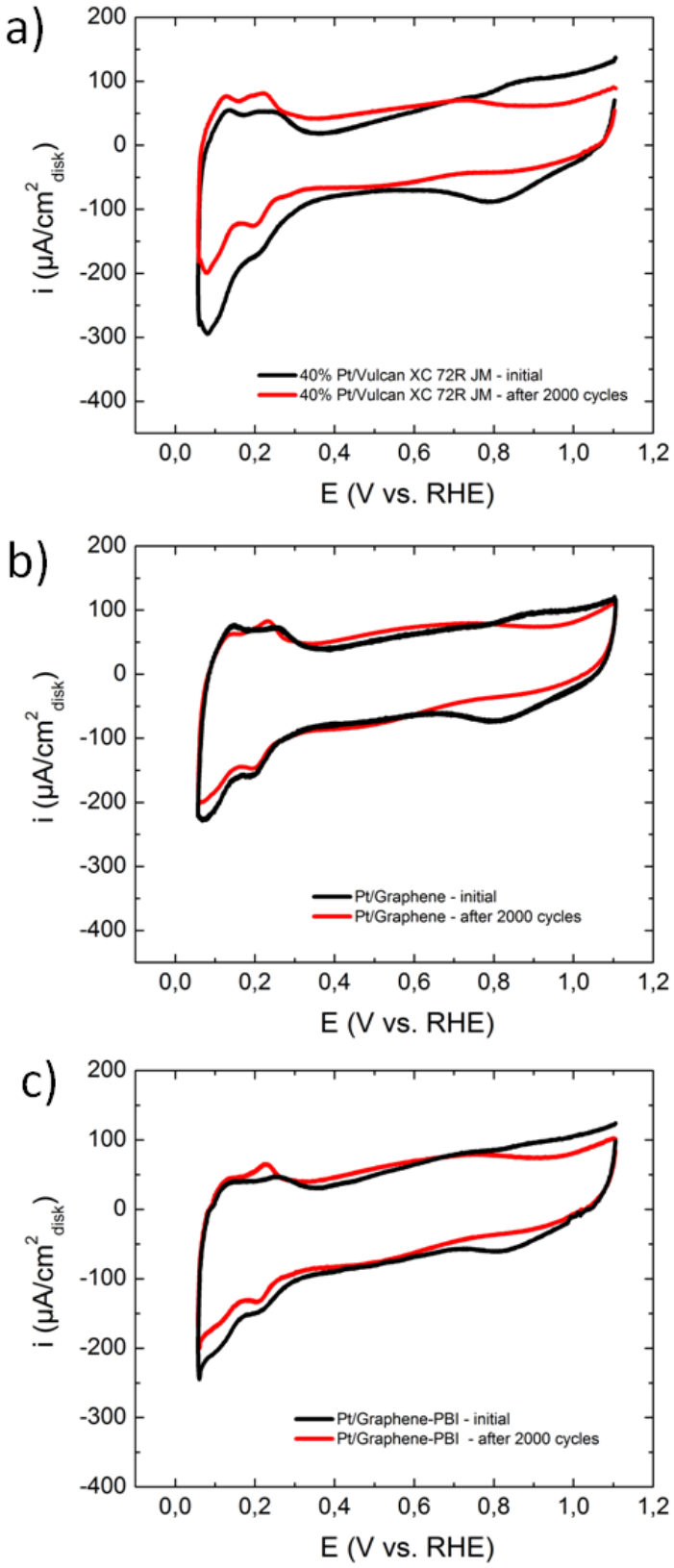

Figure 3.10: Cyclic voltammograms (CVs) of the catalysts for evaluation of the platinum electrochemical surface area (ECSA), black line states the initial CVs and red line represents CVs after voltage cycling between 0.06 and 1.1 V vs. RHE in deaerated 0.1 M $HClO_4$ with a scan rate of 10 mV/s at room temperature, geometric area normalized: a) 40% Pt/Vuclan XC 72R, b) Pt/Graphene, c) Pt/Graphene-PBI.

3.4.4 Stability of the Pt/Graphene-PBI during the voltage cycling

To evaluate whether a PBI coating will also improve an ECSA stability characteristics of the synthesized catalyst, a voltage cycling long-term stability test was performed for 40% Pt/Vuclan XC 72R, Pt/Graphene and Pt/Graphene-PBI. Catalysts were exposed to 2000 voltage cycles between 0.06 - 1.1 V vs. RHE with a scan rate 10 mV/s in oxygen free 0.1 M $HClO_4$ at room temperature. Figure 3.10 shows results of cyclic voltammograms (CVs) for evaluation of catalysts (normalized to geometric disk area). The black line represents the initial CVs whilst the red line represents CVs after 2000 voltage cycles. Table 3.1 summarizes obtained ECSA data normalized to the area and mass of platinum before and after CV cycling.

The ECSA of the commercial 40% Pt/Vuclan XC 72R catalyst is higher than for the Pt/Graphene and Pt/Graphene-PBI catalysts, however the 40% Pt/Vuclan XC 72R exhibited a significant drop of ECSA after potential cycling compare to others. ECSA for the Pt/Graphene-PBI nanoparticle catalyst is higher than for Pt/Graphene and much higher than for 40% Pt/Vuclan XC 72R after voltage cycling testing. Pt/Graphene ECSA is a little lower than its initial level, while Pt/Graphene-PBI ECSA remained practically unchanged. The change in ECSA observed for the Pt/Graphene-PBI catalyst could possibly be explained by the following factors; The thin shell of PBI offers additional protection, reducing graphene corrosion without sacrificing the electrical conductivity of the existing graphene support. The Pt nanoparticles are strongly incorporated into the PBI structure preventing it detachment, sintering, migration and/or dissolution - these hypothesis require further investigations, e.g. in-situ TEM and ICP analysis. Thus, the data derived from this study highlights the potential to enhance ECSA properties by employing a PBI coated Graphene support as opposed to non coated Graphene. The study also shows the PBI coated catalyst is more active in regards to the ORR than Pt/Graphene alone and significantly more durable to both Pt/Graphene and commercial 40% Pt/Vuclan XC 72R.

3.5 Conclusions

In this chapter a PBI wrapped Graphene supported platinum catalyst was synthesized. The electrocatalytic reduction of oxygen activity in addition to cycling stability were compared for Pt/Graphene-PBI, Pt/Graphene and commercial 40% Pt/Vulcan XC 72R electrocatalysts.

From the above experiments the following can be concluded:

• The Pt/Graphene-PBI catalyst exhibited a more positive onset potential, hence showed a higher ORR catalytic activity than for the Pt/Graphene catalyst at 0.85 V vs. RHE

Table 3.1: Summary of Pt/Graphene-PBI, Pt/Graphene and 40%Pt/Vulcan XC 72R JM performance after 2000 cyles between 0.06 to 1.1 V vs. RHE in deaerated 0.1 M $HClO_4$ with a scan rate 10 mV/s at room temperature

Catalyst	Pt loading$_{(TGA)}$ [wt.%]	Pt particle size $_{(TEM)}$ [nm]	Pt crystallite size$_{(XRD)}$ [nm]	ORR		ECSA [m^2/g_{Pt}]		ECSA [cm^2_{Pt}]	
				I_s, 0.9V [$\mu A/cm^2_{Pt}$]	I_s, 0.9V [A/mg_{Pt}]	Initial	after 2000 cycles	Initial	after 2000 cycles
40%Pt/Vulcan XC 72R JM	-	4.9	4.5	199.15	0.07	24.80	13.21	0.9402	0.7238
Pt/Graphene	32.5	5	4.8	127.33	0.05	18.51	18.98	0.9378	0.9614
Pt/Graphene-PBI	37	2.7	3.0	134.2	0.03	21.65	23.67	1.0969	1.0177

• The ORR results for the home made Pt/Graphene and Pt/Graphene-PBI are comparable with the 40% Pt/Vuclan XC 72R and with the benchmark commercial fuel cell catalysts

• Pt/Graphene-PBI exhibits a higher initial ECSA value than Pt/Graphene

• XRD and TEM studies confirm that the application of PBI onto Graphene alters the platinum nanoparticle size dramatically decrease than those observed for the plain Pt graphene catalyst as a support

• Introduction of PBI coating aided a more even Pt deposition on the surface which was proven by attained TEM images

• Pt (wt.%) loading on the support enhanced from 32.5 wt.% to 37 wt.% when BPI wrapping was employed as revealed by TGA results

• ECSA of the 40% Pt/Vuclan XC 72R commercial catalyst was higher prior to potential cycling than for Pt/Graphene and Pt/Graphene-PBI catalysts, however 40% Pt/Vuclan XC 72R exhibited a significant drop in ECSA after 2000 cycles in comparison to the other catalysts studied

• The ECSA for the Pt/Graphene-PBI nanoparticle catalyst was greater than that of either Pt/Graphene or 40% Pt/Vuclan XC 72R after potencial cycling testing. ECSA of Pt/Graphene-PBI is remained unchaned, while Pt/Graphene ECSA decreased

The observed ORR activity and ECSA properties for the Pt/Graphene-PBI catalyst can potentially be explained by the following factors. The thin shell of PBI offers additional protection to the conditions employed and reduces graphene corrosion without sacrificing electrical conductivity of the existing graphene support. The increase in ORR could be explained by a change in Pt nanoparticle size, whereby PBI induces improved nucliation of Pt nanoparticles onto the inert graphene surfaces, subsequently aiding Pt nanopartcle distribution and preventing damage of the support. Thus, data derived from the current study highlights the potential enhancements of a PBI coated Graphene support in comparison to non coated Graphene. PBI addition makes the catalyst more active in regards to ORR than a simpler Pt/Graphene catalyst and bestows a greater degree of durability in comparison to either Pt/Graphene or a commercial 40% Pt/Vuclan XC 72R catalyst. Thus, it is concluded that Graphene-PBI supports are viable fuel cell catalyst supports.

Chapter 4

Bulk Pt-Si alloys as highly active methanol and CO electro-oxidation catalysts

4.1 Introduction

This chapter reports on the synthesis and characterisation of bulk Pt-Si alloys as catalyst for the electro-oxidation of CO and methanol. Pt is usually employed for these reactions and is widely recognized as the most active catalyst for CO and methanol electro-oxidation. However, during the reaction the Pt catalyst suffers from rapid deactivation caused by carbon monoxide poisoning, thus kinetics decrease leading to unacceptably high anodic overpotentials [128]. This reaction involves a bifunctional mechanism requiring a CO tolerant catalyst or catalysts with inherently higher activity toward adsorption of both CO and water oxidation sites [47, 51, 129–131]. The alloy of platinum with transition metals (Pt-M, where M=Ru, Sn, Rh, etc.) [129] is the most common way to satisfy this requirement. In this chapter the bifunctional mechanism will only be explained briefly. For a more detailed explanation the reader is directed to the introduction of this thesis. Pt-M catalysts such as Pt-Ru [39,47,52,128,129,132] and Pt-Sn [53,54,131] have been proven to enhance catalytic activity towards CO oxidation at relatively low potentials in comparison to that of pure Pt. This phenomenon has been attributed to the formation of hydrated oxides on the alloying transition metal, facilitating oxidation of CO and providing free surface sites for the oxidation of hydrogen [133]. Nevertheless, even a well-alloyed Pt-M catalyst will suffer from base-metal leaching under the acidic operating conditions of a fuel cell [134]. Therefore, this chapter explores the prospect of alloying Pt with other non-metal elements such as silicon,

which is relatively insoluble in most of acids. Previously it has been shown that silicone nanocones [135], SiO_2 nanoparticles [136] and porous silicone [137] (i.e. used as a support for Pt based catalysts [135]) exhibit greater tolerance towards CO poisoning [136, 137]. It has been assumed they follow the bifunctional mechanism of the reaction. However, no direct electrochemical study on Pt-Si alloys has currently been conducted. The work reported in this chapter describes studies conducted using Pt-Si bulk alloys as potential small organic molecular electro-oxidation catalysts. Consequently silicon is suggested to provide a binding site for water adsorption (as a highly oxophillic element), whilst Pt serve as a CO adsorption site.

4.2 Synthesis of bulk Pt-Si alloys

According to the phase diagram (Figure 4.1), more than ten stoichiometric Pt-Si compounds are known with compositions ranging from PtSi as the most silicon rich to Pt25Si7 as the most silicon deficient. In order to study the properties and catalytic behavior of different compositions, Pt:Si catalysts with the following atomic ratios were prepared ; “Pt0.5Si0.5”, “Pt0.8Si0.2” and “Pt0.97Si0.03” . These preparations are marked as ”red”, ”yellow” and ”green” lines on the phase diagram, respectively.

Platinum-silicon alloys were produced following the preparation scheme shown in Figure 4.2. Firstly, high purity Pt foil (0.03 mm, 99.99 mass %, Dansk Aedelmetal A/S) and high purity Si powder (Max. particle size: 45 micron, 99.998 mass %, GoodFellow) were pressed into a pellet of 2 grams total mass in a glove box under an argon atmosphere. Next, the obtained Pt-Si pellet was transferred in preparation for arc-melting using an Edmund Bühler 2414 furnace (Figure 4.3). The arc-melting process was conducted under an argon atmosphere employing at least 10 melt cycles for each sample. Subsequently the produced platinum cilicides (Pt-Si alloys) were prepared for further treatment and characterisation.

4.3 Structural characterization of Pt-Si alloys

4.3.1 Bulk structural characterisation

Bulk structural composition of Pt-Si alloys was confirmed by X-ray Diffraction (XRD) (Figure 4.4). XRD measurements were performed using a Bruker D8 diffractometer using a large area GADDS 2-dimensional detector. The samples were spun in Debye diffraction rings to increase the amount of scattered X-rays observed and increase the number of crystallites

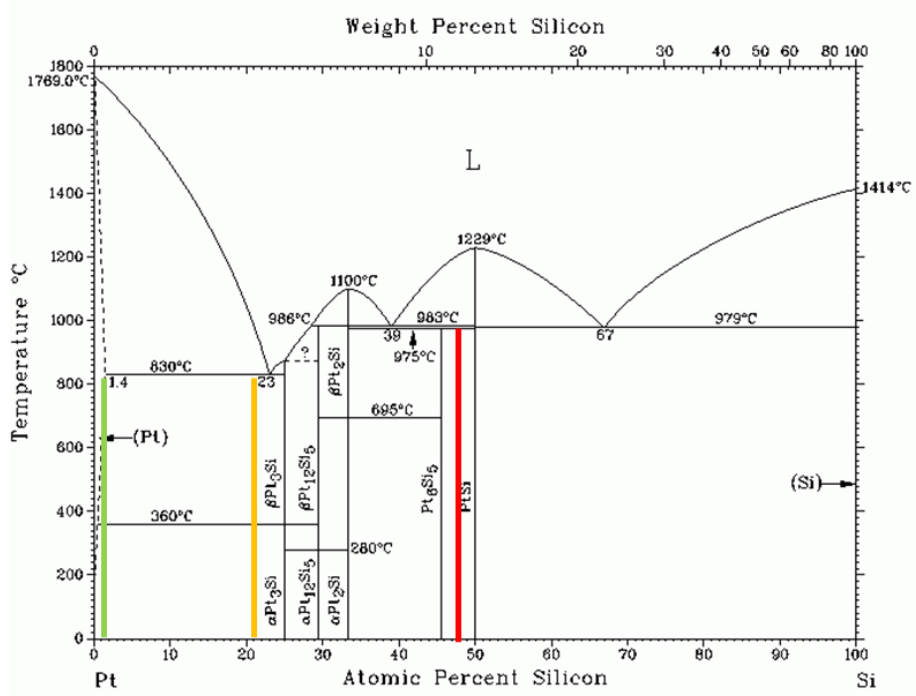

Figure 4.1: "Platinum – Silicon" phase diagram used for choosing the atomic ratios for Pt:Si catalysts [6]. "Red", "yellow" and "green" lines at the phase diagram corresponding to "Pt0.5Si0.5", "Pt0.8Si0.2" and "Pt0.97Si0.03" atomic ratios, respectively.

contributing to the measured pattern. Data was collected using Copper Kα radiation and the 15-75° window in the 2θ range. For the pristine Pt-Si alloy with the overall composition "Pt0.5Si0.5", a Pt6Si5 phase as well as a Pt12Si5 phase could be identified (Figure 4.4 (a)). "Pt0.8Si0.2" contained a Pt3Si phase and additionally a Pt-rich phase (marked as Pt0.985Si0.015) which is essentially Pt doped with Si. The "Pt0.97Si0.03" alloy also exhibited evidence of a Pt3Si phase manifest as a (002) Pt3Si peak in addition to dominant Pt-rich phase peaks.

To refine the structure (by inducing a greater level of homogeneity in order to verify presence of the Pt3Si phase) annealing was performed at temperatures up to 847$\pm$2°C for 16 hours under 4 % H_2/Ar atmosphere for both "Pt0.8Si0.2" and "Pt0.97Si0.03" alloys. After annealing, clear evidence of a Pt3Si phase was observed in both alloys. A comparison of pristine and annealed "Pt0.8Si0.2" and "Pt0.97Si0.03" alloys is shown in Figure 4.4 (b) and (c) respectively, where Pt3Si peaks became stronger and sharper while the Pt-rich phase is still remains.

Bulk compositions was also verified by energy dispersive spectroscopy (EDS) analysis (Figure 4.5). The Oxford Instrument INCA EDS equipped on JEOL 6320FV Field-Emission High-resolution SEM was used to determine the bulk Si concentration of generated Pt-Si

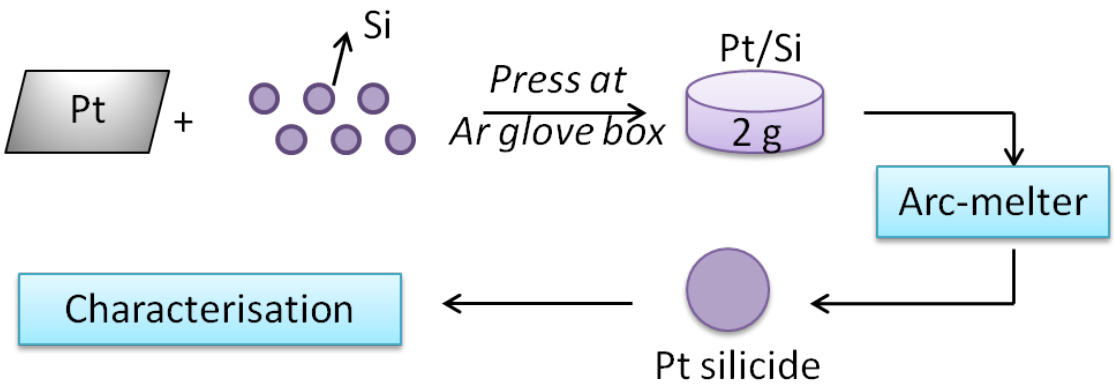

Figure 4.2: Preparation scheme for the platinum silicides (or Pt-Si alloys).

alloys. Spectra were collected up to 10 keV for 10 min. Overall results were determined as the average of three different spots on the sample. Pt M and Si K peaks were used to calculate the atomic ratio of platinum and silicon, which after arc-melting, were found to be similar to the ratio of the starting materials. Overall bulk analyses showed reasonable agreement with theoretical values, although Pt content was slightly lower than predicted. This suggests a small loss of Pt during the preparation procedure.

Figure 4.3: Arc-melter Edmund Bühler 2414. Department of Energy Conversion and Storage, DTU

4.3.2 Surface atomic structural characterisation

Surface atomic structure characterisation of Pt-Si alloys was performed using X-ray photoelectron spectroscopy (XPS).

A Physical Electronics Versaprobe II X-ray Photoelectron Spectrometer was used to study surface chemistry of Pt-Si samples. First Pt-Si electrodes were exposed to a vacuum for 24 hours prior each measurement; afterwards samples were fixed onto the Al sample holder with conductive tape for XPS. X-ray photoelectron spectra were subsequently collected in ultra-high vacuum, less than 1 $\times$ 10-8 Torr. First, a survey spectrum from 0 to 1100 eV at steps of 0.8 eV was taken. Then, high resolution spectra at steps of 0.1 eV were recorded in the range of Pt (4f), Si (2s), and C (ls) bands. In addition the C (1s) band was collected to correct for potential energy shift brought about by charge accumulation. Photoelectron spectra were evaluated using Gaussian fits after corrections were applied. The comparison between Pt and Si peaks provides surface Si atomic concentrations, with corrected relative sensitivity factors (RSF) of 51.064 and 2.583 for Pt (4f) and Si (2s) respectively.

As shown in Figure 4.6, Pt (4f) and Si (2s), band spectra were recorded. The peak position for Pt 4f7/2 appeared to be around 70.9 eV, which is the value of pure Pt rather than of Pt-Si compounds [138]. This indicates that on the surface, Pt-Si mainly exists in a form of a solid solution, which is different from the bulk structure characterized by XRD measurements. The XPS results implied that Pt-Si compounds might be unstable on the surface. Evaluation of the photoelectron spectra using Gaussian fits after corrections and comparison between Pt and Si peaks provided surface Si atomic concentrations with corrected relative sensitivity factors (RSF) of 51.064 and 2.583 for Pt (4f) and Si (2s), respectively. Results show that for pristine “Pt0.5Si0.5”, “Pt0.8Si0.2” and “Pt0.97Si0.03” alloys, surface Si concentrations were 57%, 24% and 14%, respectively. This value is a little higher than the bulk Si concentration determined by EDS (Figure 4.5), but still within a reasonable error range (i.e. within the limitation of EDS and XPS techniques).

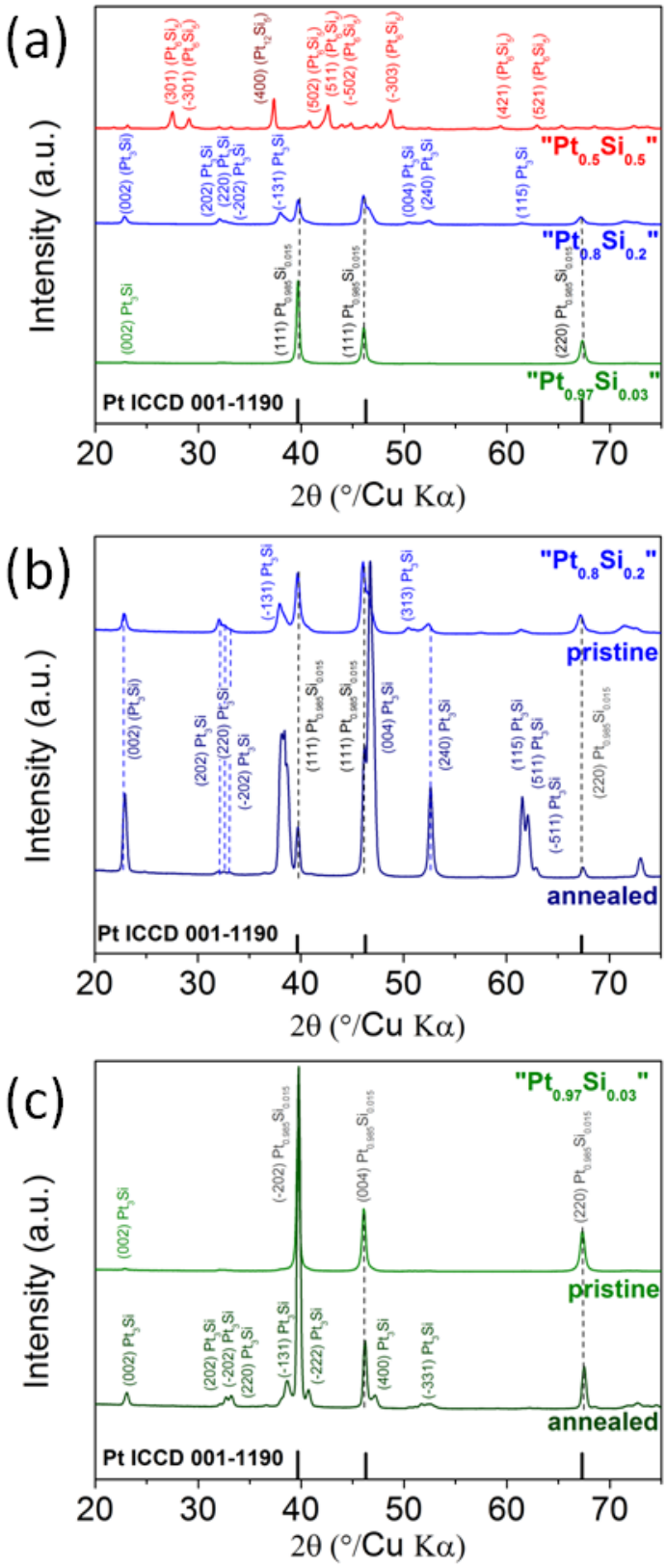

Figure 4.4: (a) XRD patterns of pristine Pt-Si alloys with the overall Pt-Si compositions "Pt0.5Si0.5", "Pt0.8Si0.2" and "Pt0.97Si0.03". (b) and (c) XRD patterns of pristine vs. annealed Pt-Si alloys with the compositions of "Pt0.8Si0.2" and "Pt0.97Si0.03", respectively (annealed at T = 847 ± 2°C for 16 hours under 4% H_2/Ar atmosphere). Individual peaks are identified on the figure.

Element	Atomic %
Si K	53
Pt M	47

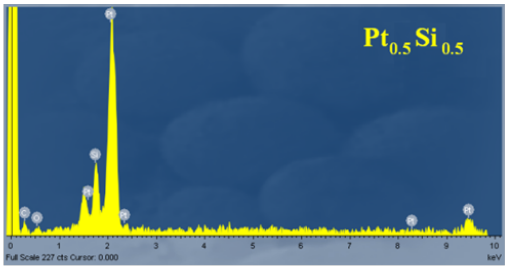

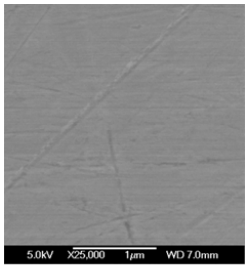

Element	Atomic %
Si K	22
Pt M	78

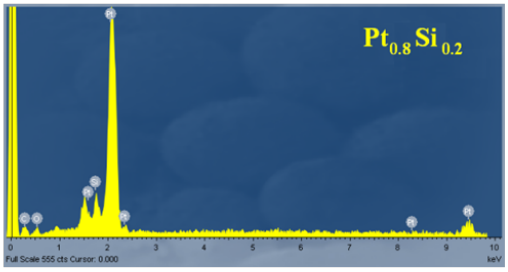

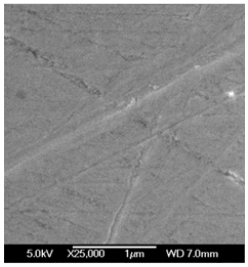

Element	Atomic %
Si K	6
Pt M	94

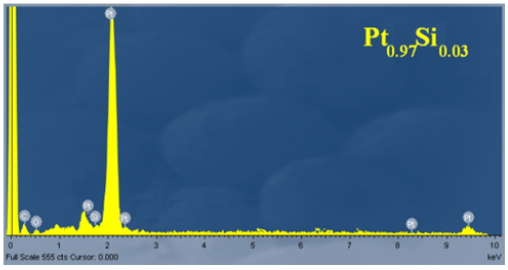

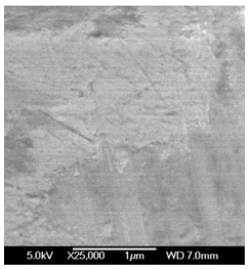

Figure 4.5: Bulk elemental compositions of pristine Pt-Si alloys, evaluated from EDS data by the relative intensities of Pt M and Si K peaks. The Si compositions are slightly higher than nominal values, which can be explained by Pt loss during sample preparation process. The relative SEM images are shown on the right.

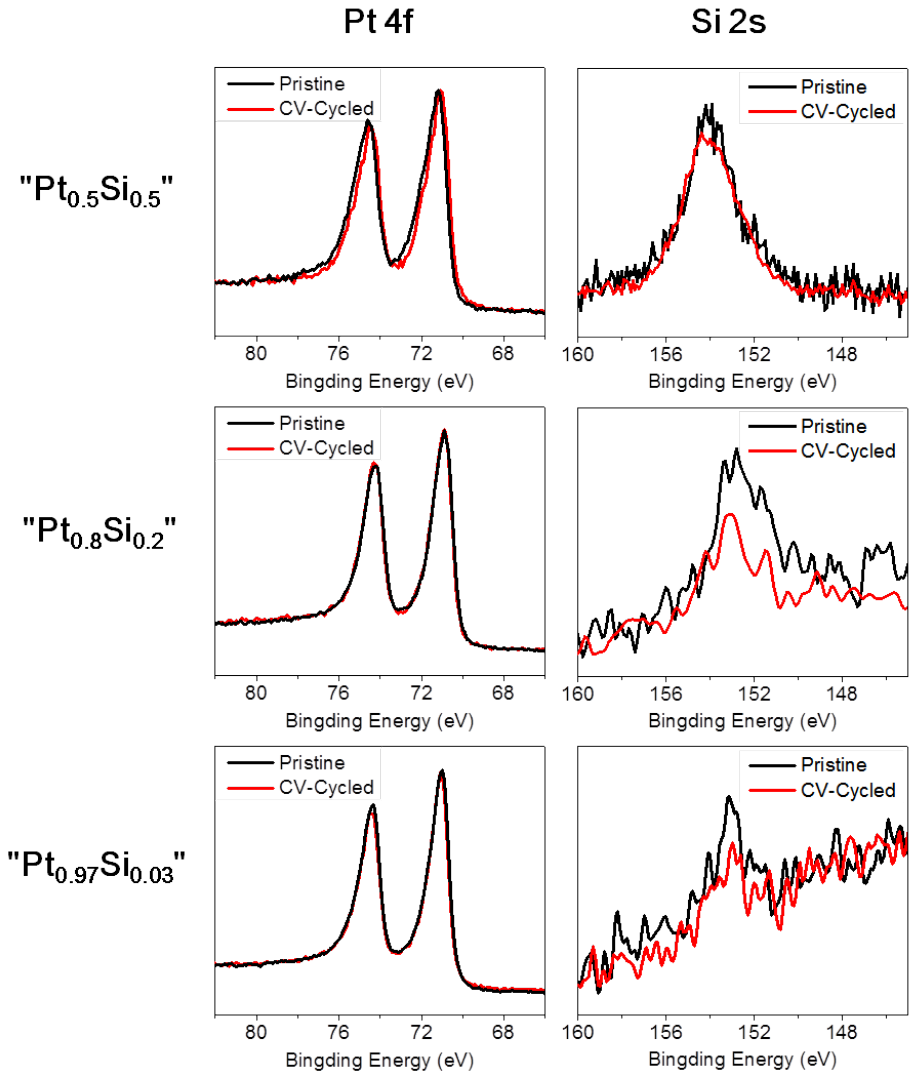

Figure 4.6: XPS results on pristine and CV-cycled pristine Pt-Si alloys.

4.4 Electrochemical characterisation of Pt-Si alloy surfaces

4.4.1 Sample preparation

Due to the non-standard shapes of obtained Pt-Si alloys, a new ring disc electrode (RDE) holder was designed. A schematic of the specifically designed sample holder is presented in Figure 4.7 (a). To fit the non-standard samples into the newly designed RDE holder, alloys were inserted into epoxy resin (OMEGABOND®, OB-101-1/2), dried for 24 hours, polished using alumina polishing sheets (3 μm, 1 μm, 0.2 μm, Thorlabs) and finalized by alumina paste (0.05 μm alumina particle suspension, micropolish, Buehler). This methodology al-

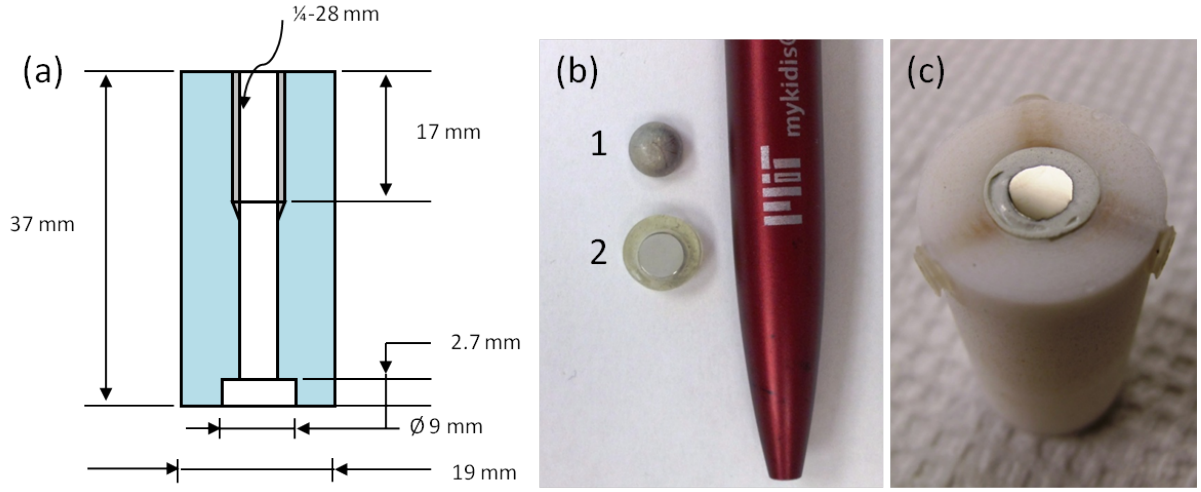

Figure 4.7: (a) Scheme of specifically designed sample holder for bulk Pt-Si alloys, (b) 1 - typical bulk Pt-Si sample obtained after arc-melting, (b) 2 - mirror-like polished bulk Pt-Si alloy sample inserted in epoxy resin, (c) Prepared sample inserted into the specifically designed sample holder

lowed a mirror-like disk surface to be obtained prior to each electrochemical measurement. The typical bulk Pt-Si sample obtained after arc-melting is presented in Figure 4.7 (b) 1, complete with mirror-like, polished bulk Pt-Si alloy sample inserted in epoxy resin (Figure 4.7 (b) 2). Afterwards, the sample was inserted into the specially designed sample holder as shown in Figure 4.7 (c) and fixed into the rotating disk electrode (RDE) motor (PINE Instruments, USA) for further electrochemical measurements.

4.4.2 Set-up and procedure for electrochemical measurements

A three-electrode cell was used for all electrochemical measurements at room temperature. A Pt wire and saturated calomel electrode (SCE) (Analytical Sensor, Inc.) were used as the counter and reference electrodes, respectively. The SCE potential was calibrated to the RHE scale. Cyclic voltammetry measurements were performed to electrochemically clean and stabilize Pt-Si sample surfaces in O_2-free 0.1 M $HClO_4$ electrolyte saturated for 30-min by ultra-high-purity Ar gas (99.999%, Airgas). The Pt-Si electrodes were cycled between 0.05 and 1.2 V (vs. RHE) at a scan rate of 200 mV/s for 150 cycles to reach steady state. Subsequently following ECSA, CO oxidation and methanol electro-oxidation measurements were performed on the surface-stabilized electrodes. A slower CV scan at 10 mV/s with a voltage range between 0.05 and 1.1 V (vs. RHE) was used to calculate the ECSA from the charge integration of hydrogen adsorption and desorption areas between 0.05 and 0.35 V (vs. RHE). A conversion factor of 210 $\mu C/cm^2$ Pt was applied after double-layer correction. The CO stripping measurements were performed between 0.05 and 1.1 V (vs. RHE) with a

scan rate of 5 mV/s in 0.1 M $HClO_4$ O_2-free and CO-free electrolyte, obtained by bubbling ultra-high-purity Ar gas (99.999%, Airgas) for at least 30 min, after the complete adsorption of CO at a potential of 0.1 V (vs. RHE). The methanol electro-oxidation activities were measured between 0.05 and 1.1 V (vs. RHE) at 50 mV/s in O_2-free 0.1 M $HClO_4$ and 1 M CH_3OH electrolyte prepared by 30-min bubbling of ultra-high-purity Ar gas (99.999%, Airgas). All activity measurements were background-corrected by subtracting the blank CV curves obtained in 0.1 M $HClO_4$ O_2-free electrolyte at the corresponding scan rates, normalized by Pt ECSA.

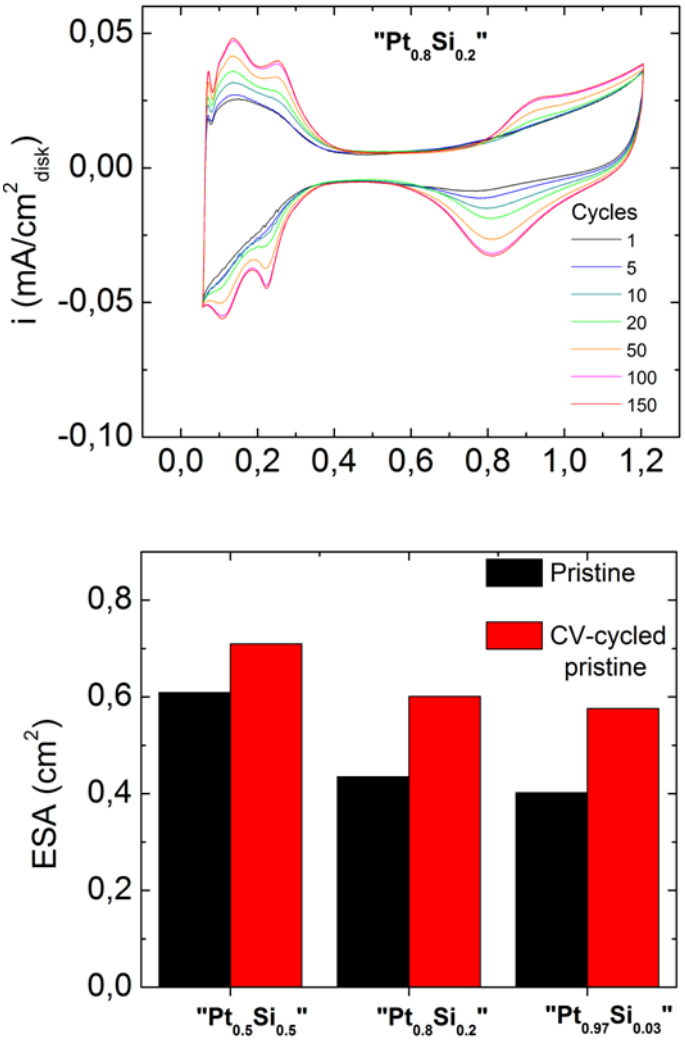

Figure 4.8: Stabilization effects on Pt-Si alloys. (a) Example of hydrogen adsorption (HAD) curves for pristine "Pt0.8Si0.2" alloy in 0.1 M $HClO_4$ at 10 mV/s. (b) Comparison of the ECSA for pristine Pt-Si alloys at different at.% compositions before (black) and after (red) CV-cycling, calculated from HAD curves.

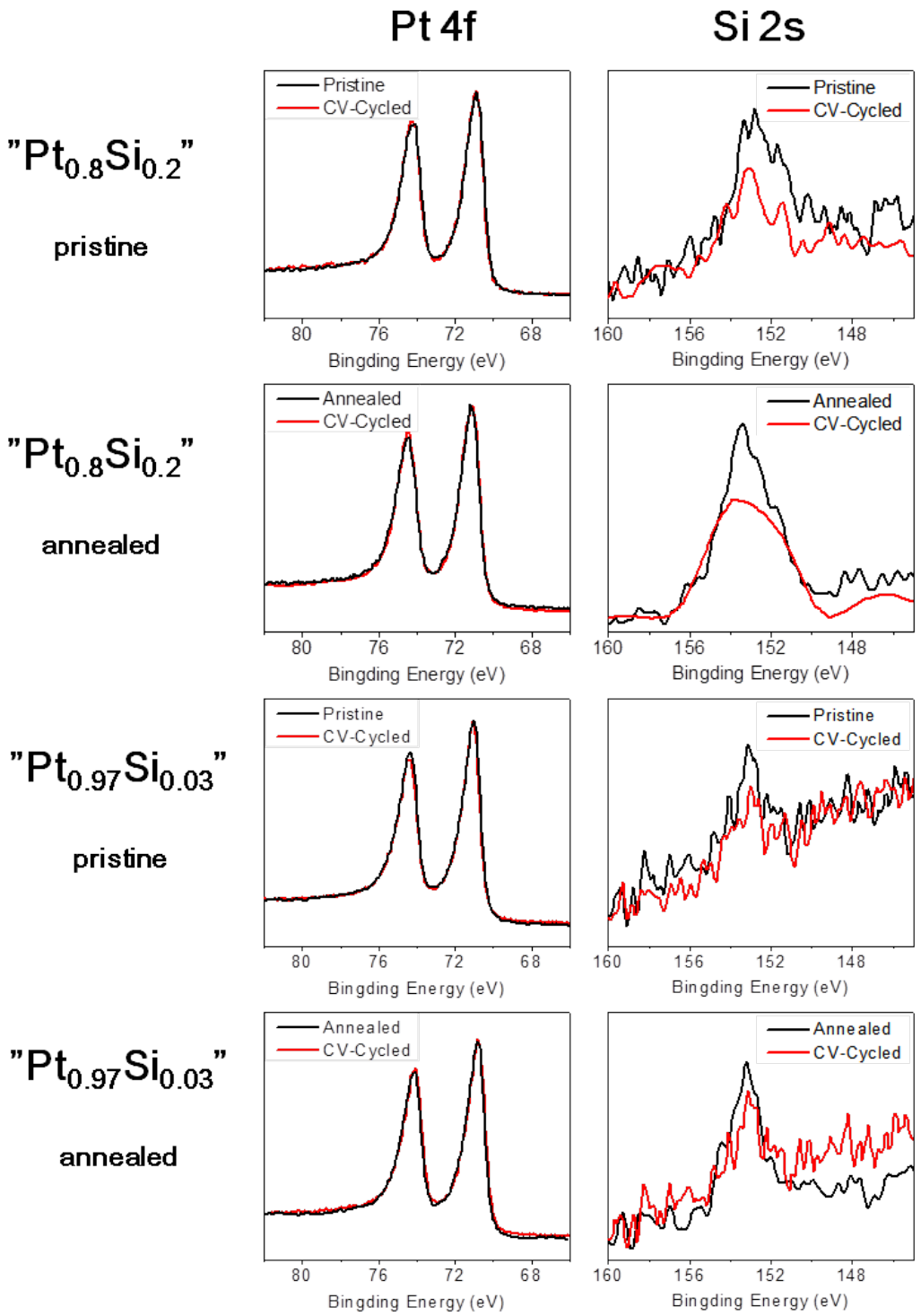

Figure 4.9: XPS results on pristine and annealed Pt-Si alloys, both before and after CV cycling. By comparing the relative intensity of Pt and Si peaks, the leaching of Si during CV cycling can be observed on all samples.

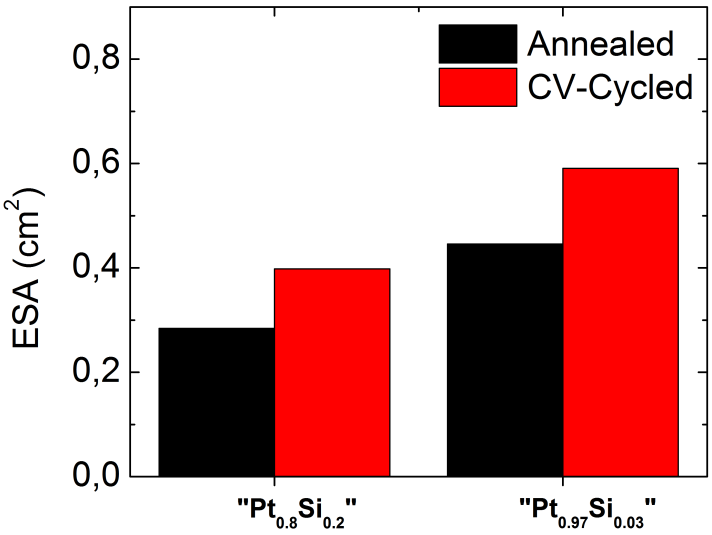

Figure 4.10: Stabilization effects on annealed Pt-Si alloys in 0.1 M $HClO_4$ at 10 mV/s. Comparison of the ECSA of annealed and CV-cycled annealed Pt-Si alloys at different compositions before (black) and after (red) CV-cycling, calculated from HAD curves.

4.4.3 Electrochemical stabilization of Pt-Si alloy surfaces

Fine mirror-like polished Pt-Si alloys (polishing procedure as described in ”Sample preparation” subsection) were ultrasonicated in de-ionized (DI) water for two 30 min sessions with a change of DI water in between. Electrochemical stabilizations of Pt-Si alloys were performed by CV cycling before electro-chemical measurements to clean the catalyst surface and to attain steady curves as shown in Figure 4.8.

All measurements of electrochemical activity were normalized to the Pt ECSA. CV curves for Pt-Si alloys exhibit a gradual stabilization after hundreds of cycles. As shown in Figure 4.8 (a). Figure 4.8 (b) shows an increase of ECSA after stabilization, which may be a result of dissolution of unstable surface species during surface cleaning. A decrease of surface Si (calculated from the XPS data shown in Figure 4.9 could be one of the reasons, whereby leaching of surface Si following the stabilization process exposes more Pt on the alloy surface.

The effects of stabilization on annealed Pt-Si alloys in comparison to ECSA of annealed and CV-cycled annealed Pt-Si alloys of varying compositions can be seen in Figure 4.10. Pre (black) and post (red) CV-cycling is calculated from HAD curves. In a similar manner to the pristine samples, annealed samples show an increase of ECSA after stabilization.

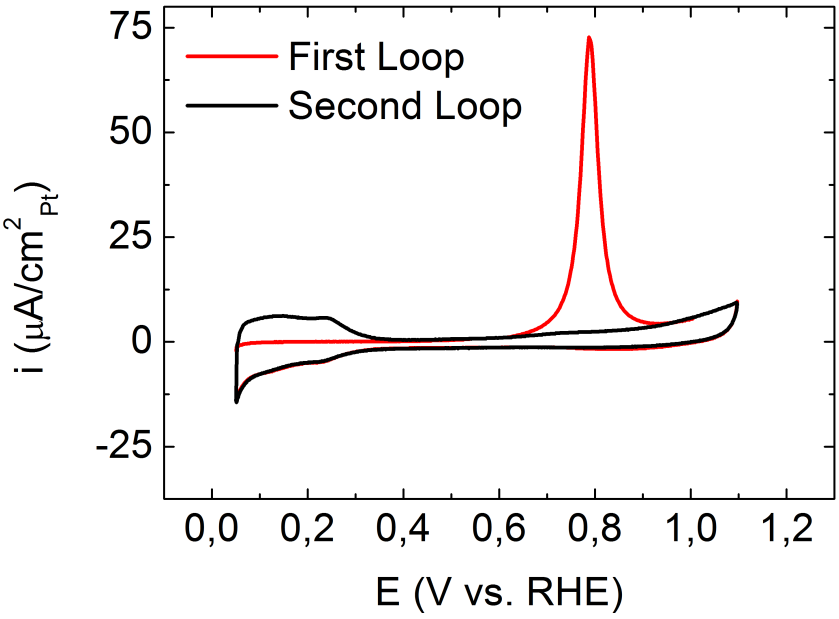

Figure 4.11: CO electro-oxidation stripping curves of pristine "Pt0.8Si0.2" alloy in 0.1 M $HClO_4$ at 5 mV/s.

4.4.4 Carbon monoxide electro-oxidation activity of Pt-Si alloys

As carbon monoxide commonly serves as a model system towards understanding the electrocatalysis of small organic molecules [**?**, 129, 131, 134, 139], Pt-Si alloys were first analysed for CO electro-oxidation activity by anodic stripping cyclic voltammetry. Figure 4.11 is an example of CV for CO stripping of "Pt0.8Si0.2".

Figure 4.12 (a) shows the specific activity of pristine "Pt0.5Si0.5", "Pt0.8Si0.2" and "Pt0.97Si0.03" alloys, defined as the current normalized to Pt ECSA, as a function of potential versus reversible hydrogen electrode (RHE). The onset and peak oxidation potentials of adsorbed CO (CO_{ad}) for the Pt-Si alloys shifted to lower potentials with increasing Si concentrations. Figure 4.12 (b) shows CO specific current normalized to Pt ECSA for pristine Pt-Si alloys against surface Si concentrations at 0.7 V versus RHE. For the Pt–Si alloy oxidation started at a lower potential than Pt alone, likely due to the necessary oxygenated species being formed at lower potentials on Si. This hypothesis is supported by the observation that on "Pt0.5Si0.5" CO is oxidized at lower potentials than on other materials. All Pt-Si alloys exhibited much higher CO specific activities seen as shifts towards lower potentials for the onset and peak oxidation potentials of CO_{ad} compared to that on Pt. The intrinsic electro-oxidation activity of CO_{ad} on pristine Pt-Si alloys was found to be enhanced with increasing Si concentrations.

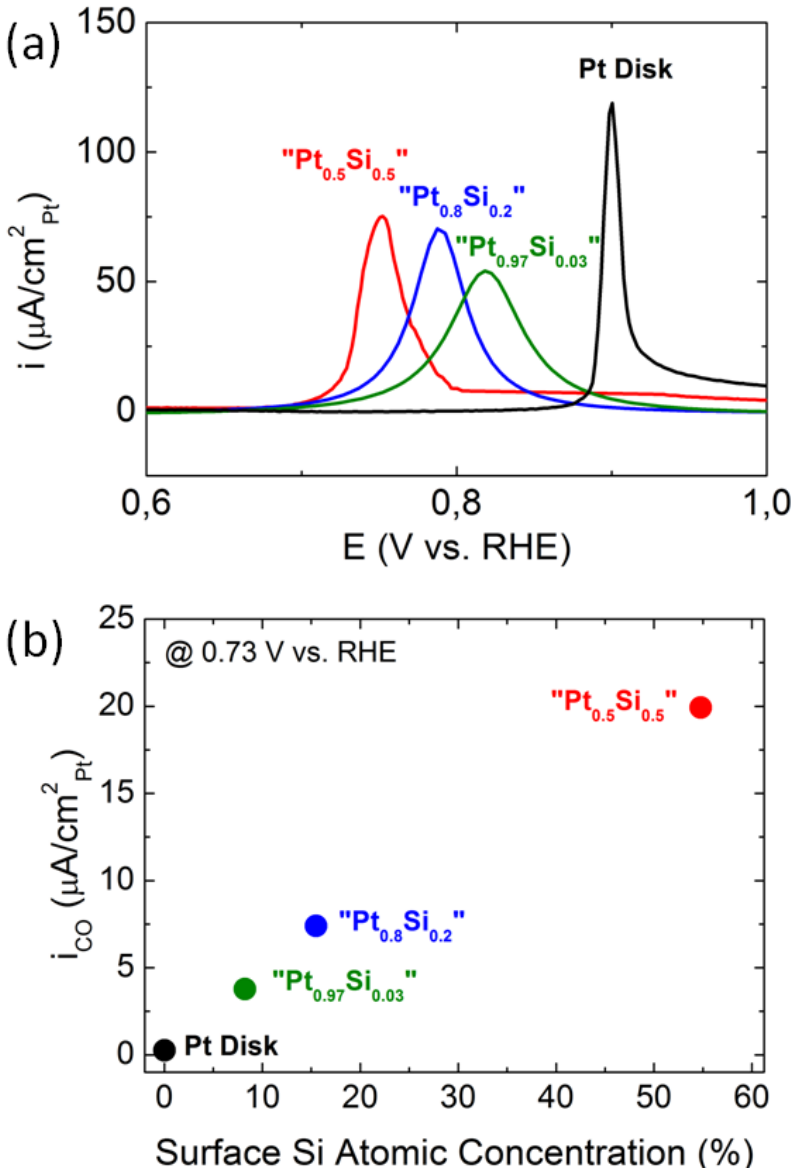

Figure 4.12: CO electro-oxidation activity on pristine Pt-Si alloys with compositions: ”Pt0.5Si0.5”, ”Pt0.8Si0.2” and ”Pt0.97Si0.03” measured at room temperature. (a) Specific electro-oxidation currents (normalized to ECSA) of CO_{ad} on pristine Pt-Si alloys in 0.1 M $HClO_4$ at 5 mV/s. (b) CO electro-oxidation current at 0.7 V vs. RHE against surface Si concentration obtained by XPS measurements.

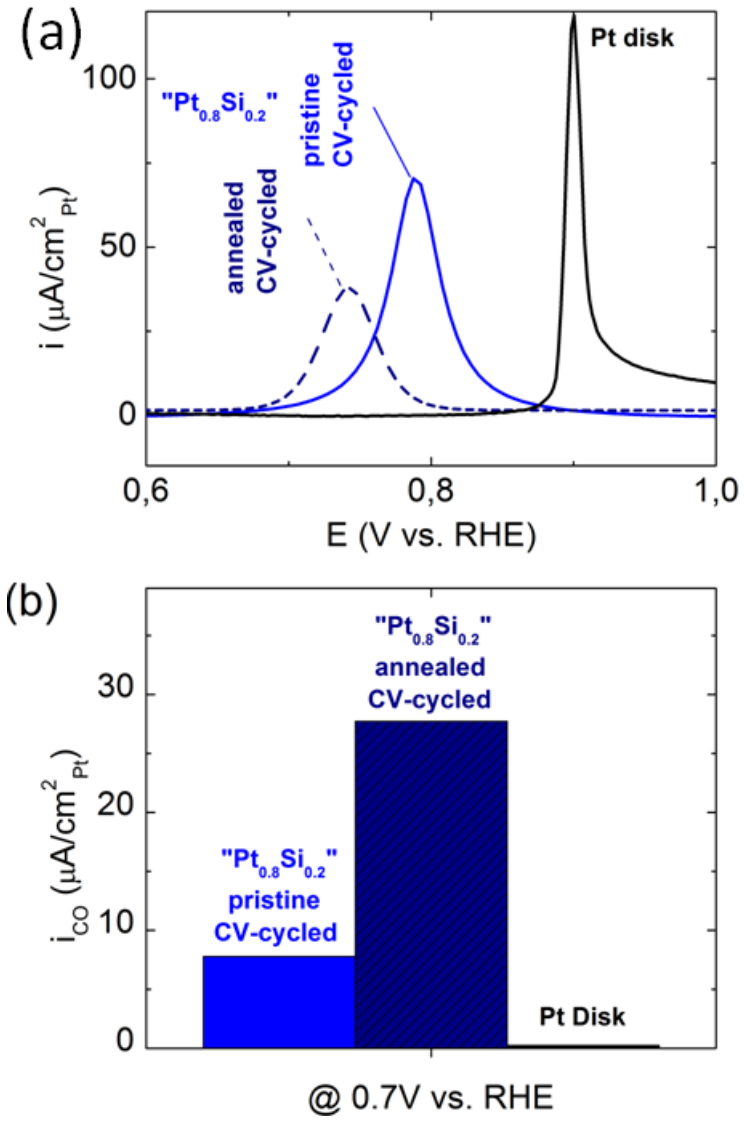

Figure 4.13: CO electro-oxidation activities on annealed vs. pristine "Pt0.8Si0.2" alloys, measured at room temperature. (a) Specific electro-oxidation current (normalized to ECSA) of CO_{ad} on annealed vs. pristine "Pt0.8Si0.2" alloys in 0.1 M $HClO_4$ at 5 mV/s. (b) CO specific current (normalized to Pt ECSA) for annealed vs. pristine "Pt0.8Si0.2 " alloys at 0.7 V vs. RHE in 0.1 M $HClO_4$ at 5 mV/s.

The annealed Pt-Si alloys exhibited even higher electro-oxidation activity than pristine samples as seen in Figure 4.13 (a) which shows the specific electro-oxidation current (normalized to ECSA) of CO_{ad} on annealed vs. pristine "Pt0.8Si0.2" alloys. At 0.7 V (versus RHE). In addition the specific current of CO electro-oxidation tends to increase in "Pt0.8Si0.2" after annealing, as shown in Figure 4.13 (b). This activity enhancement may be caused by increased uniformity of the Pt-Si atom arrangements after annealing (formation of more pronounced Pt3Si phase), which was also observed in "Pt0.97Si0.03" alloy (Figure 4.14 (a) and (b)).

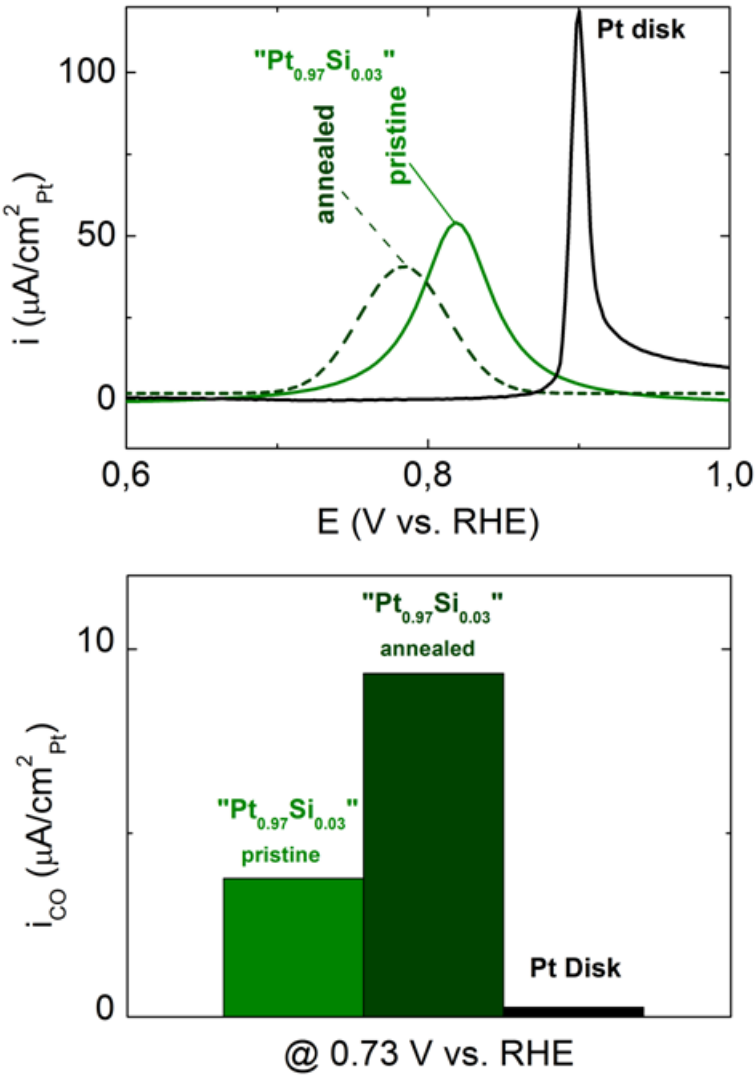

Figure 4.14: CO electro-oxidation activity on annealed vs. pristine "Pt0.97Si0.03" alloy, measured at room temperature. (a) Specific electro-oxidation current (normalized to ECSA) of CO_{ad} on annealed vs. pristine "Pt0.97Si0.03" alloy in 0.1 M $HClO_4$ at 5 mV/s. (b) CO specific current (normalized to Pt ECSA) on annealed vs. pristine "Pt0.97Si0.03" alloy at 0.7 V vs. RHE in 0.1 M $HClO_4$ at 5 mV/s.

4.4.5 Methanol electro-oxidation activity of Pt-Si alloys

Cyclic voltammetry curves for methanol electro-oxidation on pristine samples are shown in Figure 4.15. Black curves represent the first oxidation loops, while red curves were measured after 10 cycles. (Left) Original oxidation curves normalized to Pt ESA. (Right) Background-corrected oxidation currents normalized to Pt ECSA of MOR for un-annealed Pt-Si alloys. Methanol electro-oxidation curves of pristine vs. annealed "Pt0.8Si0.2" and "Pt0.97Si0.03"

alloys are shown in Figure 4.16 and 4.17, respectively. Here, similar black curves represent the first oxidation loops, while red curves were measured after 10 cycles. (Left) Original oxidation curves normalized to Pt ESA. (Right) Background-corrected oxidation currents normalized to Pt ESA. The methanol electro-oxidation reaction (MOR) activities of Pt-Si alloys were measured in an Ar-saturated solution of 1 M CH_3OH in 0.1 M $HClO_4$ with a scanning rate of 50 mV/s.

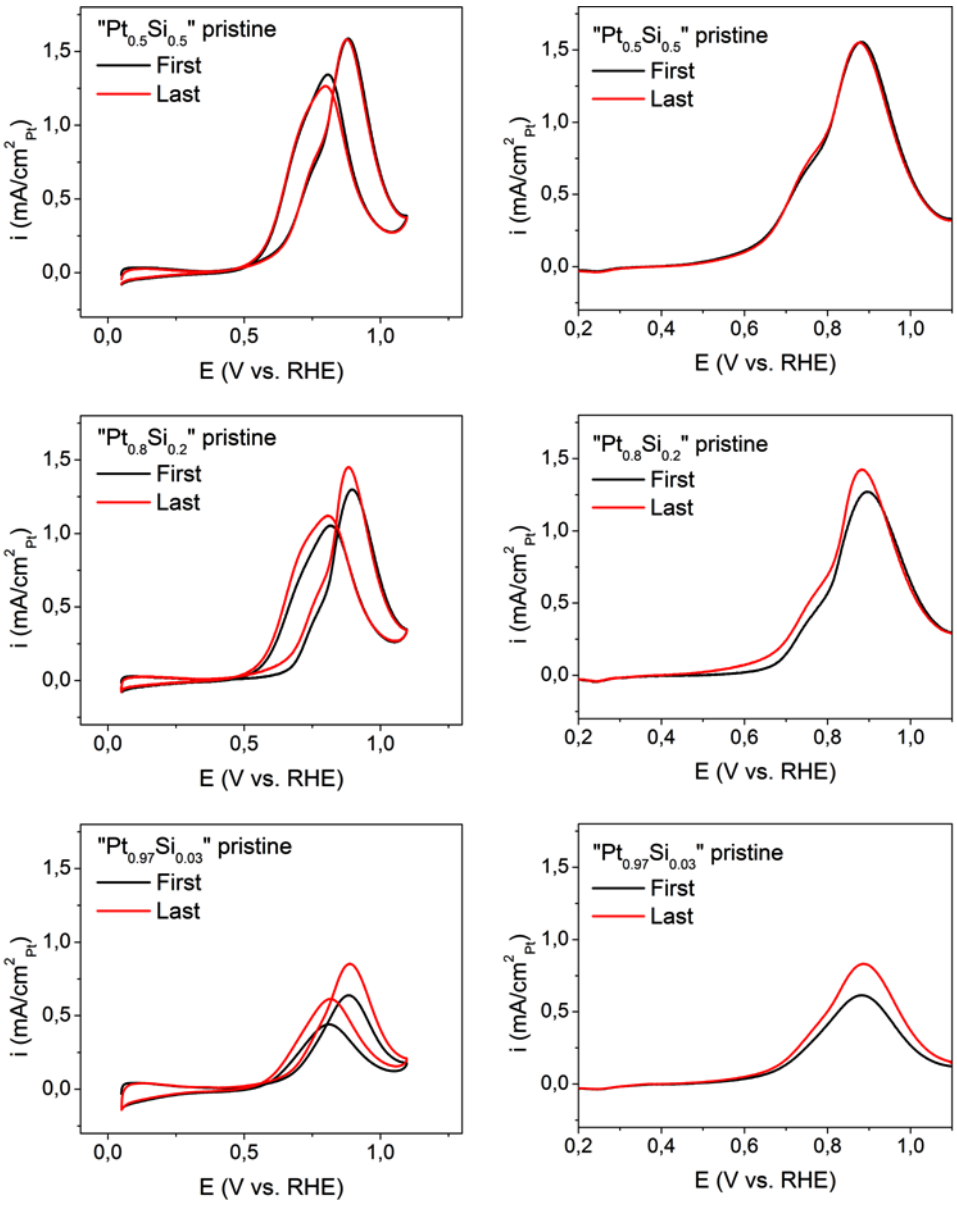

Figure 4.15: Methanol electro-oxidation curves of Pt-Si pristine alloys in 0.1 M $HClO_4$ in 0.1 M $HClO_4$ at 50 mV/s at different compositions, measured at room temperature. The black curves were the first oxidation loops, while the red curves were measured after 10 cycles. (Left) Original oxidation curves normalized to Pt ECSA. (Right) Background-corrected oxidation currents normalized to Pt ECSA of MOR for unannealed Pt-Si alloys.

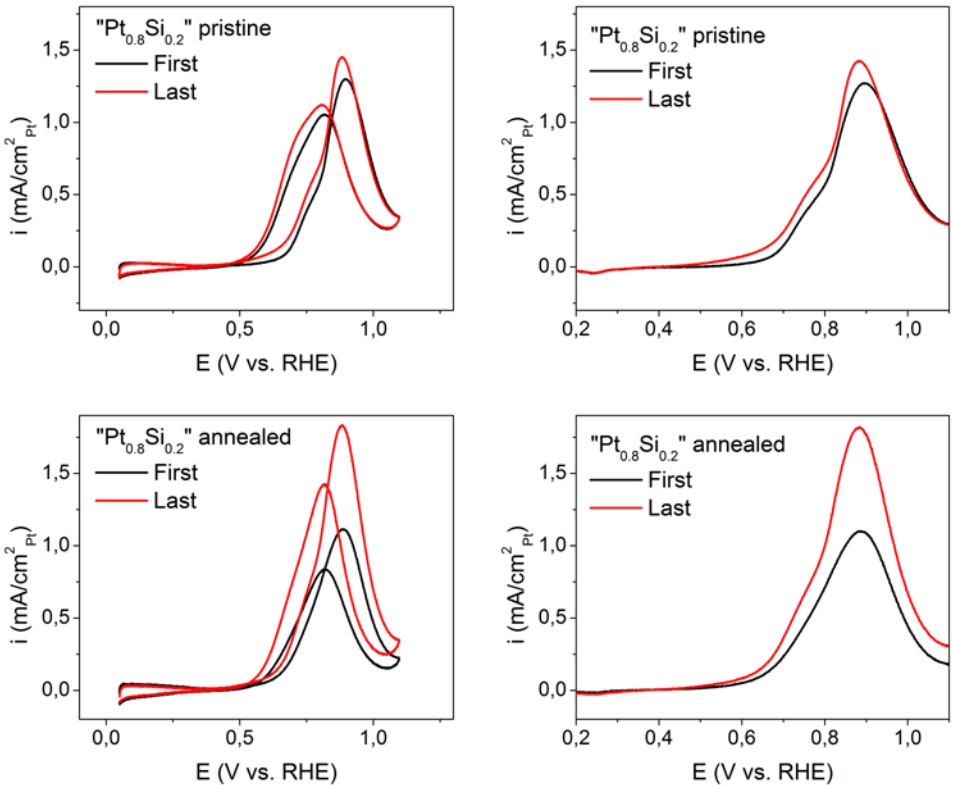

Figure 4.16: Methanol electro-oxidation curves of pristine and annealed "Pt0.8Si0.2" alloys in 0.1 M $HClO_4$ at 50 mV/s at different compositions, measured at room temperature. The black curves were the first oxidation loops, while the red curves were measured after 10 cycles. (Left) Original oxidation curves normalized to Pt ECSA. (Right) Background-corrected oxidation currents normalized to Pt ESA. of MOR for pristine Pt-Si alloys.

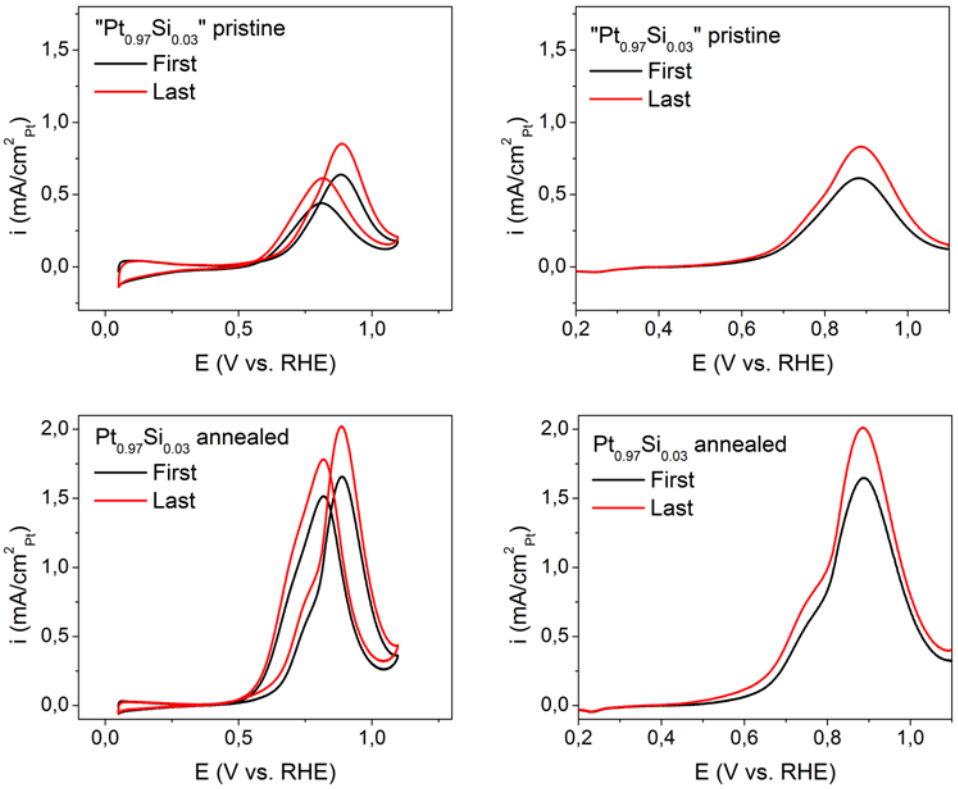

Figure 4.17: Methanol electro-oxidation curves of pristine and annealed "Pt0.97Si0.03" alloys in 0.1 M $HClO_4$ with 50 mV/s at different atomic % compositions, measured at room temperature. The black curves were the first oxidation loops, while the red curves were measured after 10 cycles. (Left) Original oxidation curves normalized to Pt ECSA. (Right) Background-corrected oxidation currents normalized to Pt ECSA for pristine Pt-Si alloys

The intrinsic activity (normalized to Pt ECSA and background CV corrected) for methanol electro-oxidation of Pt-Si alloys was also found to rise with increasing Si concentration (Figure 4.18(a)). Figure 4.18 (b) shows methanol electro-oxidation specific currents for different compositions, which tend to increase with rising Si concentrations at 0.7 V versus RHE. It can be seen that methanol electro-oxidation activity for Pt-Si alloys follows the CO electro-oxidation trend demonstrated in previous studies, whereby electro-oxidation of CO and methanol shows an intrinsic relationship [47, 52, 129]. It is generally accepted that CO_{ad} often forms during electrochemical oxidation of methanol and recognized as an indirect pathway. In contrast methanol electro-oxidation via soluble intermediates is termed the direct pathway [41, 131, 140]. In the case of the Pt-Si alloys, Si likely tends to adsorb OH species promoting the CO electro-oxidation on Pt. Consequently this enhances methanol electro-oxidation on a Pt-Si alloy. At low potentials, the MOR activity increases at increased potential due to an enhanced reaction driving force.

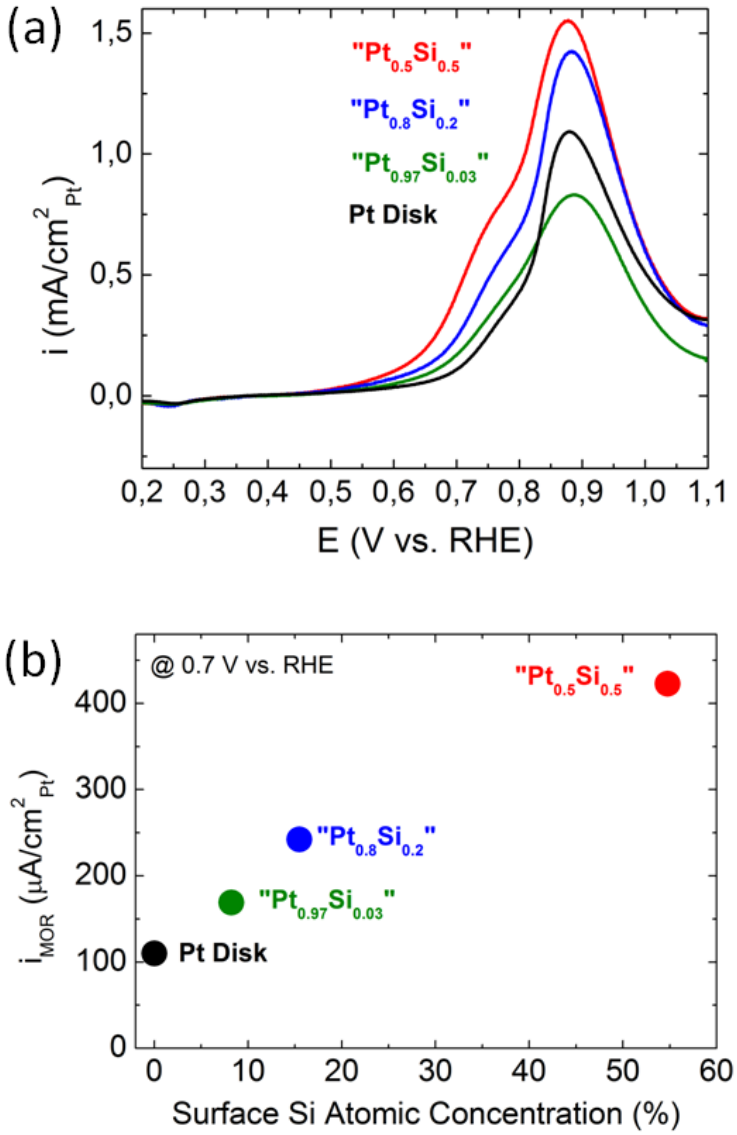

Figure 4.18: Methanol electro-oxidation activity (MOR) of Pt-Si alloys at different atomic % compositions, measured at room temperature. (a) Background-corrected specific current (normalized to Pt ECSA) of MOR for pristine Pt-Si alloys in 0.1 M $HClO_4$ at 50 mV/s. (b) MOR activity of Pt-Si alloys at 0.7 V vs. RHE versus surface Si concentration obtained by XPS measurements.

At high potentials, the catalyst surfaces were gradually covered and poisoned by surface oxygenated species. This leads to the characteristic oxidation peaks seen on the MOR curves in 4.18(a).

Following this CO electro-oxidation trend, annealed Pt-Si alloys also exhibited higher MOR electro-oxidation activity than pristine samples. Figure 4.19 (a) shows the MOR electro-oxidation currents (normalized to ECSA) of annealed vs. pristine “Pt0.8Si0.2” alloys.

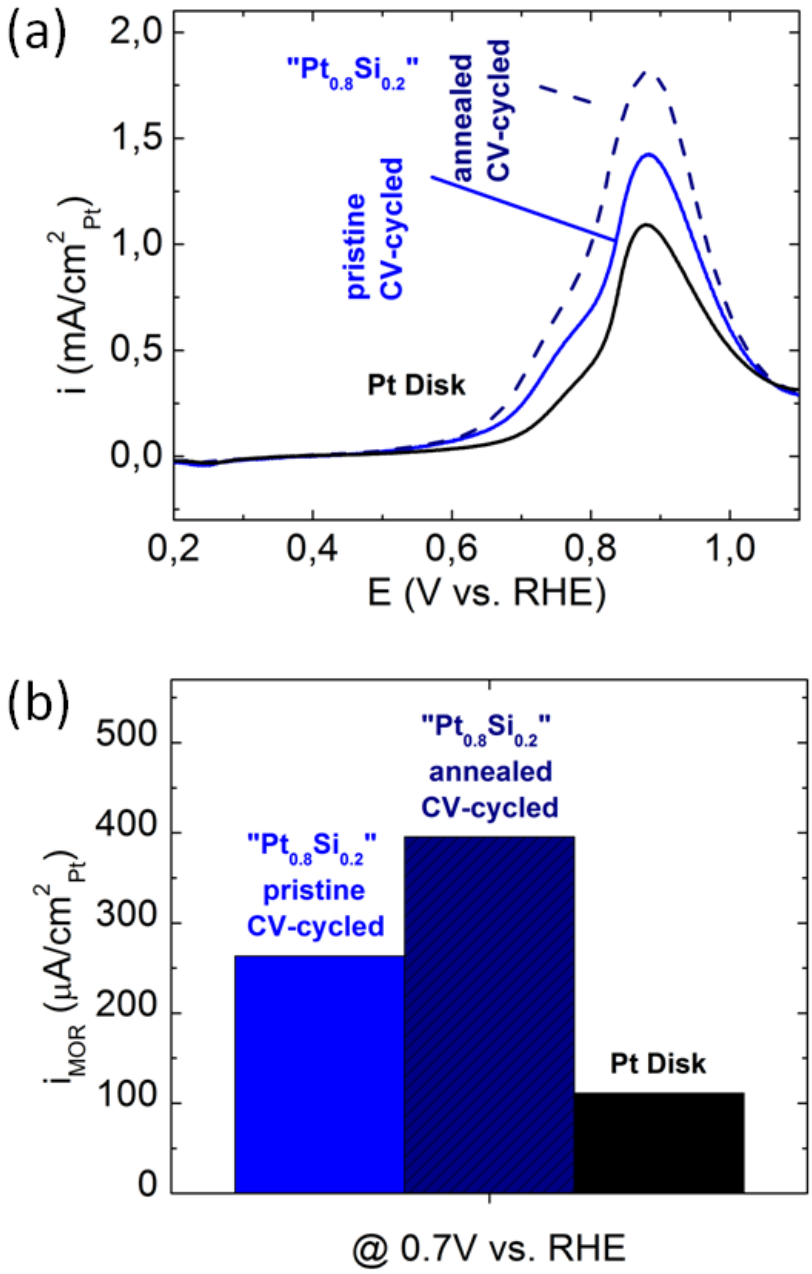

Figure 4.19: Methanol electro-oxidation activity (MOR) on annealed vs. pristine "$Pt_{0.8}Si_{0.2}$" alloy, measured at room temperature. (a) Background-corrected specific electro-oxidation current (normalized to Pt ECSA) of MOR on annealed vs. pristine "$Pt_{0.8}Si_{0.2}$" alloy in 0.1 M $HClO_4$ at 50 mV/s. (b) MOR specific current activity at 0.7 V on annealed vs. pristine "$Pt_{0.8}Si_{0.2}$" alloy in 0.1 M $HClO_4$ at 50 mV/s.

Comparison of 0.7 V vs RHE clearly demonstrates an increase of MOR specific currents for the annealed "Pt0.8Si0.2" alloy (Figure 4.19 (b)). This enhanced methanol oxidation activity may also be a result of the intrinsic relationship between CO and methanol electro-

oxidation. The annealing process has shown this to be an effective method to optimize CO oxidation activity.

Previous studies have indicated that oxidation of CO and methanol in acid, where CO reacts with adsorbed oxygenated species to form CO_2, can be understood in terms of a generalized bi-functional reaction mechanism [47, 52, 129, 131]. Therefore, Pt-Si alloys catalytic mechanism is likely similar to Pt-Ru and Pt-Sn alloy catalysts which follow Langmuir-Hinshelwood reaction types [46].

CO and methanol electro-oxidation vs. surface Si concentration from XPS for Pt-Si alloys in 0.1 M $HClO_4$ at 5 mV/s at 0.7 V vs. RHE can be found in Appendix A.

4.5 Conclusions

Characterization of a series of Pt-Si alloys for CO and methanol electro-oxidation was performed for the first time. Both the onset and peak oxidation potentials shifted to lower potentials for CO electro-oxidation whilst the onset potentials for MOR shifted to lower potentials. Intrinsic electro-oxidation activity for adsorbed CO on Pt-Si alloys increased with Si concentrations. A Langmuir-Hinshelwood reaction type was proposed and attributed to preferential adsorption of oxygenated species on the Si sites, promoting faster oxidation of CO adsorbed on Pt sites. The enhanced activity of CO and methanol electro-oxidation implies Pt-Si alloys could be a potential highly active catalyst for fuel cells operating with CO and small molecular organic based fuels. Moreover, the limited solubility of Si in acidic media may lead to higher stability than other Pt-M analogues.

Chapter 5

Pt-Si thin film alloys as methanol electro-oxidation catalyst

5.1 Introduction

Recent development of micro-devices has increased demand for similarly micro power sources, such as micro-batteries, micro-solar cells and micro-fuel cells. Micro-fuel cells are especially attractive due to their operational lifespan potential (i.e. as long as fuel and oxidant is supplied). For instance, the best lithium battery technology only produces 0.4 mega-watts per cubic-meters, whereas a micro-scale fuel cell can achieve power densities (power per unit volume) of 2000 mega-watts per cubic-meters. In other words, fuel cells potentially offer 5 to 10x greater energy densities than rechargeable batteries [9], as shown in Table 5.1. The reason for this is that fuel cells store energy as a fuel rather than as an integrated part of the system which is the case for batteries [141]. Therefore, there is significant interest in further development of high performance micro-fuel cells as a replacement in applications that would ordinarily use a battery. A portable power system must contain both the fuel cell and the means of fuel storage and delivery. In this case there are generally two choices of fuels considered; hydrogen and methanol. Other systems can be too complicated by requiring the inclusion of a reformer leading to problems with thermal management due to the higher operating temperatures. Hydrogen fuel as a gas requires a very large volume. Although it is possible to store hydrogen, even the best metal hydride storage densities, liquid methanol still has greater volumetric and gravimetric energy densities making it preferable for use in micro-fuel cells (micro-DMFCs). Employment of methanol also allows an increase in the amount of time between refueling whilst minimising system size.

Table 5.1: Comparison of thermodynamic energy densities, packaging efficiencies, and practical energy densities for various advanced battery systems and fuel cell [9]

Rechargeable batteries	Electrochemical reaction	Energy density (W h/l)	Packaging efficiency	Practical energy density (W h/l)
Li–polymer	$C_6+2LiCoO_2\rightarrow LiC_6+2Li_{0.5}CoO_2$	1350	27%	360
Ni–metal hydride	$NiOOH+MH\rightarrow Ni(OH)_2+M$	988	21%	205
"Ni–Cad"	$2NiOOH+Cd+2H_2O\rightarrow 2Ni(OH)_2+Cd(OH)_2$	439	27%	120
Fuel cells				
H_2 fuel cell	$H_2+1/2O_2\rightarrow H_2O$; unpressurized gaseous H_2 and air	2.8	50% (est.)	1.4
H_2 fuel cell	Liquid H_2 and air	4632	50% (est.)	2316
Methanol fuel cell	$2CH_3OH+3O_2\rightarrow 2CO_2+4H_2O$; 100% MeOH	4767	40% (est.)	1906
Methanol fuel cell	2M MeOH (7%) in water	334	40% (est.)	134

The potential for miniature direct methanol fuel cells has recently been identified in several works and patents [142–145]. However, a significant increase in power density is still needed, as it is currently far from the ideal. It should be possible with current technology to further improve the performance of these methanol micro-fuel cells. Two main ways to do this would involve improving the electrode's by; 1) alloying the Pt catalyst with other elements; and 2) adjusting the surface area of catalysts, as previously described. A combination of these two factors could provide optimum parameters to attain the best possible performance of the anode thereby enhancing general performance of a micro fuel cell. Electrodes are considered to cause the majority of kinetic loss in this type of fuel cell due to CO poisoning of the anode. This is a consequence of the methanol oxidation process which will ultimately cause deactivation of the cathode catalyst due to the methanol cross over [9]. To enhance the surface area of the catalysts, it is common to prepare electrodes in the form of thin films, for example as porous electrodes and selectively deposit metal layers (i.e. Pt, Pt alloys) onto tiny current collectors [75, 143, 146, 147]. The current collector usually utilized in methanol micro fuel cells is a doped Si substrate. In contrast to powdered catalysts material (i.e. fibers or tubes) thin films have an advantage - they can be directly used as electrode materials.

Supported by the findings in Chapter 4, where bulk Pt-Si alloys exhibit higher carbon monoxide and methanol electro-oxidation activities in an acid electrolyte [95], this chapter explore into Pt-Si thin films supported on the Si (100) substrate and hypothesize that they can potentially possess similar properties. For this purpose in the following chapter ways of preparing Pt-Si alloy are studied as well as methods of physical characterisation and ways to attain starting electrochemical measurements.

Review on synthesis methods for the Pt-Si thin film alloys

The formation of platinum silicides from Pt films deposited onto Si substrate at temperatures considerable below their eutectic points was first reported by Lepselter [148].The oriented growth of the interfacial PtSi layer between Pt and Si was subsequently studied in detail by Kawamura et al. [149]. In this study the determined crystallographic properties indicate that Pt films sputtered onto Si wafers react with Si at temperatures above 600°C to form Pt_2Si and PtSi. The study also showed that the temperature of heat treatment influences the preferred orientation characteristic of the interfacial PtSi layer. Low temperature formation of a Pt_2Si-like compound has also been confirmed at 350°C in a study by Hiraki et al. [150] where migration of Si into sputtered Pt films was observed. Separately Drobek et al. [151] carried out electron transmission analysis on evaporated Pt-Si systems and identified that three compounds were formed during diffusion; Pt_3Si, Pt_2Si and PtSi. In this study the initial formation of Pt_3Si was followed by the formation of Pt_2Si and PtSi phases. Subsequently the Pt_3Si compound disappeared as diffusion proceeded. Later on Shinoda (in his physico-chemical studies of platinum-silicon interfaces [152]) identified that the layered structure of the Pt-Si contact sequentially changes through Pt-Pt_2Si-Si, Pt-Pt_2Si-PtSi-Si and Pt_2Si-PtSi-Si, into PtSi-Si during heat treatment at temperatures ranging from 200°C to 700°C. It was also identified that PtSi layer possesses a preferred crystallographic orientation in the [001] direction. In addition the rate-determining process of the solid-solid reaction on the Pt-Si contact was identified as a diffusion process of Si into Pt and/or platinum silicides. The duration of heat treatment used was varied from 20 seconds to 2 hours. Pt_2Si and PtSi phases were already observed in the sample heat-treated for 5 min at 350°C in addition to the Pt diffraction lines. In the samples heat-treated for 2 hours or more, both the diffraction lines of Pt and Pt_2Si disappeared and only diffraction lies corresponding to PtSi remained. Murarka et al. [153] analysed the properties of films as a function of annealing temperature using various techniques, including x-ray analyses. At temperature range of 300 to 1000°C, annealed for 30 minutes, the silicide formation of only PtSi was detected.

In general, it can be extracted that the formation of Pt-Si thin films alloys on a Si substrate can be achieved by heat-treatment in between 200 and 1000°C with a time range from 5 min to 2 hours and longer. Formation of the Pt_3Si, Pt_2Si, PtSi and their combinations is possible. Note that the Pt thin film deposition manner, thickness and Si substrate's type and orientation various likewise.

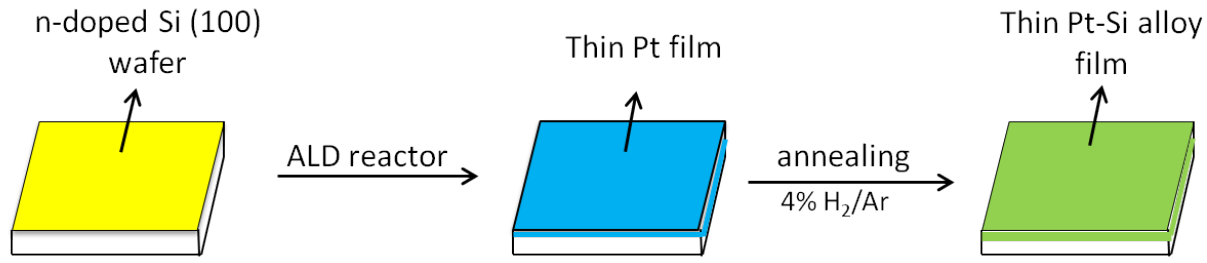

Figure 5.1: Simplified scheme for preparation of thin film Pt–Si alloys.

5.2 Synthesis of thin film Pt-Si alloys

Guided by experience reported in the literature, several steps were undertaken in order to obtain thin films of platinum silicides for the current experimental study. A simplified preparation scheme for thin film Pt–Si alloys is illustrated in Figure 5.1 and explained in detail in the following subsections.

5.2.1 Atomic Layer Deposition of Pt thin films onto Si (100) wafers

Pt films deposited onto the Si (100) n-doped wafers were prepared by Atomic Layer Deposition (ALD) and explained in Figure 5.2.

Pt films were deposited using a hot-wall, top-flow Atomic Layer Deposition reactor from Picosun (Sunale R-150, Figure 5.2, a)). The inside of the reactor is shown on Figure 5.2, b), where the lid of the ALD reactor is open. In addition to the lid, the inside of the reactor is comprised of heat reflectors, a reaction chamber lid, a precursor distribution plate (with the detailed view on Figure 5.2, c)) and four trays able to accommodate four 4" wafers simulataneously. Figure 5.2 d) represents the reaction chamber.

The temperature of the reaction chamber is measured with a thermoelement. Generally, during the deposition process the heater temperature (measured by the thermoelement) is about 70-110°C greater than the stabilized reaction chamber temperature. The intermediate space of the chamber is purged with N_2 using a fixed mass flow rate. The pressure of the intermediate space during the deposition process (measured by thermoelement) is typically 5-15 hPa. Pressure depends on the deposition temperature and gas flow rate and in the current study was measured about 300 sccm (standard cubic centimeters per minute) throughout all depositions.

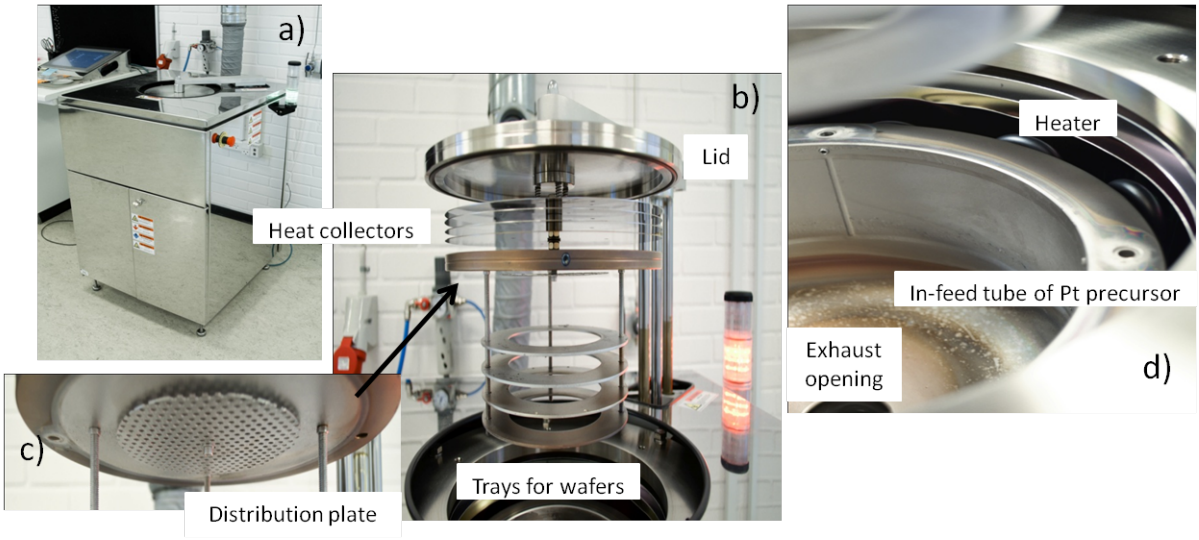

Figure 5.2: Atomic Layer Deposition reactor (Picosun Sunale R-150). DTU Nanotech.

The ALD system has room for four precursors in total; however for the deposition of thin Pt films only two precursors were used. A platinum precursor and gas phase oxygen were subsequently supplied. The source of the Pt precursor is equipped with a Picosolid Booster source system, which enables the temperature to be fixed and measured by thermoelement. During the deposition processes the system temperature was set to 55°C. Prior to deposition the precursor gas line was purged with nitrogen gas (99.999%), which also functions as the precursor vapor carrier. The N_2 gas flow rate for the precursor sources was set to 50 sccm for Pt precursor source and 150 sccm for the oxygen precursor source for all depositions. The oxygen gas flow rate was measured and recorded using a mass flow meter and controlled by pressure transducer (set to 20 hPa during pulsing).

Samples (Si wafers) to be coated with Pt thin film were placed in the middle of the tray in the chamber. The precursor used was trimethyl(methylcyclopentadienyl)platinum (MeCpPtMe3) and O_2 the reactant. This process is based on the dissociative chemisorption of O_2 on the Pt surface for oxidative decomposition of the precursor ligands [154–156]. Temperature of the Pt precursor was set to 55°C and was maintained via a Picosolid Booster source system. Pulse/purge times of MeCpPtMe3 were 1s/6s and pulse/purge times of O_2 were 5s/8s. The substrate used was n-doped Si wafers with (100) surface orientation. In total 300 cycles were deposited, resolving in a film thickness of approximately 130 Å.

Table 5.2: Pt-Si thin films. Annealing methods. Method A - temperature dependent and method B - time dependent.

Method A - temperature dependent	**Method B - time dependent**
30 min at:	**600°C at:**
200°C	30 min
350°C	2 hours
400°C	8 hours
500°C	24 hours
600°C	-

5.2.2 Annealing of the ALD deposited Pt thin films

The second step of the Pt-Si alloy thin film preparation involved annealing of the Pt films which had been deposited onto the n-doped Si (100) wafers at the set temperatures. Two methods of annealing were employed, temperature dependent and time dependent (methods A and B, respectively). These two methods were used in order to form platinum silicides and are presented in Table 5.2. For annealing method A, samples were heat treated at temperatures of 200°C, 350°C, 400°C, 500°C and 600°C for 30 min each. Annealing method B involved heat treatment of samples for 30 minutes, 2 hours, 8 hours and 24 hours at temperature of 600°C each. The temperatures range was chosen in order to clarify the optimum condition for platinum silicide formation. It would also allow determination of whether it is possible to form a Pt silicide layer with different phases; i.e. Pt_3Si, Pt_2Si, and PtSi (if any). It would also eventually allow the behaviour of these platinum silicide phase(s) towards the methanol electro-oxidation to be studied.

Annealing of all samples was conducted in a furnace under a controlled 4% H_2/Ar atmosphere.

5.3 Structural characterization of Pt-Si thin film alloys

The samples obtained after ALD and annealing were characterized using X-ray diffraction, Raman spectroscopy, Scanning Electron Microscopy and Atomic Force.

5.3.1 X-Ray diffraction

The diffraction analysis was made as follows. Each heat-treated sample was mounted on a rotating sample holder (for use with X-ray Diffractometer (XRD) Bruker D8). A Large area GADDS 2-dimensional detector was used during spinning in order to increase the amount

of scattered X-rays observed by the Debye diffraction rings and increase the number of crystallites contributing to the measured pattern. A scanning region from the 15° to 75° window in the 2θ range was chosen and data collected using Copper Kα radiation.

Typical X-ray diffraction patterns for the thin film Pt-Si samples heat treated for different durations and temperatures are shown in Figure 5.3 a) and b). Figure 5.3 a) shows the XRD patterns for method A, whereby samples were annealed for 30 min in temperature range between 200 and 600°C. XRD patterns of the ”as-deposited” by ALD thin Pt film on Si (100) wafer show only Pt diffraction peaks, namely Pt(100) and Pt(200). No tetragonal or hexagonal Si_2Pt phases in the as-deposited Pt films were observed. In samples heat-treated at 200 to 600°C, no diffraction lines corresponding to Pt_3Si, Pt_2Si or PtSi phases were observed. The only difference between samples observed was that the Pt (111) peak is slightly bigger and wider for the 600°C Pt film, which could be due to agglomeration of Pt particles. These results were surprising and are not in concurrence with currently published literature data. Current literature suggests Pt_3Si and Pt_2Si phases were observed at 350°C after 5 min of heat treatment [152] and a PtSi phase observed in a stable manner after 30 min heat treatment at 300°C [153]. However, it should be noted that previously published results depend on sample parameters which may be different than those employed here. Figure 5.3 b) shows the XRD patterns for samples heat treated by method B (i.e. heat treatment at 600°C) starting from 30 min up to and including 24 hours. After 2 hours of heat treatment it can be seen that; formation of PtSi phase has occurred, a Pt(111) peak is still remaining whilst a Pt (200) peak has disappeared under the domination of the PtSi phase peaks.

Following 8 hours of heat treatment, a very small peak of Pt phase can be observed and the PtSi phase dominates. After 24 hours of heat treatment no Pt peaks are observed while PtSi phase peaks are represented by the same peaks with the exception that the PtSi (101) peak is weaker and an additional PtSi (021) peak is now observed. It should be noted here that the strongest lines correspond to (101) reflections of PtSi after 2 and 8 hours of heat treatment. This observations is in contrast to the studies of Murarka et al. [153], who found that the strongest lines for the samples annealed above 800°C are Pt (002) and Pt (101), in that order. In the current study a Pt (002) peak was not observed. However, differences in the methods of deposition should be taken in to account. In the current study the ALD method was used. In contrast Murarka et al. [153] used dc magnetron sputtering from two targets where temperatures of the substrate did not exceed 50°C. Moreover, a longer heat treatment time may also contribute to this discrepency, (Murarka et al. used 30 min used annealing all temperatures). Murarka et al. found that the Pt (101) intensity increased up to 500°C, invariably between 500 and 700°C and decreased to small values when annealed at 1000°C.

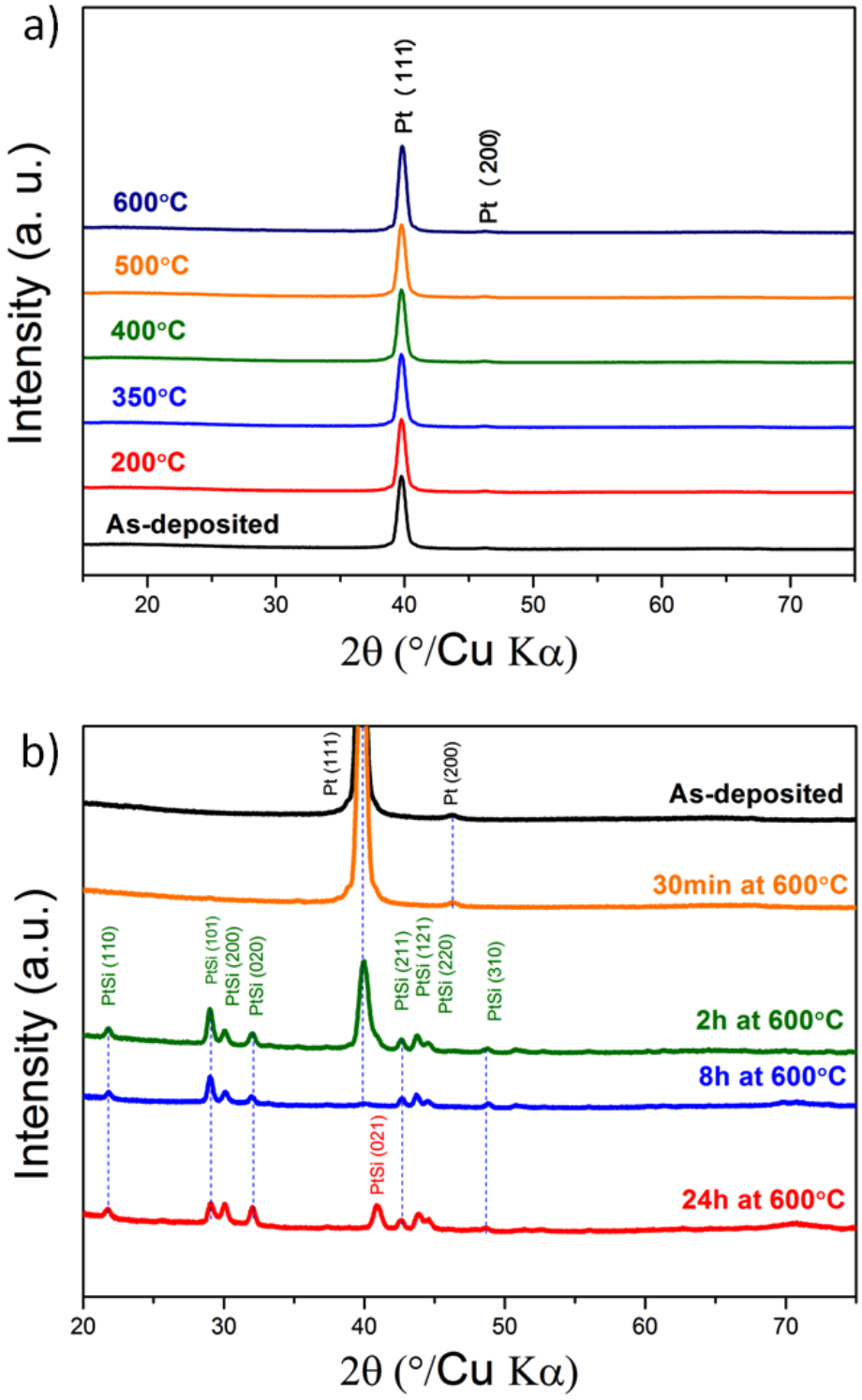

Figure 5.3: XRD patterns for Pt-Si thin film samples heat treated at different times and temperature ranges. a) XRD patterns for the method A with samples annealed for 30 min between 200 and 600°C and b) XRD patterns for the method B with samples annealed at 600°C between 30 min up to 24 hours.

Observations were similar in the current study but also a dependence on time of treatment was observed. In this study the Pt (101) peak grew with a longer heat treatment time, invariably between 2 and 8 hours of heat treatment and was fully depleted after annealing for 24 hours at 600°C. Samples annealed for 24 hours at 600°C showed a change in the preferred orientation indicating a decrease in PtSi concentration in the film. Murarka et al. [153] proposed that this was caused by instability of the PtSi phase at higher temperatures. In the current study a longer heat treatment time could have a similar effect. The observations could also be caused by Pt diffusion from PtSi into the underlying silicon. The greater the treatment time the deeper the penetration of Pt into the silicon substrate.

5.3.2 Raman spectroscopy

As-deposited by ALD and annealed samples (formed by both methods A and B) were also verified by Raman spectroscopy. The detection of Raman scattering from Pt or Pt-Si films was conducted using a LabRAM HR UV-VIS-NIR Raman system from HORIBA Scientific equipped with a BX41 confocal microscope. Scattered light was collected by an 800 mm focal length astigmatic flat field spectrograph, 1800 mm^{-1} grating and 632 nm laser. Hole and slit size were 100 μm each. 50xLWD objective (N.A. = 10.6 mm) was used. An average of 4 scans with a 5 min exposure was employed. During measurement samples were inserted in the Linkam THMS600 cell under an Ar atmosphere in order to reduce the intensity of the inelastically scattered light from atmospheric molecules. Measurements were made at room temperature. For all samples background subtraction was done with respect to Si peak. The photon energies of the Raman spectra measured are the same as those observed in other studies [157, 158] for Si and PtSi. The dominant lines fall between 220 and 350 cm^{-1} for Si and between 50 and 200 cm^{-1} for PtSi, thus defining the spectral range of interest.

Figure 5.4 show Raman spectra (left side) and optical microscope pictures of the spots where Raman spectra were taken (right side) for samples annealed by method A. Only samples annealed at 200°C and 600°C for 30 min are shown. 600°C is represented by 2 Raman spectra taken from 2 different spots as shown on the relative optical microscope pictures. It can be seen that the sample annealed for 200°C for 30 min shows no peak for platinum silicide and only shows a peak relative to the Si (100) wafer at around 305 cm^{-1}, identical to relative intensities obtained by Tsang et al. [158, 159]. Unfortunately Pt peaks cannot be observed using Raman spectroscopy as the noble metal is not ”Raman active”, due to translational symmetry of the cubic lattice structure of the Pt.

Surprisingly it was found that the Raman spectra were able to detect the PtSi alloy in samples annealed for only 30 min and at 600°C, which was not detected by XRD as pre-

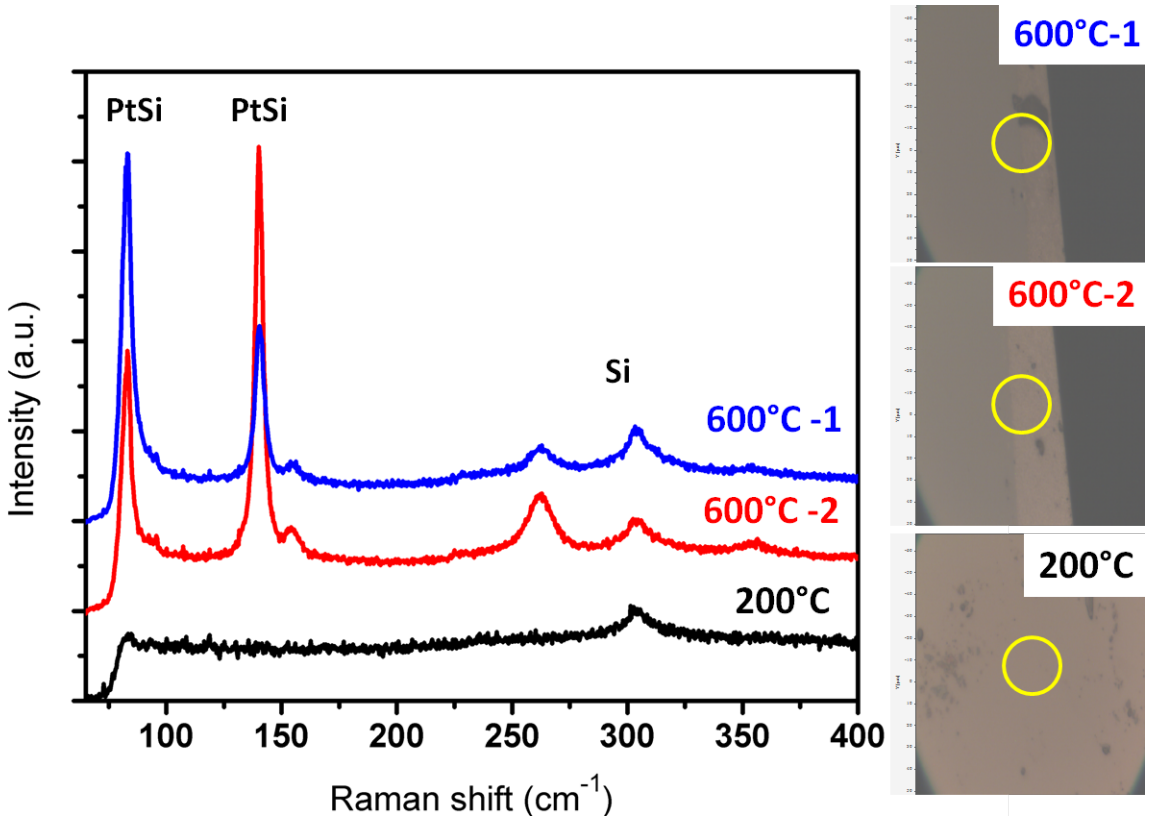

Figure 5.4: Raman spectra (left side) and relative optical microscope pictures (right side) of Sample annealed by method A: 30 min annealing in the range of 200 to 600°C. A yellow circle marks the the area, where the Raman spectra on the left were recorded.

viously described. However, considering it was found in only 2 localized spots and both were close to the edge of the sample and XRD was taken from the areas where no cracks were visually observed; platinum silicide could form in these areas due to cracks in the initial sample, also damage and heating of the silicon layers may also have induced Pt-Si alloy formation. It could be concluded that that Pt-Si alloy forms first near defect sites and then covers the entire surface for longer annealing time, which agrees with the XRD data.

Figuire 5.5 shows Raman spectra for samples annealed by method B (samples annealed at 600°C for 30 min, 2 hours, 8 hours and 24 hours). Four Raman scans each subjected to a 5 min exposure are shown. It can be seen that for 2 hours annealed sample peaks are not concurrent. For this sample some are sharp and high whilst some are broad and short and the relative intensities of the 82 and 140 cm^{-1} lines are different. This could be a result of a inhomogeneous sample surface even after 2 hours of heat treatment. Samples annealed for 8 and 24 hours show more concurrent trends in peak relative intensities and look similar. This is potentially a result of Pt being fully reacted to PtSi and completely covering the Si surface.

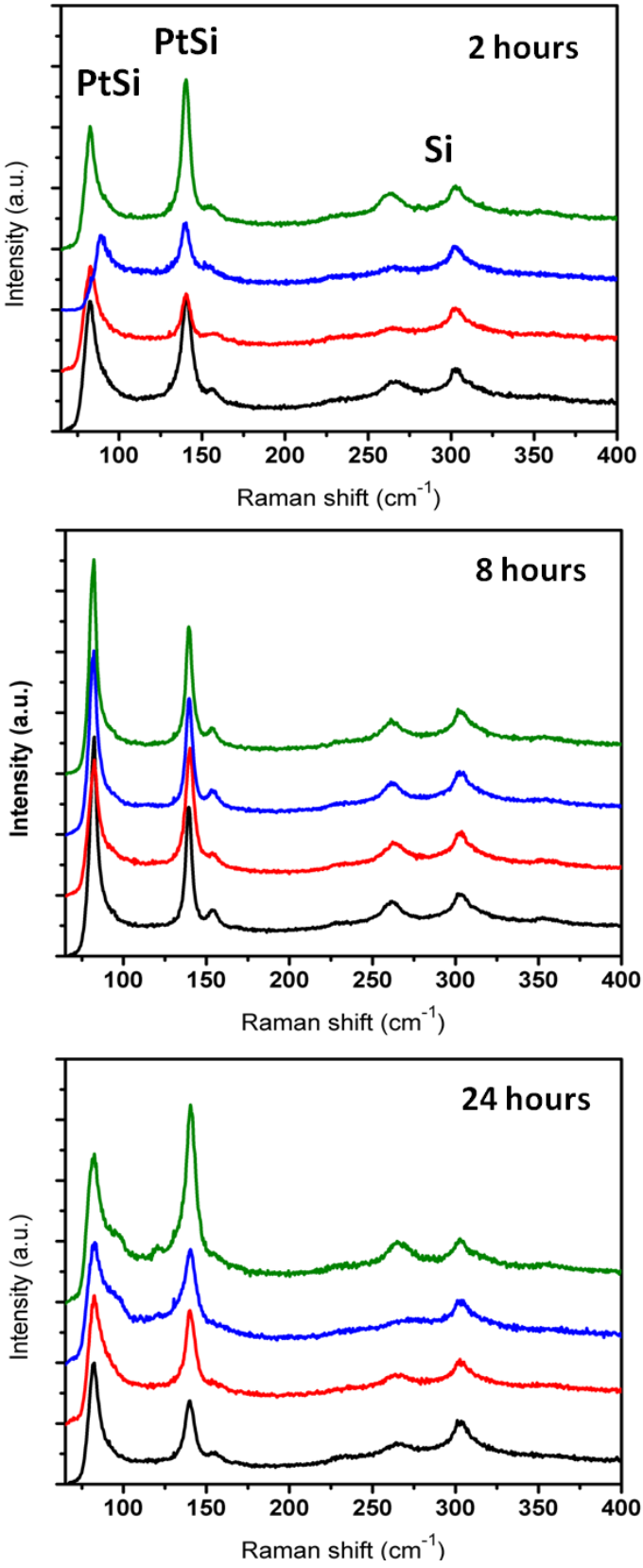

Figure 5.5: Raman spectra for samples heat treated by method B: 600°C for 30 min, 2 hours, 8 hours and 24 hours annealing. Four Raman scans with 5 min exposure shown for each time of annealing.

Figure 5.6 presents a summary of the Raman spectra (left side) and relative optical microscope pictures (right side) for samples heat treated by method presented. Differences in the spectra could be due to differences in the orientation of the PtSi growth which manifest when annealing for different periods of time. Here it can be seen that the sample annealed for 24 hours has a broader peak than other samples. Such broadening is common when the crystalline quality of a sample is poor [158]. Furthermore this hypothesis is in agreement with XRD data, which indicates a decrease of the PtSi concentration in the film annealed for 24 hours which could be due to Pt diffusion from PtSi into the underlying silicon.

Thus, Raman spectroscopy data were in general found to be well correlated to currently published literature confirming a PtSi phase was observed. In addition the Raman analysis was also in agreement with the data obtained by XRD analysis.

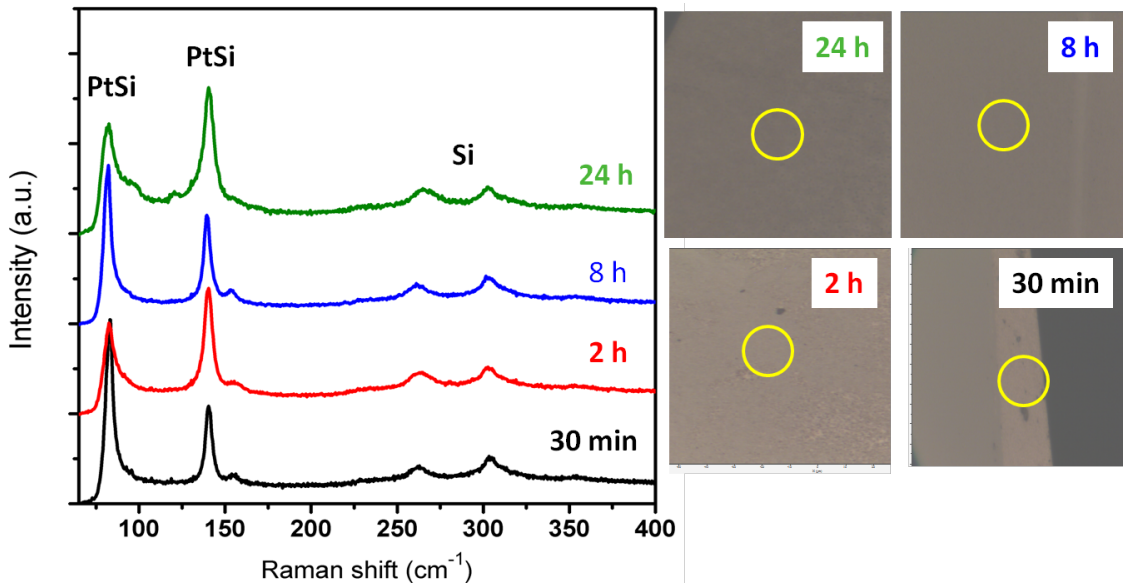

Figure 5.6: Summary of Raman spectra (left side) and relative optical microscope pictures (reght side) for samples heat treated at 600°C each and different annealing times. Yellow circles indicate areas, where Raman spectra were recorded.

5.3.3 Environmental scanning electron microscopy

Several thin film samples were also analysed by environmental scanning electron microscopy (ESEM) and energy dispersive spectroscopy (EDS) to characterise silicide surfaces and the formed agglomerations. Images were taken using FEI/Philips XL30 FEG ESEM equipped with Energy Dispersive X-ray Analyser from EDAX. Spectra were collected up to 15 keV. The final results were determined as the average of five different spot measurements on the sample. Figure 5.7 presents environmental ESEM and EDX results for thin Pt film on Si

(100) as-deposited by ALD (left side, a), c) and e)) and for a sample annealed for 2 hours at 600°C (right side, b), d) and f)). As seen from EDS - Figure 5.7 a) and b), only PtM and SiK peaks were identified for all samples, inferring no impurities were introduced in the ALD or annealing process, respectively. The ESEM analysis is represented by 20 μm and 2 μm images for each sample. ESEM images of the as-deposited thin film sample (5.7, c), e)) show a well dispersed surface with no agglomerations evident. For the 2 hour, 600°C annealed sample ESEM images show significant change in surface morphology and the presence of agglomerated particles of Pt silicide, especially at the 2 μm scale (5.7, d), f)). SEM images of samples heat treated for 30 min at different temperatures did not show significant changes in surface morphology (not shown here). Results are generally well correlated with XRD and Raman measurements which did not show presence of Pt-Si alloy in 30 min sample however did indicate its presence for the 2 hours, 600°C annealed sample. ESEM images for samples annealed for 8 and 24 hours should be attained in future work in order to complete the picture.

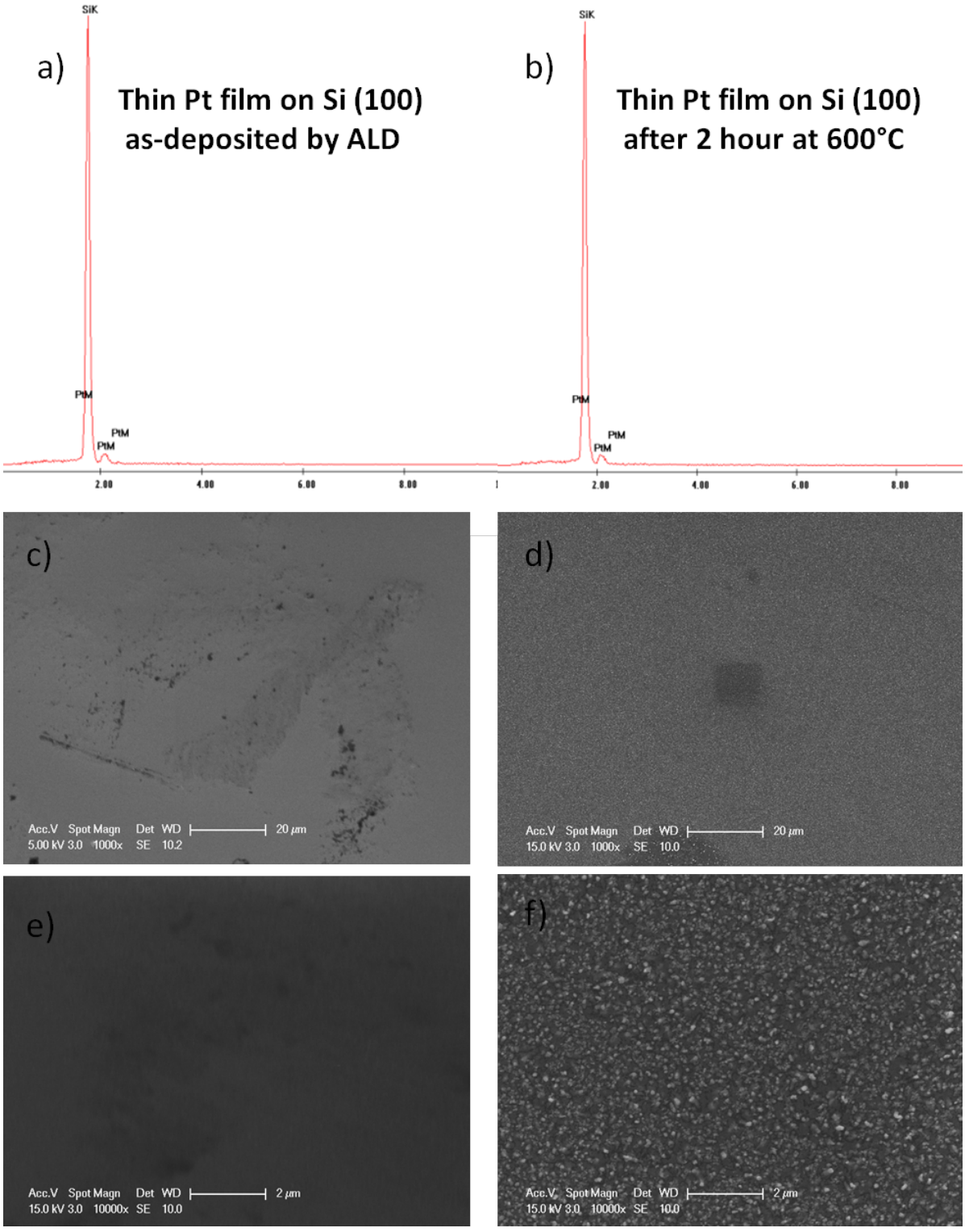

Figure 5.7: EDS spectra a) and ESEM images c) - 20 µm and e) - 2 µm for the Pt thin film on Si (100) as-deposited by ALD; EDS spectra b) and ESEM images d) - 20 µm and f) - 2 µm for the Pt thin film on Si (100) after annealing for 2 hours at 600°C.

5.4 Electrochemical characterisation of Pt-Si thin film alloys

5.4.1 Sample preparation

As-prepared by ALD and annealed samples (Figure 5.8 a) were treated in a special way in order to perform electrochemical measurements. A typical working electrode is presented in Figure 5.8 b and its schematic treatment presented in Figure 5.8 c. Electrical contacts were fixed to the top part of the film facing the Pt or Pt-Si alloy. Gallium- indium eutectic (Sigma-Aldrich, 99.99%) was fixed onto the Pt or Pt-Si alloy film side, a Ti wire (Sigma-Aldrich, 99.99%) was installed on top, fixed with silver paint (Ted Pella, Leitsilber 200) and dried for one hour. The back and sides of the electrode (as well as the wire) were covered with a non-conductive, chemically resistant epoxy (Omegabond 101) and dried for 6 hour. This was to ensure that only the catalyst surface was exposed to the electrolyte as described by Stoerzinger et al. [160].

5.4.2 Set-up and procedure for electrochemical measurements

Electrochemical measurements were conducted using a standard three-electrode cell at room temperature. A Pt wire and saturated calomel electrode (SCE) (Analytical Sensor, Inc.) were used as counter and reference electrodes, respectively. The SCE potential was calibrated to the RHE scale. Initially cyclic voltammetry measurements were performed to electrochemically clean the thin film surfaces in an O_2-free 0.1 M $HClO_4$ electrolyte saturated for 30-min by ultra-high-purity Ar gas (99.999%, Airgas). The thin film electrodes were cycled between 0.05 and 1.0-1.1 V (vs. RHE) at a scan rate of 200 mV/s for 5 cycles to reach steady state. Subsequently ECSA and methanol electro-oxidation measurements were performed on the surface-stabilized electrodes. A CV scan at 200 mV/s with a voltage range between 0.05 and 1.1 V (vs. RHE) was used to calculate the ECSA from the charge integration of hydrogen adsorption and desorption areas between 0.05 and 0.35 V (vs. RHE) with a conversion factor of 210 µC/cm$^2{}_{Pt}$ after double-layer correction. The methanol electro-oxidation activities were measured between 0.05 and 1.1 V (vs. RHE) at 50 mV/s in O_2-free 0.1 M $HClO_4$ and 1 M CH_3OH electrolyte prepared by 30-min bubbling of ultra-high-purity Ar gas (99.999 %, Airgas). All activity measurements were normalized by Pt ECSA.

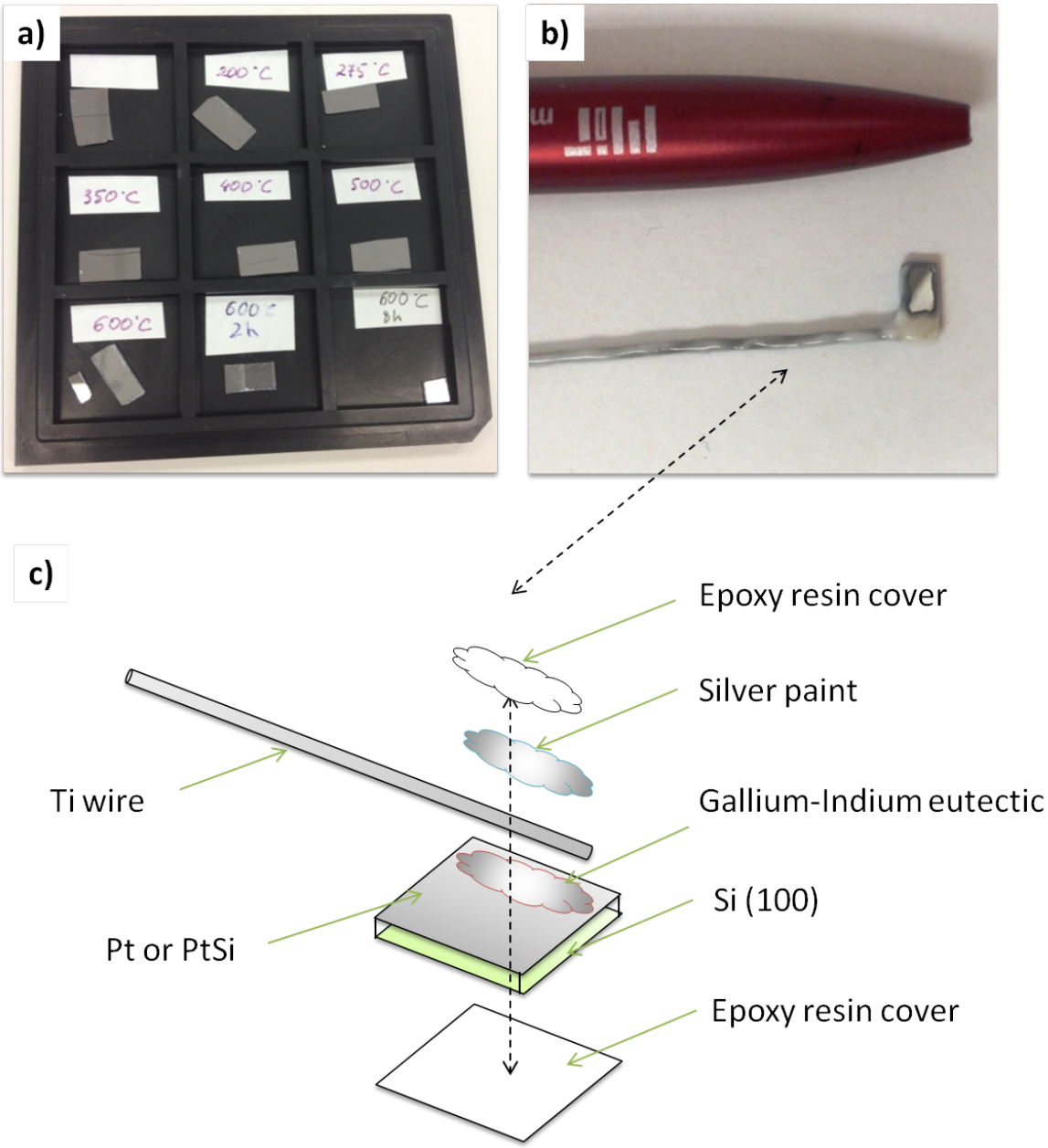

Figure 5.8: Thin film working electrode preparation scheme. a) initial samples, b) sample after treatment - working electrode, c) schematic view of the sample treatment.

5.4.3 Electrochemical surface area analysis

The hydrogen adsorption cyclic voltammograms for Pt and PtSi films on Si(100) as deposited and annealed at 600°C for different times is presented in Figure 5.9 and summarized in Table 5.3. The results show evolution of the electrochemical surface area (ECSA) versus the time.

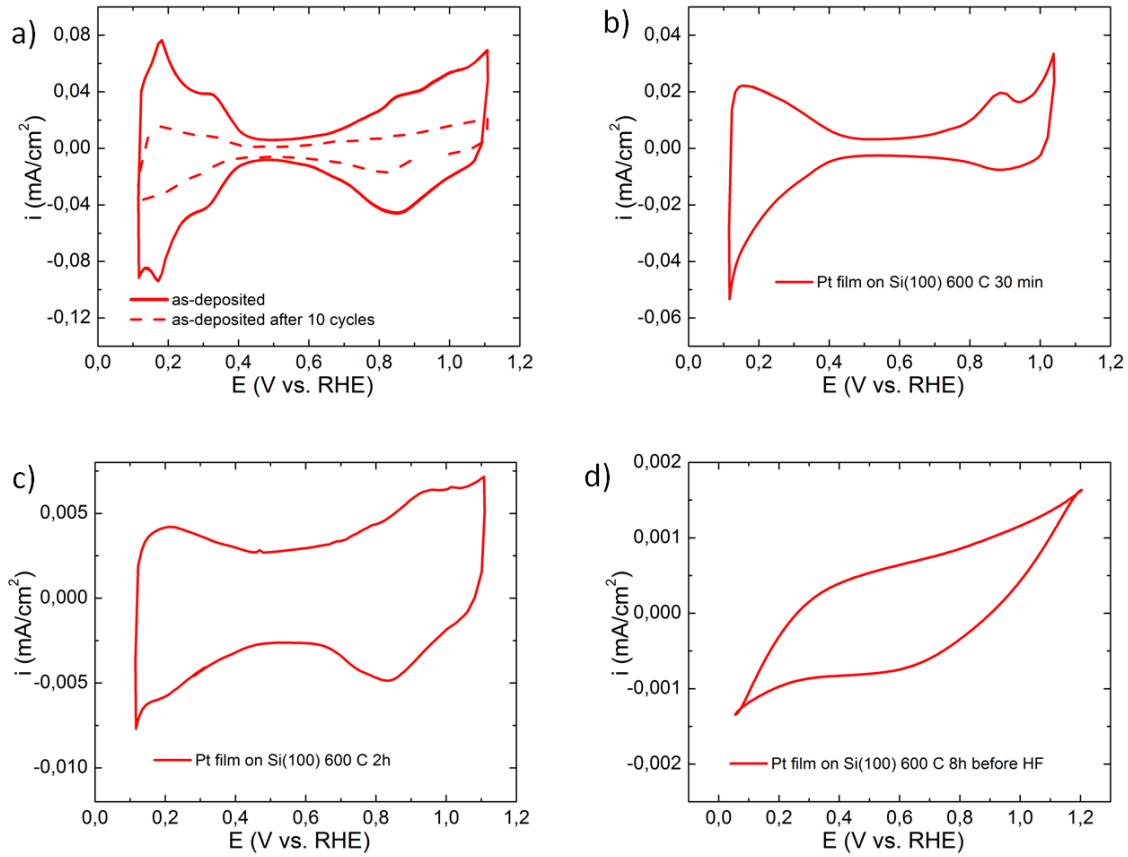

Figure 5.9: Hydrogen adsorption curves (HAD) for Pt film as-deposited - a) solid line, as-deposited after 10 CV cyles - a) dashed line; annealed at 600°C for 30 min - b); for 2 hours - c) and for 8 hours - d). Conducted in Ar-saturated 0.1 M $HClO_4$ with sweep rate 200 mV/s, measured at room temperature. Curves normalized to Pt ECSA.

Table 5.3 present geometric surface area and electrochemical surface area values for each catalyst.

The ECSA for all samples was calculated using the following equation:

$$ECSA(cm^2_{Pt}/cm^2) = \frac{q_{Pt}(mC)}{A(cm^2)0.210(mC/cm^2_{Pt})} \tag{5.1}$$

where A is the geometric area of the electrode (cm^2) and 0.210 is the charge it takes to oxidise one hydrogen monolayer on one centimetre square of Pt (single-crystal) in $mC/cm^2{}_{Pt}$.

The ECSA result show gradual a decrease with increased annealing time. The initial ECSA for Pt film on Si(100) was 0.0639 cm^2, for samples annealed at 600°C for 30 min ECSA was 0.003 cm^2, for 2 hours was 0.004 cm^2 and for 8 hours ECSA was 0.

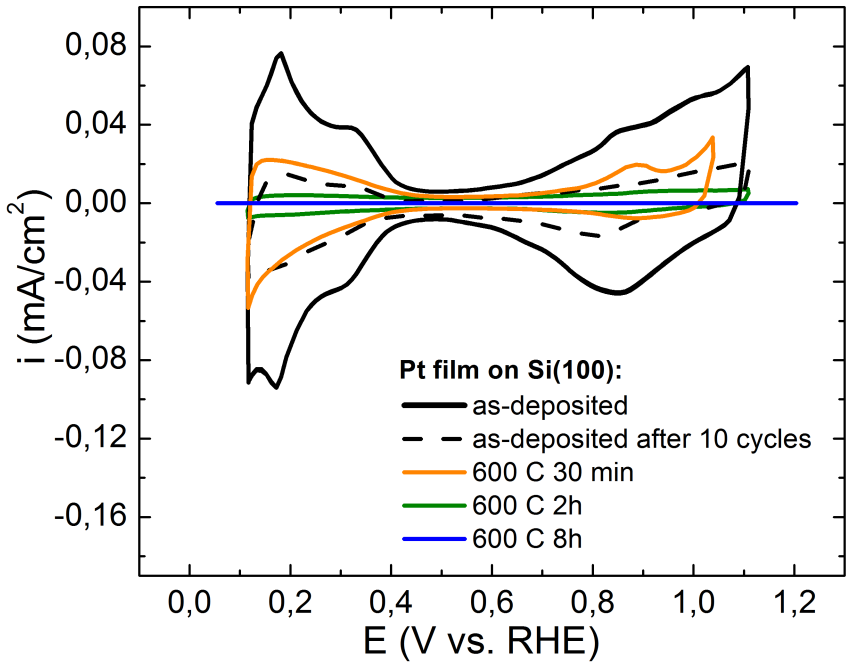

Figure 5.10: Comparison of the hydrogen adsorption curves for all catalysts in Ar-saturated 0.1 M $HClO_4$ with sweep rate 200 mV/s, measured at room temperature. Curves normalized to Pt ECSA.

In addition, Pt film as-deposited on Si(100) was seen to be unstable in the acid electrolyte and flaked off the Si(100) dramatically already after 10 cycles, resulting in ECSA decrease of 0.0204 cm^2 (Figure 5.9) (a), red dashed line). Heat treated samples however exhibited high stability under acid electrolyte conditions with ECSA unchanged after a number of cycles during all measurements. A comparison of cyclic voltammograms is given in Figure 5.10. Decreasing of ECSA could be hypothetically attributed to formation of silicon dioxide caused by reaction of Pt-Si alloy with the atmospheric oxygen. Overall ECSA results are in concurrence with XRD and Raman data analysis, whereby formation of the Pt-Si alloy is increasing gradually with increased annealing time.

5.4.4 Methanol electro-oxidation measurements

The electrocatalytic activity of Pt film on Si(100) as-deposited and samples annealed at 600°C for 30 min and 2 hours for methanol electro-oxidation activity in acid media is shown in Figures 5.11 and 5.12.

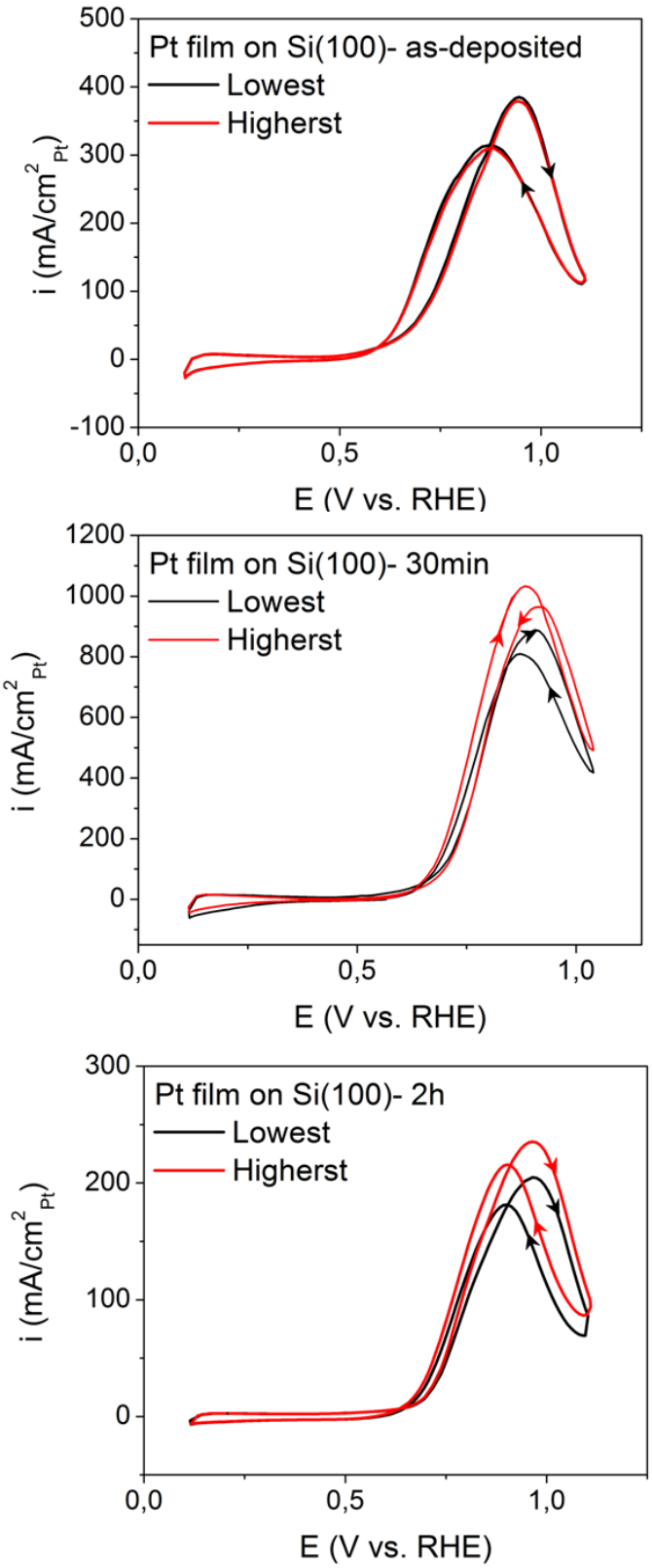

Figure 5.11: Original methanol electro-oxidation curves of Pt film on Si(100)as-deposited - a) and samples annealed at 600°C for 30 min - b) and 2 hours - c). Conducted in Ar-saturated 1 M CH_3OH in 0.1 M $HClO_4$ with sweep rate 200 mV/s, measured at room temperature. The black curves represent the lowest (first) oxidation loops, while the red represent the highest oxidation loops. Curves normalized to Pt ECSA.

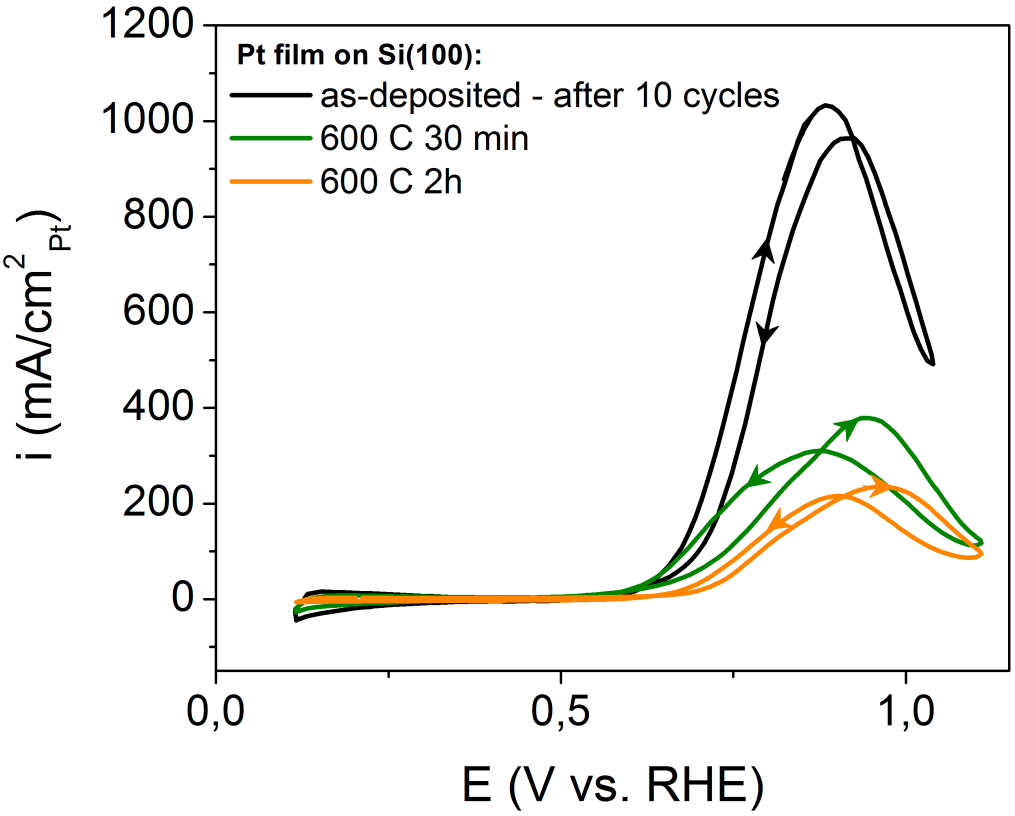

Figure 5.12: Comparison of original methanol electro-oxidation curves of Pt film on Si(100) as-deposited and annealed at 600°C for 30 min and 2 hours. Conducted in Ar-saturated 1 M CH_3OH in 0.1 M $HClO_4$ with sweep rate 200 mV/s, measured at room temperature and normalized to Pt ECSA.

Throughout the MOR measurements, MOR curves showed unsteady behaviour, but never went lower then the initial scan, therefore the lowest (first) scan (black curves) and the highest scan (red curves) presented for each catalyst as shown in Figures 5.11. Original methanol electro-oxidation curves were normalized to Pt ECSA.

The intrinsic activity of as-deposited Pt and PtSi films on Si(100) was observed to decrease with increased annealing time. In Figure 5.12, two characteristic irreversible current peaks were observed during the electro-oxidation of methanol for all investigated materials. It can be seen that the methanol electro-oxidation curves follow the general mechanism previously described; The peak obtained in the forward scan is typically attributed to the methanol electro-oxidation on Pt and the backward peak is known to be due to the oxidation reaction on the Pt of residual intermediate species such as CH_2OH, CH_2O, HCOOH and CO [4, 129, 131, 161].

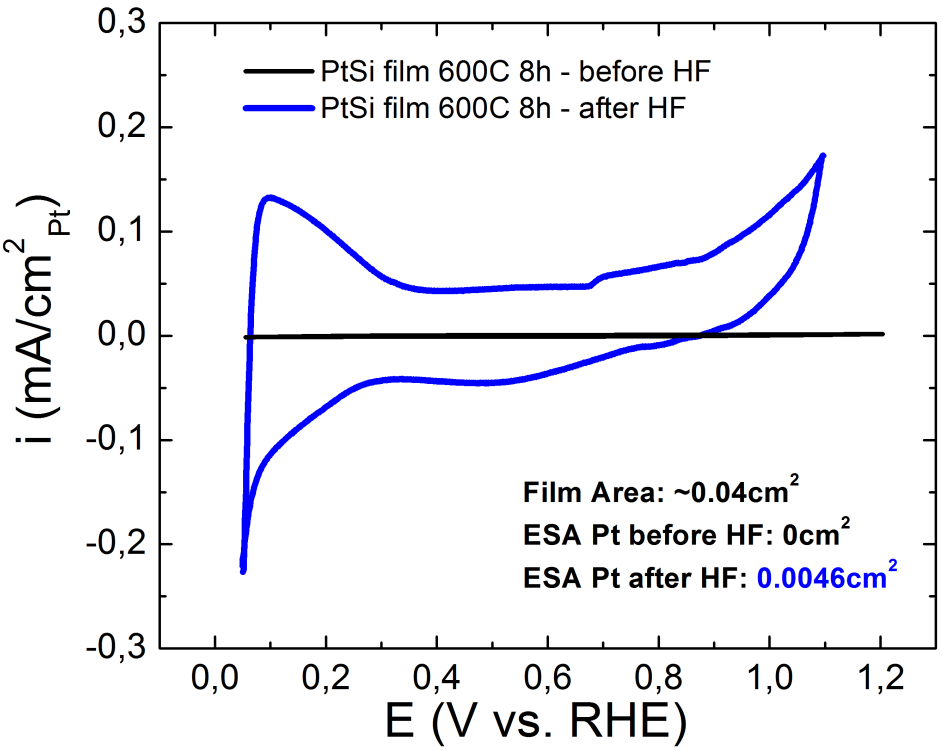

Figure 5.13: CVs for the PtSi thin film annealed at 600°C for 8 hours before (black line) and after (blue line) HF treatment. Conducted in Ar-saturated 0.1 M $HClO_4$, at 50 mV/s and room temperature.

Lowering of the MOR kinetics with increasing annealing times can be explained by formation of the silicon dioxide on the catalyst's surface, when more Si and less Pt getting exposed to the atmosphere oxygen (e.g. when more Pt-Si alloy is formed). This is similar in nature to the hydrogen adsorption ECSA results discussed previously, therefore it was decided to treat annealed samples in hydrofluoric acid (HF). HF treatment is a common method for dissolving silicon dioxide from the surface of materials.

5.4.5 Influence of hydrofluoric acid treatment on CV and MOR

Cyclic voltammetry

Figure 5.13 shows comparison of the cyclic voltammetry (CV) for the PtSi thin film annealed at 600°C for 8 hours and for the same film treated for 1 min in hydrofluoric (HF) acid. Experiments were conducted in Ar-saturated 0.1 M $HClO_4$ with sweep rate 50 mV/s, measured at room temperature and normalized to ECSA. The black line is the PtSi thin film alloyed sample before HF treatment and blue line, after HF treatment. It can be clearly seen that CV area increases dramatically after HF treatment. The shape of obtained CV for the HF treated sample show very similar behaviour to the PtRu alloys in acid solution, specifically, to the

PtRu alloy with ∼50 at.% Ru on the surface (as described by Gastaiger et al. [38]). In contrast to the typical Pt voltammogram with clearly defined hydrogen desorption/adsorption (H_{ad}/H_{des}) peaks (from ∼0 to ∼0.3 V vs. RHE), "hydrogen region" of PtRu alloys, does not allow simple potential-dependent distinction of these surface processes [38, 162, 163].

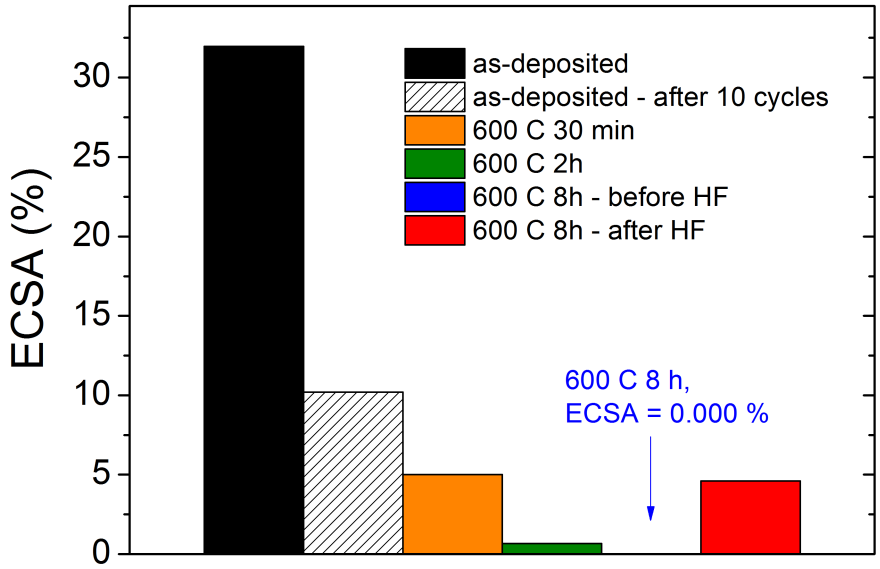

Figure 5.14: Comparison of ECSA (%) for Pt and Pt-Si alloy thin film catalysts before and after HF treatment.

In case of PtRu alloys the overlap of hydrogen desorption and oxide formation regions is caused by onset of the adsorption oxygen-like species at potentials as low as 0.2 V and coincides with the hydrogen desorption. As for the HF treated PtSi thin film, no typical H_{ad}/H_{des} peaks were observed as well. This finding can indicate similar mechanism of PtSi thin film alloy with PtRu alloys. However, this is an assumption and require further investigations. For the sake of comparison with non-HF treated samples, conjectural ECSA was calculated for the HF treated sample and shown obvious enlargement. It reached 0.0046 cm^2, whilst before the HF treatment it was 0.000 cm^2. A comparison of ECSA (%) for catalysts before and after HF treatment is presented in Figure 5.14, geometric surface area vs. electrochemical surface area data is summarised in Table 5.3. For reaching higher ECSAs, longer HF treatment times could be explored in future studies to further increase active surface sites by reducing silicon dioxide content on the surface.

Table 5.3: Comparison of annealing time, geometric area and electrochemical surface area (ECSA) for as deposited Pt film on Si(100) and catalysts annealed at 600°C and different times.

Samples annealed at 600°C	Area (GEO), cm^2	ECSA, cm^2
As-deposited/after 10 CV cycles	0.20/0.20	0.0639/0.0204
30 min	0.06	0.0030
2h	0.06	0.0004
8h - before HF	0.04	0.0000
8h - after HF	0.08	0.0046

Methanol electro-oxidation

In order to determine methanol electro-oxidation reaction (MOR) activity for HF treated PtSi film on Si(100) annealed at 600°C for 8 hours, samples CVs were measured in Ar-saturated 1 M CH_3OH in 0.1 M $HClO_4$ with sweep rate 50 mV/s at room temperature and normalized to Pt ECSA.

Figure 5.15 a) show the CV for the HF treated sample measured in 0.1 M $HClO_4$ (blue line) versus MOR (red line). This example indicate obvious evidence of methanol electro-oxidation on the PtSi thin film alloy after HF treatment. The shape of the MOR voltammogram obtained for the HF treated sample also show similar behaviour to the PtRu alloys in acid solution [38]), i.e. absence of the peaks typical for Pt MOR. HF treated PtSi film on Si(100) annealed at 600°C for 8 hours is shown in Figure 5.15, b) (i.e. the red line) and compared to MOR of Pt disk c) (i.e. black line). MOR of the HF treated sample does not exhibit higher peak current than Pt disk, but in terms of onset oxidation potential (usually the key parameter used to evaluate MOR electrocatalytic activity [4, 39, 129] it is shifted to the much lower potentials compare to one of the Pt disk.

In addition to the MOR activity, chronoamperometric curves were recorded at room temperature when the potential was stepped from 0.1 to 0.7 V vs. RHE in 1 M CH_3OH and 0.1 M $HClO_4$ in order to evaluate the catalyst deactivation process [130, 131], Figure 5.15, c). The currents values normalized to Pt ECSA. Here the red line represents the HF treated PtSi thin film alloy annealed at 600°C for 8 hours, while the black line represents the Pt disk data. Apparently, the HF treated PtSi thin film alloy exhibits rapid current density decay in the initial stages, likely being occupied by the poisoning intermediates during the electro-oxidation of methanol during the first 10 s. The Pt disk exhibits a similar decay over time, however the current density falls dramatically, indicating a lower tolerance to poisoning intermediates (a linearly bonded CO_{ad}). After 15 min of continuous polarization, the current density for the Pt disk is still decreasing.

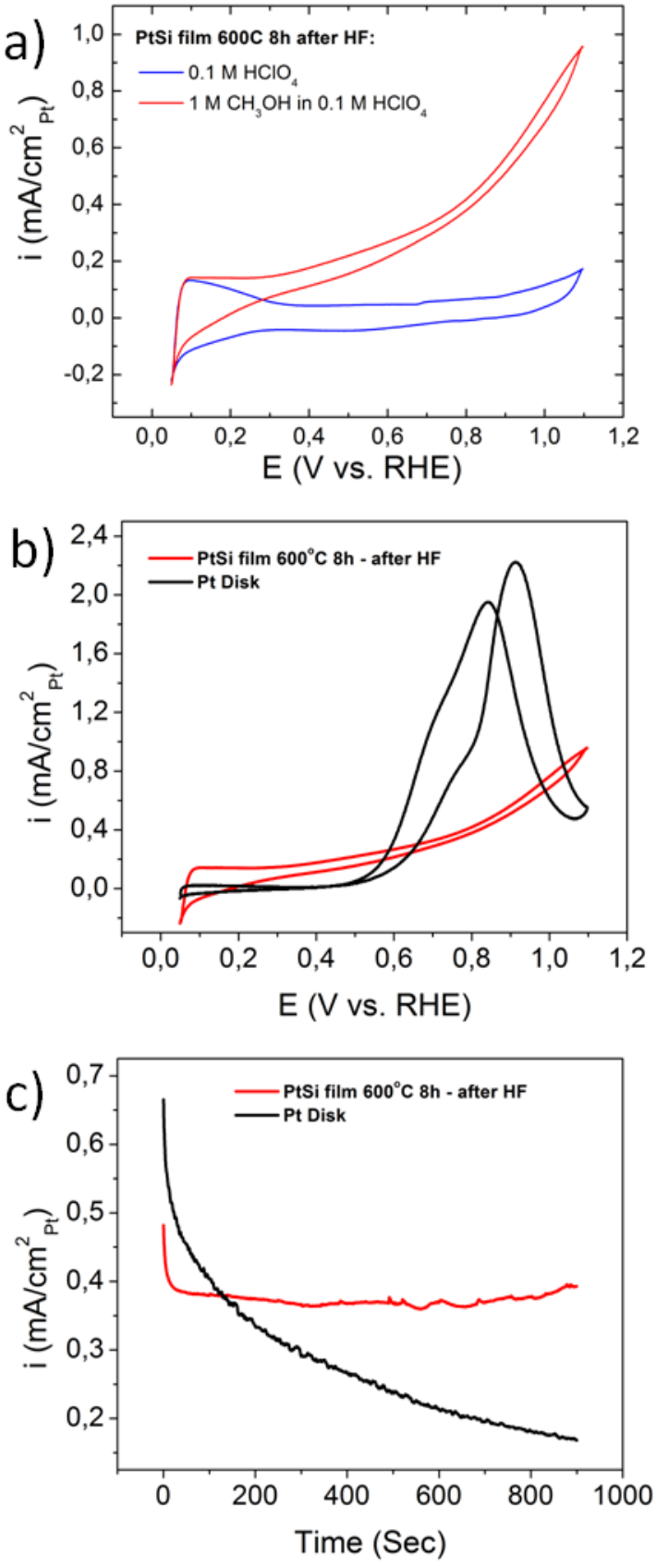

Figure 5.15: MOR for HF treated Pt-Si thin film on Si(100) annealed at 600°C for 8 hours. Conducted in Ar-saturated 1 M CH_3OH in 0.1 M $HClO_4$ with sweep rate 50 mV/s, measured at room temperature and normalized to Pt ECSA. a) CV in 0.1 M $HClO_4$ vs. MOR; b) MOR for the HF treated sample vs. Pt disk; c) Potentiostatic MOR current densities at 0.7 V; for b) and c) red line - HF treated sample and black line - Pt disk.

This is in contrast to the measured current density of HF treated PtSi thin film alloy which remains unchanged, indicating high stability toward the MOR. The final current density after 15 min polarisation for the Pt disk is about 0.1682 mA/cm^2, which is 2.4 times lower than that for HF treated PtSi thin film alloy (0.3929 mA/cm^2). This observation indicates PtSi thin film alloy on Si(100) annealed at 600°C for 8 hours could posses high resistance to poisoning during the methanol electo-oxidation in acidic media. However, this hypothesis requires further confirmation.

5.5 Conclusions and future work

Characterisation of a series of Pt and PtSi films on Si(100), heat treated at different temperatures or a fixed temperature (i.e. 600°C) and varying times was performed. Full conversion of Pt on Si(100) into PtSi alloy on Si(100) was observed after heat treatment at 600°C for 8 hours. Hydrogen adsorption exhibited a decreased ECSA in non-HF treated samples and a decrease in methanol oxidation activity. HF treated PtSi film on Si(100) annealed at 600°C for 8 hours showed a dramatic increase in ECSA compared to non-HF treated samples. This observation could be attributed to the dissolution of silicon dioxide from the alloy surface, however requires further confirmation by surface techniques such as X-ray photoelectron spectroscopy (XPS). After HF treatment, a PtSi alloy sample was compared to a Pt disk for MOR activity whereby it was observed that HF treated PtSi film alloy's onset oxidation potential shifted to much lower potentials in comparison to that of the Pt disk. Evaluation of the catalyst deactivation process by chronoamperometry for HF treated PtSi alloy film showed a 2.4 times higher resistance to poisoning for MOR in acid media in comparison to results obtained for the Pt disk. Moreover, the CV and MOR for the HF treated sample shown similar behaviour to the PtRu alloys in acidic solution [38, 39, 162, 163], that can hypothesize similar mechanism of reaction for Pt-Si thin film alloys. In summary, the results of this work are new and promising. However further experimental study is required in order to clarify the processes occurring before any firm conclusions can be made. This work will hopefully be completed in the near future.

Chapter 6

Conclusions and Perspectives

Conclusions

In the present thesis, tree main topics were highlighted:

In Chapter 3 the activity and durability of Pt nanoparticle PEM fuel cell electrocatalysts was investigated. Particularly, the effects of the support material were investigated, which further resulted in increased understanding of optimum design for improved catalysts. During the study a novel catalyst composed of Graphene-PBI supported platinum was synthesized and used for electrocatalytic reduction of oxygen. A comparison was made for ORR activity and cycling stability (ECSA) between Pt/Graphene-PBI, Pt/Graphene and commercial 40% Pt/Vulcan XC 72R electrocatalysts. Pt/Graphene-PBI catalyst exhibited activities in line with benchmark commercial fuel cell catalysts and showed a higher ORR activity and electrochemical surface area (ECSA) than the Pt/Graphene catalyst. A significant level of durability for the Pt/Graphene-PBI catalyst in comparison to the commercial alternative was also established. From the experimental correlations observed between particle size and distribution, ECSA and ORR activity change we can conclude that;

• The Pt/Graphene-PBI catalyst exhibited a more positive onset potential hence shows a higher ORR catalytic activity than observed for the Pt/Graphene catalyst at 0.85 V vs. RHE

• The observed increase in ORR activity for Pt/Graphene-PBI compare to Pt/Graphene is likely caused by the advantages inherent in the Graphene-PBI support. The XRD and TEM studies showed that by applying PBI onto Graphene platinum the nanoparticle size reduced significantly compare to the Pt catalyst with graphene as a support only. The introduction of a PBI coating aided more even deposition of Pt on the surface, an effect clearly seen in

the acquired TEM images. In addition, Pt (wt.%) loading on the support was increased from 32.5 wt.% to 37 wt.% when BPI wrapping was applied as revealed by TGA results

• ECSA of the 40% Pt/Vuclan XC 72R commercial catalyst is higher prior to potential cycling than for Pt/Graphene and Pt/Graphene-PBI catalsts. However the 40% Pt/Vuclan XC 72R exhibited a significant drop in ECSA compared to the two other catalysts after potential cycling

• ECSA's for the Pt/Graphene-PBI nanoparticle catalysts are higher than those for Pt/Graphene and those of 40% Pt/Vuclan XC 72R after voltage cycling testing. ECSA of Pt/Graphene-PBI stayed almost unchanged, while Pt/Graphene ECSA is decreased after potential cycling regime

The resultant ORR and ECSA for Pt/Graphene-PBI catalyst could potentially be explained by the following factors. First, the increase in ORR can be explained by a change in Pt nanoparticle size, whereby PBI induces improved nucliation of Pt nanoparticles onto the inert graphene surfaces, subsequently aiding better Pt nanopartcle distribution. Secondly, the thin shell of PBI offers additional protection against graphene corrosion without sacrificing the electric conductivity of the existing graphene support and preventing damage of the support giving higher stability. The approach creates a catalyst which is more active than Pt/Graphene for ORR which is also highly durable in comparison to Pt/Graphene and commercial 40% Pt/Vuclan XC 72R. Therefore, this study suggests that Graphene-PBI supports are viable fuel cell catalyst supports.

In Chapter 4 the activity of catalysts towards carbon monoxide and methanol electro-oxidation for DMEFC was investigated for DMEFCs anodes. This was achieved by alloying Pt with other non-metal elements such as silicon. A novel Pt-Si catalysts was investigated and the mechanism of catalysis for carbon monoxide and methanol electro-oxidation reaction was proposed.

• Characterization of a series of Pt-Si alloys for CO and methanol electro-oxidation was performed for the first time.

• Both the onset and peak oxidation potentials shifted to lower potentials for CO electro-oxidation.

• The onset potentials for MOR shifted to lower potentials.

• The intrinsic electro-oxidation activity for adsorbed CO on Pt-Si alloys increased with Si concentrations.

• A Langmuir-Hinshelwood reaction type was proposed and attributed to preferential adsorption of oxygenated species on Si sites, promoting faster oxidation of CO adsorbed on Pt sites.

Thus, the enhanced activity of CO and methanol electro-oxidation implies Pt-Si alloys could be a potential highly active catalyst for fuel cells operating with CO and small molecular organic fuels. Moreover, the limited solubility of Si in acidic media may lead to higher stability than other Pt-M analogues.

In Chapter 5 the potential of newly designed Pt-Si thin film alloy catalyst for the methanol electro-oxidation was investigated aided by the findings presented in Chapter 4, where bulk Pt-Si alloys exhibit higher carbon monoxide and methanol electro-oxidation activities in an acid electrolyte. Alloying of the ALD deposited Pt thin film with Si(100) support was explored. Consequently ways of preparing Pt-Si alloy thin films were explored including methods for physical characterization and to attain starting electrochemical measurements. It was hypothesized that Pt-Si films supported on a Si (100) substrate potentially possess similar properties to PtRu alloys towards the methanol electro-oxidation.

• Characterisation of a series of Pt film and PtSi film on Si(100) heat treated at varying temperature and for a fixed temperature (600°C) and varying times was performed. This investigation found a full conversion of Pt on Si(100) into PtSi alloy on Si(100) was observed after heat treatment at 600°C for 8 hours.

• Hydrogen adsorption was seen to decrease ECSA in non-HF treated samples and decrease overall methanol oxidation activity.

• HF treated PtSi film on Si(100) annealed at 600°C for 8 hours showed a dramatic increase of ECSA in comparison to non-HF treated samples in addition to an increase in MOR activity. This was suggested to be a result of dissolution of silicon dioxide from the alloy surface, however this requires additional confirmation by surface techniques (e.g. X-ray photoelectron spectroscopy).

• HF treated PtSi alloy samples were subsequently compared to a Pt disk for MOR activity whereby it was observed that the onset oxidation potential for HF treated PtSi film alloy is shifted to much lower potentials in comparison to the Pt disk.

• Evaluation of the catalyst deactivation process using chronoamperometry at 0.7 V vs. RHE in 1 M CH_3OH and 0.1 M $HClO_4$ for HF treated PtSi alloy film showed a 2.4 times higher resistance to poisoning for MOR in acid media compare to the Pt disk.

Therefore the results of this work show significant promise for a new material to be developed for catalysis of methanol electro-oxidation in miniature methanol fuel cells. It

should be noted however that further investigation is needed in order to fully characterise and assess the processes occurring.

Perspectives

The development of more active and stable catalysts including suitable supports for ORR, CO and methanol electro-oxidation reactions remains a crucial research goal in order to improve PEMFC efficiency. Currently, Pt-based catalysts in conjunction with carbon-based supports are the commonly employed catalyst for these reactions. The work described in this thesis suggests that the future perspectives and challenges for further improvement of PEM, DME and miniature DME fuel cell catalysts are;

• The design and construction of corrosion resistant supporting materials with high conductivity and minimal surface defects. This could be achieved by polymer wrapping which allows; homogeneous dispersion of catalyst nanoparticles, reduction in catalyst's particle size, prevention of catalyst sintering and prevention of dissolution and migration during lifetime voltage tests. For example, development of Pt nanoparticles deposited onto PBI wrapped Graphene was shown as a possible approach for engineering a more durable form of Pt electrocatalyst for ORR than the current Pt/C.

• The transfer of Pt/Graphene-PBI catalyst results established by RDE studies to a single MEA and stack scale-up, to test under typical PEMFCs conditions. Consequently the design of a gas diffusion electrode then will be a challenge.

• Identification of an optimal catalyst composition for high stability and activity using model experiments on bulk, thin films and size selected nanoparticles for Pt-Si alloys.

• Transfer of CO and methanol electro-oxidation results of a model bulk and thin film Pt-Si alloy to the nano-scale. Furthermore the design of a chemical synthesis process to fabricate nanoparticle catalysts with potential scale up to production level would then be required.

• Conventional aqueous synthesis routes are currently unable to form nanoparticles for Pt- Si alloys due to the insolubility of Si. Therefore, other methods should be studied such as; cathodic corrosion of bulk Pt alloys, metalorganic synthesis routes and/or magnetron cluster source for production of mass selected model nanoparticles.

• The complete investigation of Pt-Si thin film alloys on Si (100) should be undertaken and eventually a comprehensive study investigating its properties as an electrode by itself in miniature DMEFCs.

• The investigation of catalysts presently employed for other currently electro-chemical reactions. For example; formic acid, dimethyl ether eloectro-oxidation activity or hydrogen electro-oxidation reaction (HOR) in alkaline membrane fuel cells (AMFC's), where recently extended surfaces of polycrystalline Pt-Ru exhibit a 6-fold activity improvement over pure Pt [164]. Similar properties could apply to the PtSi alloys.

Chapter 7

Appendixes

7.1 Apendix A

CO and methanol electro-oxidation vs. surface Si concentration from XPS for Pt-Si alloys in 0.1 M $HClO_4$ at 5 mV/s at 0.7 V vs. RHE., Figure 7.1 and 7.2, respectively.

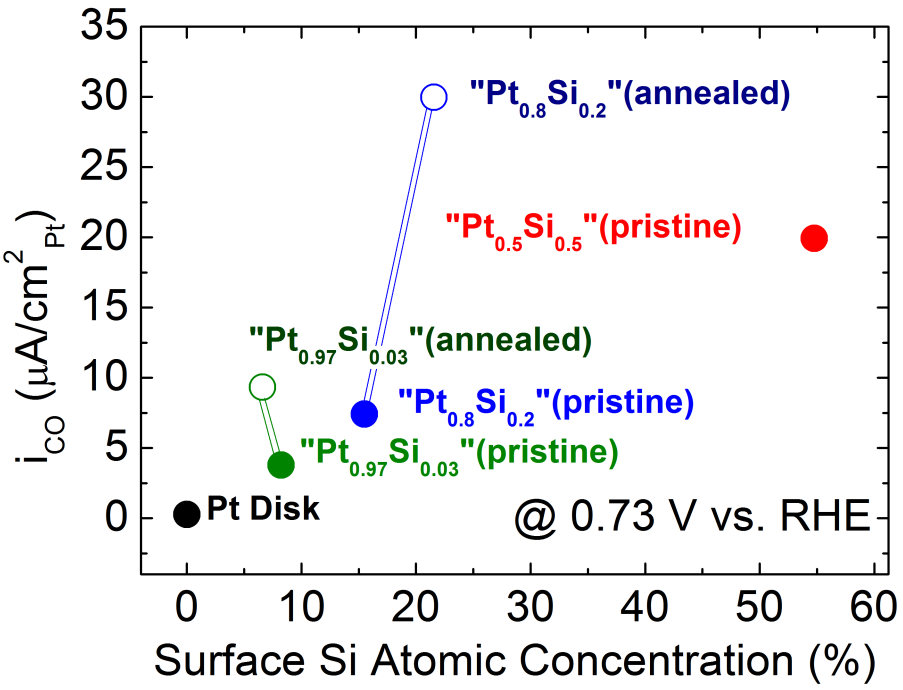

Figure 7.1: CO electro-oxidation vs. surface Si concentration from XPS for Pt-Si alloys in 0.1 M $HClO_4$ at 5 mV/s at 0.7 V vs. RHE..

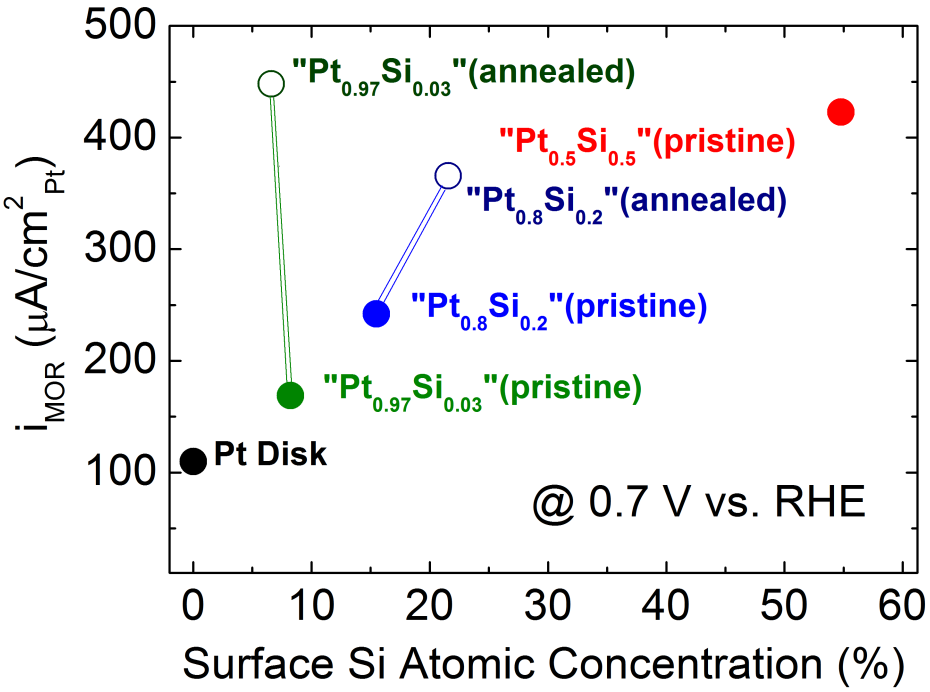

Figure 7.2: Methanol electro-oxidation vs. surface Si concentration from XPS for Pt-Si alloys in 0.1 M $HClO_4$ at 50 mV/s at 0.7 V vs. RHE.

7.2 Apendix B

Atomic force microscopy (AFM) images of ALD deposited Pt and Pt-Si thin films on Si (100). 2D AFM images - Figure 7.3 and 3D AFM images - Figure7.4.

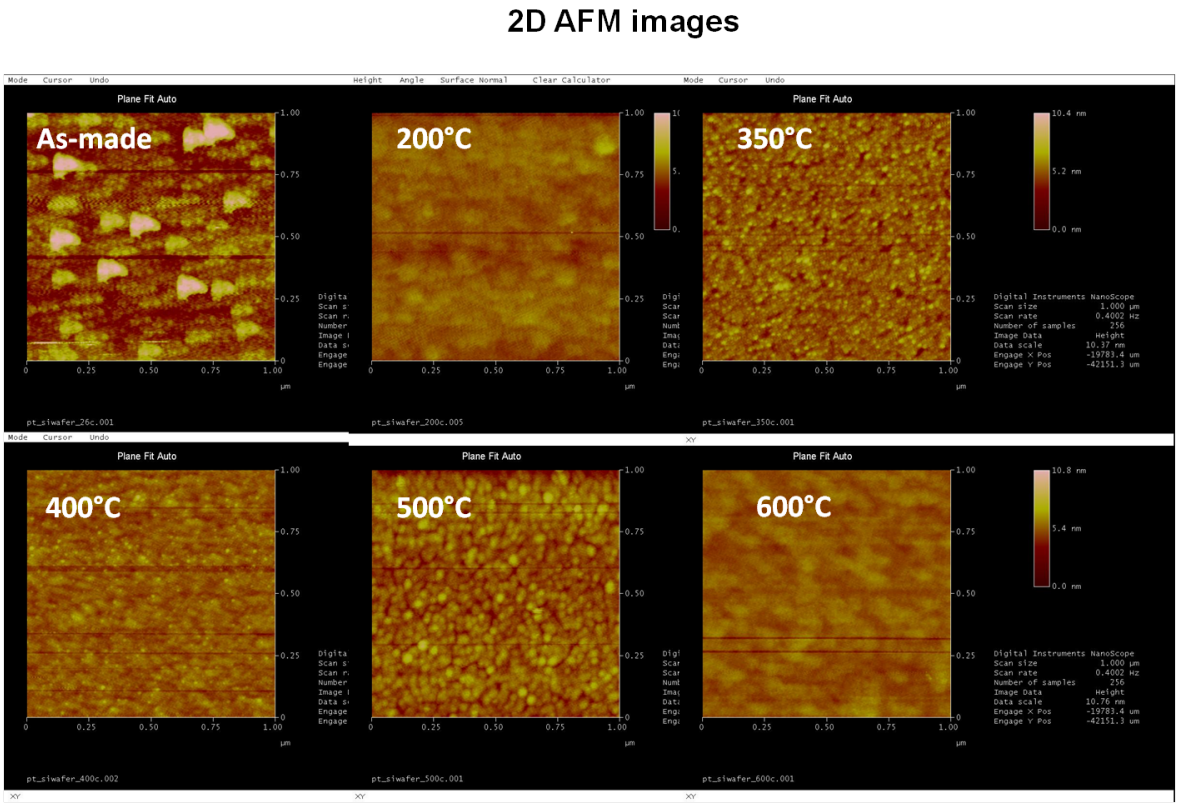

Figure 7.3: 2D AFM images of thin film samples as-deposited by ALD and heat treated by method A: 30 min for 200°C, 350°C, 400°C, 500°C and 600°C

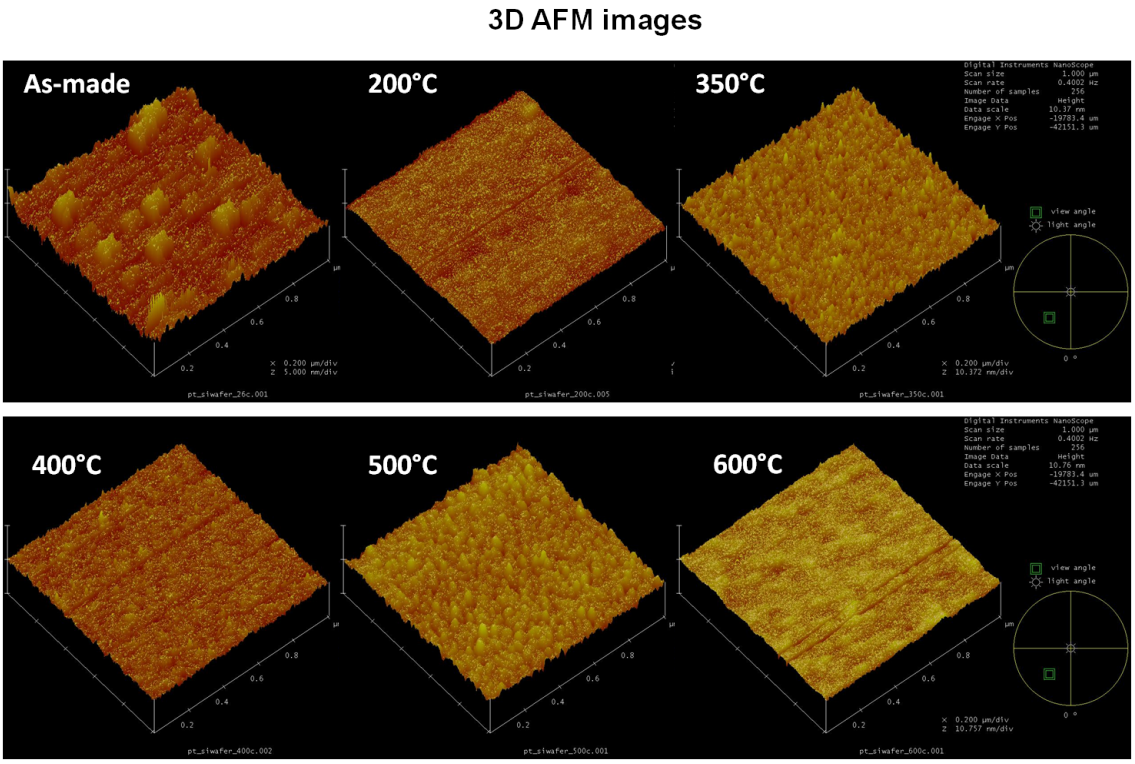

Figure 7.4: 3D AFM images of thin film samples as-deposited by ALD and heat treated by method A: 30 min for 200°C, 350°C, 400°C, 500°C and 600°C

Bibliography

[1] ExxonMobil, "2010 the out look for energy: A view to 2030," 2010.

[2] "European commission. high level group. hydrogen energy and fuel cells - a vision of our future," 2003.

[3] H. Wang, C. Wingender, H. Baltruschat, M. Lopez, and M. Reetz, "Methanol oxidation on Pt, PtRu, and colloidal Pt electrocatalysts: a DEMS study of product formation," *Journal of Electroanalytical Chemistry*, vol. 509, no. 2, pp. 163–169, 2001.

[4] H. S. Wroblowa, Yen-Chi-Pan, and G. Razumney, "Electroreduction of oxygen a new mechanistic criterion," *Journal of Electroanalytical Chemistry*, vol. 69, no. 2, pp. 195–201, 1976.

[5] E. Yeager, "Mechanisms of Electrochemical Reactions on Non-Metallic Surfaces," *NBS Special Publication*, 1976.

[6] H. Okamoto, "Pt - Si (Platinum-Silicon)," *Journal of Phase Equilibria and Diffusion*, vol. 32, no. 4, pp. 394–395, 2011.

[7] P. P. Edwards, V. L. Kuznetsov, W. I. F. David, and N. P. Brandon, "Hydrogen and fuel cells: Towards a sustainable energy future," *Energy Policy*, 2008.

[8] J. Larminie and A. Dicks, *Fuel cell systems explained*. Wiley, second ed., 2003.

[9] H. L. Maynard and J. P. Meyers, "Miniature fuel cells for portable power: Design considerations and challenges," *Journal of Vacuum Science & Technology B: Microelectronics and Nanometer Structures*, vol. 20, no. 4, pp. 1287–1297, 2002.

[10] ExxonMobil, "2012 the outlook for energy: A view to 2040," 2012.

[11] C. . C. C. Project, "Total man-made emissions," 2008.

[12] I. Dincer, "Hydrogen and fuel cell technologies for sustainable future," *Jordan Journal of Mechanical and Industrial Engineering*, 2008.

[13] A. B. Stambouli and E. Traversa, "Fuel cells, an alternative to standard sources of energy," *Renewable and Sustainable Energy Reviews*, 2001.

[14] R. O'Hayre, S.-W. Cha, W. Colella, and F. B. Prinz, *Fuel Cell Fundamentals, 2nd Edition*. John Wiley & Sons, Inc., 2009.

[15] S. Thomas and M. Zalbowitz, "Fuel cells - green power," *Los Alamos National Laboratory*, 2006.

[16] S. M. J. Zaidi and M. A. Rauf, *Polymer Membranes for Fuel Cells: Fuel Cell Fundamentals*. Springer-Verlag US, 2009.

[17] W. R. Grove *Philosophical Magazine*, vol. 14, 1839.

[18] M. L. Mond and C. Langer, "A new form of gas battery," *The Royal Society of London*, 1889.

[19] W. Vielstich, A. Lamm, and H. A. Gasteiger, eds., *Handbook of Fuel Cells: Fundamentals, Technologies and Applications. Fundamentals and Survey of Systems*, vol. 1. John Wiley & Sons Ltd, 2003.

[20] J. O. Jensen and Q. Li, *Hydrogen Technology. Chapter 5: Fuel Cells*. Springer-Verlag Berlin Heidelberg, 2008.

[21] L. R. F. Allen J. Bard, *Elecreochemical Methods. Fundamentals and Applications*. John Wiley & Sons, 2001.

[22] N. L. W. Grubb W. T. *J. Electrochem. Soc.*, vol. 107, pp. 131–135, 1960.

[23] B. K. A. Hamnett, "Bimetallic carbon supported anodes for the direct methanol-air fuel cell," *Electrochim. Acta*, vol. 33, p. 1613, 1988.

[24] J. S. Wainright, J. T. Wang, D. Weng, R. F. Savinell, and L. M., "Acid-Doped Polybenzimidazoles: A New Polymer Electrolyte," *J. E*, vol. 142, pp. L121–L123, 1995.

[25] Q. Li, R. He, J. O. Jensen, and B. N. J., "PBI - Based Polymer Membranes for High Temperature Fuel Cells Preparation, Characterization and Fuel Cell Demonstration," *Fuel Cells*, vol. 4, pp. 147–159, 2004.

[26] Q. Li, J. O. Jensen, R. F. Savinell, and N. J. Bjerrum, "High temperature proton exchange membranes based on polybenzimidazoles for fuel cells," *Progress in Polymer Science*, vol. 34, pp. 449–477, 2009.

[27] J. O. Jensen, Q. Li, C. Pan, A. P. Vestb, K. Mortensen, H. N. Petersen, C. L. Srensen, T. N. Clausen, J. Schramm, and B. N. J., "High temperature PEMFC and the possible utilization of the excess heat for fuel processing," *International J. Hydrogen Energy*, vol. 32, pp. 1567–1571, 2007.

[28] Q. Li, R. He, J. O. Jensen, and B. N. J., "CO tolerance by the PEMFC operational at temperatures up to 200C," *J. Electrochem. Soc.*, vol. 150, pp. A1599–A1605, 2003.

[29] L. Qingfeng, H. A. Hjuler, C. Hasiotis, J. K. Kallitsis, C. G. Kontoyannis, and N. J. Bjerrum, "A quasi-direct methanol fuel cell system based on blend polymer membrane electrolytes," *Eletrochem. Solid-State Lett.*, vol. 5, pp. A125–A128, 2002.

[30] C. H. Hamann, A. Hamnett, and W. Vielstich, *Electrochemistry*. Wiley-VCH, Weinheim, second ed., 2007.

[31] X. Li, *Principles of fuel cells*. Taylor & Francis Group, LLC, 2006.

[32] W. Vielstich, A. Lamm, and H. A. Gasteiger, eds., *Handbook of Fuel Cells. Fundamentals, Technology and Applications. Electrocatalysis*, vol. 2. John Wiley & Sons Ltd, 2003.

[33] K. C. Neyerlin, W. Gu, J. Jorne, and H. A. Gasteiger, "Study of the Exchange Current Density for the Hydrogen Oxidation and Evolution Reactions," *Journal of The Electrochemical Society*, vol. 154, no. 7, pp. B631–B635, 2007.

[34] W. Sheng, H. A. Gasteiger, and Y. Shao-Horn, "Hydrogen Oxidation and Evolution Reaction Kinetics on Platinum: Acid vs Alkaline Electrolytes," *Journal of The Electrochemical Society*, vol. 157, no. 11, pp. B1529–B1536, 2010.

[35] V. S. Bagotzky and Y. B. Vassiliev, "Absorption of organic substances on platinum electrodes," *Electrochimica Acta*, vol. 11, no. 10, pp. 1439 – 1461, 1966.

[36] V. E. Kazarinov, G. Y. Tysyachnaya, and V. N. Andreev, "On the reasons for the discrepancies in the data on methanol adsorption on platinum," *Journal of Electroanalytical Chemistry and Interfacial Electrochemistry*, vol. 65, no. 1, pp. 391 – 400, 1975.

[37] B. A. Sexton, "Methanol decomposition on platinum (111)," *Surface Science*, vol. 102, no. 1, pp. 271 – 281, 1981.

[38] H. A. Gasteiger, N. Markovic, P. N. Ross, and E. J. Cairns, "Methanol electrooxidation on well-characterized platinum-ruthenium bulk alloys," *The Journal of Physical Chemistry*, vol. 97, no. 46, pp. 12020–12029, 1993.

[39] N. M. Markovic, H. A. Gasteiger, P. N. R. Jr, X. Jiang, I. Villegas, and M. J. Weaver, "Electro-oxidation mechanisms of methanol and formic acid on Pt-Ru alloy surfaces," *Electrochimica Acta*, vol. 40, no. 1, pp. 91 – 98, 1995.

[40] S. W. Lee, S. Chen, J. Suntivich, K. Sasaki, R. R. Adzic, and Y. Shao-Horn, "Role of Surface Steps of Pt Nanoparticles on the Electrochemical Activity for Oxygen Reduction," *The Journal of Physical Chemistry Letters*, vol. 1, no. 9, pp. 1316–1320, 2010.

[41] F. J. E. Scheijen, G. L. Beltramo, S. Hoeppener, T. H. M. Housmans, and M. T. M. Koper, "The electrooxidation of small organic molecules on platinum nanoparticles supported on gold: influence of platinum deposition procedure," *Journal of Solid State Electrochemistry*, vol. 12, pp. 483–495, 2008.

[42] P. Olivi, L. Bulhões, J.-M. Léger, F. Hahn, B. Beden, and C. Lamy, "The electrooxidation of formaldehyde on Pt(100) and Pt(110) electrodes in perchloric acid solutions," *Electrochimica Acta*, vol. 41, no. 6, pp. 927 – 932, 1996.

[43] W. Gao, J. A. Keith, J. Anton, and T. Jacob, "Theoretical Elucidation of the Competitive Electro-oxidation Mechanisms of Formic Acid on Pt(111)," *Journal of the American Chemical Society*, vol. 132, no. 51, pp. 18377–18385, 2010.

[44] H. Ekstrom, *Evaluating Cathode Catalysts in the PEM FC*. 2007.

[45] J. O. Bockris and S. U. M. Khan, *Surface Electrochemistry: A Molecular Level Approach*. Springer, 1993.

[46] S. Gilman, "The Mechanism of Electrochemical Oxidation of Carbon Monoxide and Methanol on Platinum. II. The "Reactant-Pair" Mechanism for Electrochemical Oxidation of Carbon Monoxide and Methanol," *The Journal of Physical Chemistry*, vol. 68, no. 1, pp. 70–80, 1964.

[47] N. P. Lebedeva, A. Rodes, J. M. Feliu, M. T. M. Koper, and R. A. van Santen, "Role of Crystalline Defects in Electrocatalysis: CO Adsorption and Oxidation on Stepped Platinum Electrodes As Studied by in situ Infrared Spectroscopy," *The Journal of Physical Chemistry B*, vol. 106, no. 38, pp. 9863–9872, 2002.

[48] E. Santos, E. P. M. Leiva, and W. Vielstich, "CO adsorbate on Pt(111) single crystal surfaces," *Electrochimica Acta*, vol. 36, no. 3–4, pp. 555 – 561, 1991.

[49] E. Herrero, J. M. Feliu, S. Blais, Z. Radovic-Hrapovic, and G. Jerkiewicz, "Temperature Dependence of CO Chemisorption and Its Oxidative Desorption on the Pt(111) Electrode," *Langmuir*, vol. 16, no. 11, pp. 4779–4783, 2000.

[50] V. R. Stamenkovic, B. Fowler, B. S. Mun, G. Wang, P. N. Ross, C. A. Lucas, and N. M. Markovic, "Improved Oxygen Reduction Activity on $Pt_3Ni(111)$ via Increased Surface Site Availability," *Science*, vol. 315, no. 5811, pp. 493–497, 2007.

[51] T. F. Jaramillo, K. P. Jørgensen, J. Bonde, J. H. Nielsen, S. Horch, and I. Chorkendorff, "Identification of Active Edge Sites for Electrochemical H_2 Evolution from MoS_2 Nanocatalysts," *Science*, vol. 317, no. 5834, pp. 100–102, 2007.

[52] H. A. Gasteiger, N. M. Markovic, and P. N. Ross, "H_2 and CO Electrooxidation on Well-Characterized Pt, Ru, and Pt-Ru. 1. Rotating Disk Electrode Studies of the Pure Gases Including Temperature Effects," *The Journal of Physical Chemistry*, vol. 99, no. 20, pp. 8290–8301, 1995.

[53] Y. Morimoto and E. B. Yeager, "CO oxidation on smooth and high area Pt, Pt-Ru and Pt-Sn electrodes," *Journal of Electroanalytical Chemistry*, vol. 441, pp. 77–81, 1998.

[54] L. dos Santos, F. Colmati, and E. R. Gonzalez, "Preparation and characterization of supported Pt–Ru catalysts with a high Ru content," *Journal of Power Sources*, vol. 159, no. 2, pp. 869 – 877, 2006.

[55] C. Dupont, Y. Jugnet, and D. Loffreda, "Theoretical evidence of PtSn alloy efficiency for CO oxidation," *Journal of the American Chemical Society*, vol. 128, pp. 9129–36, July 2006.

[56] Z. Liu, B. Guo, L. Hong, and T. H. Lim, "Microwave heated polyol synthesis of carbon-supported PtSn nanoparticles for methanol electrooxidation," *Electrochemistry Communications*, vol. 8, pp. 83–90, Jan. 2006.

[57] T. Kawaguchi, Y. Rachi, W. Sugimoto, Y. Murakami, and Y. Takasu, "Performance of ternary PtRuRh/C electrocatalyst with varying Pt:Ru:Rh ratio for methanol electro-oxidation," *Journal of Applied Electrochemistry*, vol. 36, pp. 1117–1125, 2006.

[58] Y. S. Kim, S. H. Nam, H.-S. Shim, H.-J. Ahn, M. Anand, and W. B. Kim, "Electrospun bimetallic nanowires of PtRh and PtRu with compositional variation for methanol electrooxidation," *Electrochemistry Communications*, vol. 10, no. 7, pp. 1016 – 1019, 2008.

[59] S. Mukerjee, R. C. Urian, S. J. Lee, E. A. Ticianelli, and J. McBreen, "Electrocatalysis of CO Tolerance by Carbon-Supported PtMo Electrocatalysts in PEMFCs," *Journal of The Electrochemical Society*, vol. 151, no. 7, pp. A1094–A1103, 2004.

[60] B. Gurau, R. Viswanathan, R. Liu, T. J. Lafrenz, K. L. Ley, E. S. Smotkin, E. Reddington, A. Sapienza, B. C. Chan, T. E. Mallouk, and S. Sarangapani, "Structural and Electrochemical Characterization of Binary, Ternary, and Quaternary Platinum Alloy Catalysts for Methanol Electro-oxidation," *The Journal of Physical Chemistry B*, vol. 102, no. 49, pp. 9997–10003, 1998.

[61] N. M. Markovic, T. J. Schmidt, V. Stamenkovic, and P. N. Ross, "Oxygen Reduction Reaction on Pt and Pt Bimetallic Surfaces: A Selective Review," *Fuel Cells*, vol. 1, no. 2, pp. 105–116, 2001.

[62] N. Markovic, H. Gasteiger, and P. N. Ross, "Kinetics of Oxygen Reduction on Pt(hkl) Electrodes: Implications for the Crystallite Size Effect with Supported Pt Electrocatalysts," *Journal of The Electrochemical Society*, vol. 144, no. 5, pp. 1591–1597, 1997.

[63] H. A. Gasteiger, S. S. Kocha, B. Sompalli, and F. T. Wagner, "Activity benchmarks and requirements for Pt, Pt-alloy, and non-Pt oxygen reduction catalysts for PEMFCs," *Applied Catalysis B: Environmental*, vol. 56, pp. 9–35, Mar. 2005.

[64] J. Greeley, I. E. L. Stephens, A. S. Bondarenko, T. P. Johansson, H. A. Hansen, T. F. Jaramillo, J. J. Rossmeisl, I. CRossmeisl, and J. K. Nrskov, "Alloys of platinum and early transition metals as oxygen reduction electrocatalysts," *Nature Chemistry*, vol. 1, pp. 552–556, Oct. 2009.

[65] S. Koh and P. Strasser, "Electrocatalysis on Bimetallic Surfaces: Modifying Catalytic Reactivity for Oxygen Reduction by Voltammetric Surface Dealloying," *Journal of the American Chemical Society*, vol. 129, no. 42, pp. 12624–12625, 2007.

[66] S. Chen, W. Sheng, N. Yabuuchi, P. J. Ferreira, L. F. Allard, and Y. Shao-Horn, "Origin of Oxygen Reduction Reaction Activity on Pt_3Co Nanoparticles Atomically Resolved Chemical Compositions and Structures," *The Journal of Physical Chemistry C*, vol. 113, no. 3, pp. 1109–1125, 2009.

[67] M. Escudero-Escribano, A. Verdaguer-Casadevall, P. Malacrida, U. Grnbjerg, B. P. Knudsen, A. K. Jepsen, J. Rossmeisl, I. E. L. Stephens, and I. Chorkendorff, "Pt5Gd as a Highly Active and Stable Catalyst for Oxygen Electroreduction," *Journal of the American Chemical Society*, vol. 134, no. 40, pp. 16476–16479, 2012.

[68] M. Wakisaka, H. Suzuki, S. Mitsui, H. Uchida, and M. Watanabe, "Increased Oxygen Coverage at Pt-Fe Alloy Cathode for the Enhanced Oxygen Reduction Reaction Studied by EC-XPS," *J. Phys. Chem. C*, vol. 112, pp. 2750–2755, Jan. 2008.

[69] U. A. Paulus, A. Wokaun, G. G. Scherer, T. J. Schmidt, V. Stamenkovic, V. Radmilovic, N. M. Markovic, and P. N. Ross, "Oxygen Reduction on Carbon-Supported Pt-Ni and Pt-Co Alloy Catalysts," *The Journal of Physical Chemistry B*, vol. 106, no. 16, pp. 4181–4191, 2002.

[70] K. J. J. Mayrhofer, V. Juhart, K. Hartl, M. Hanzlik, and M. Arenz, "Adsorbate-Induced Surface Segregation for Core-Shell Nanocatalysts," *Angewandte Chemie International Edition*, vol. 48, no. 19, pp. 3529–3531, 2009.

[71] H. A. Gasteiger and N. M. Markovic, "Just a Dream - or Future Reality?," *Science*, vol. 324, no. 5923, pp. 48–49, 2009.

[72] V. R. Stamenkovic, B. S. Mun, K. J. J. Mayrhofer, P. N. Ross, and N. M. Markovic, "Effect of Surface Composition on Electronic Structure, Stability, and Electrocatalytic Properties of Pt-Transition Metal Alloys: Pt-Skin versus Pt-Skeleton Surfaces," *J. Am. Chem. Soc.*, vol. 128, pp. 8813–8819, June 2006.

[73] I. E. L. Stephens, A. S. Bondarenko, U. Gronbjerg, J. Rossmeisl, and I. Chorkendorff, "Understanding the electrocatalysis of oxygen reduction on platinum and its alloys," *Energy Environ. Sci.*, vol. 5, no. 5, pp. 6744–6762, 2012.

[74] S. J. Yoo, S. J. Hwang, J.-G. Lee, S.-C. Lee, T.-H. Lim, Y.-E. Sung, A. Wieckowski, and S.-K. Kim, "Promoting effects of La for improved oxygen reduction activity and high stability of Pt on Pt-La alloy electrodes," *Energy Environ. Sci.*, vol. 5, no. 6, pp. 7521–7525, 2012.

[75] H. Wang, M. Imura, Y. Nemoto, L. Wang, H. Y. Jeong, T. Yokoshima, O. Terasaki, and Y. Yamauchi, "Electrochemical Design of Mesoporous Pt-Ru Alloy Films with Various Compositions toward Superior Electrocatalytic Performance," *Chemistry A European Journal*, vol. 18, no. 41, pp. 13142–13148, 2012.

[76] S. J. Hwang, S. J. Yoo, S. Jang, T.-H. Lim, S. A. Hong, and S.-K. Kim, "Ternary Pt−Fe−Co Alloy Electrocatalysts Prepared by Electrodeposition: Elucidating the Roles of Fe and Co in the Oxygen Reduction Reaction," *The Journal of Physical Chemistry C*, vol. 115, no. 5, pp. 2483–2488, 2011.

[77] F. Maillard, P. A. Simonov, and E. R. Savinova, *Carbon Materials as Supports for Fuel Cell Electrocatalysts*, pp. 429–480. John Wiley & Sons, Inc., 2008.

[78] D. Banham, F. Feng, K. Pei, S. Ye, and V. Birss, "Effect of carbon support nanostructure on the oxygen reduction activity of Pt/C catalysts," *J. Mater. Chem. A*, vol. 1, no. 8, pp. 2812–2820, 2013.

[79] H. Yano, T. Akiyama, P. Bele, H. Uchida, and M. Watanabe, "Durability of Pt/graphitized carbon catalysts for the oxygen reduction reaction prepared by the nanocapsule method," *Phys. Chem. Chem. Phys.*, vol. 12, no. 15, pp. 3806–3814, 2010.

[80] W. Li, M. Waje, Z. Chen, P. Larsen, and Y. Yan, "Platinum nanopaticles supported on stacked-cup carbon nanofibers as electrocatalysts for proton exchange membrane fuel cell," *Carbon*, vol. 48, no. 4, pp. 995 – 1003, 2010.

[81] G. Girishkumar, K. Vinodgopal, and P. V. Kamat, "Carbon nanostructures in portable fuel cells: single-walled carbon nanotube electrodes for methanol oxidation and oxygen reduction," *The Journal of Physical Chemistry B*, vol. 108, no. 52, pp. 19960–19966, 2004.

[82] T. Matsumoto, T. Komatsu, K. Arai, T. Yamazaki, M. Kijima, H. Shimizu, Y. Takasawa, and J. Nakamura, "Reduction of Pt usage in fuel cell electrocatalysts with carbon nanotube electrodes," *Chem. Commun.*, vol. 0, no. 7, pp. 840–841, 2004.

[83] C. Kim, Y. J. Kim, Y. A. Kim, T. Yanagisawa, K. C. Park, M. Endo, and M. S. Dresselhaus, "High performance of cup-stacked-type carbon nanotubes as a Pt–Ru catalyst support for fuel cell applications," *Journal of Applied Physics*, vol. 96, no. 10, pp. 5903–5905, 2004.

[84] C. Huang, C. Li, and G. Shi, "Graphene based catalysts," *Energy Environ. Sci.*, vol. 5, no. 10, pp. 8848–8868, 2012.

[85] L. Dong, R. R. S. Gari, Z. Li, M. M. Craig, and S. Hou, "Graphene-supported platinum and platinum–ruthenium nanoparticles with high electrocatalytic activity for methanol and ethanol oxidation," *Carbon*, vol. 48, pp. 781–787, Mar. 2010.

[86] R. Kou, Y. Shao, D. Wang, M. H. Engelhard, J. H. Kwak, J. Wang, V. V. Viswanathan, C. Wang, Y. Lin, Y. Wang, I. a. Aksay, and J. Liu, "Enhanced activity and stability of Pt catalysts on functionalized graphene sheets for electrocatalytic oxygen reduction," *Electrochemistry Communications*, vol. 11, pp. 954–957, May 2009.

[87] B. Seger and P. V. Kamat, "Electrocatalytically Active Graphene-Platinum Nanocomposites. Role of 2-D Carbon Support in PEM Fuel Cells," *The Journal of Physical Chemistry C*, vol. 113, pp. 7990–7995, May 2009.

[88] H. Chang, S. H. Joo, and C. Pak, "Synthesis and characterization of mesoporous carbon for fuel cell applications," *J. Mater. Chem.*, vol. 17, no. 30, pp. 3078–3088, 2007.

[89] E. P. Ambrosio, M. A. Dumitrescu, C. Francia, C. Gerbaldi, and P. Spinelli, "Ordered Mesoporous Carbons as Catalyst Support for PEM Fuel Cells," *Fuel Cells*, vol. 9, no. 3, pp. 197–200, 2009.

[90] Y. Shao, J. Liu, Y. Wang, and Y. Lin, "Novel catalyst support materials for PEM fuel cells: current status and future prospects," *J. Mater. Chem.*, vol. 19, no. 1, pp. 46–59, 2009.

[91] K. Lee, J. Zhang, H. Wang, and D. P. Wilkinson, "Progress in the synthesis of carbon nanotube- and nanofiber-supported Pt electrocatalysts for PEM fuel cell catalysis," *Journal of Applied Electrochemistry*, vol. 36, pp. 507–522, 2006.

[92] A. H. Castro Neto, F. Guinea, N. M. R. Peres, K. S. Novoselov, and A. K. Geim, "The electronic properties of graphene," *Rev. Mod. Phys.*, vol. 81, pp. 109–162, Jan 2009.

[93] A. K. Geim and K. S. Novoselov, "The rise of graphene," *Nat Mater*, vol. 6, pp. 183–191, Mar. 2007.

[94] S. Stankovich, D. A. Dikin, G. H. B. Dommett, K. M. Kohlhaas, E. J. Zimney, E. A. Stach, R. D. Piner, S. T. Nguyen, and R. S. Ruoff, "Graphene-based composite materials," *Nature*, vol. 442, pp. 282–286, July 2006.

[95] A. A. Permyakova, B. Han, J. O. Jensen, N. J. Bjerrum, and Y. Shao-Horn, "Pt-Si Alloys as Alternative Bifunctional Catalysts for CO and Methanol Electro-Oxidation," *To be submitted to Journal of the American Chemical Society*, 2013.

[96] A. A. Permyakova, J. Suntivich, B. Han, J. O. Jensen, Q. F. Li, N. J. Bjerrum, and Y. Shao-Horn, "Bifunctional Pt-Si Alloys for Small Organic Molecule Electro-oxidation," *2012 MRS Fall Meeting & Exhibit conference, abstract, oral presentation, Boston, MA, USA*, November 2012.

[97] A. A. Permyakova, Q. F. Li, J. O. Jensen, and N. J. Bjerrum, "Poly(benzimidazole)functionalized graphene supported Pt electrocatalyst and its application in high temperature PEM fuel cell," *ECS 222nd Meeting (PRiME) conference, abstract, poster presentation, Honolulu, Hawaii, USA*, October 2012.

[98] A. A. Permyakova, J. O. Jensen, Q. F. Li, and N. J. Bjerrum, "Poly(benzimidazole)-functionalized graphene as a stable and durable support for PEM fuel cell electrocatalysts," *3rd CARISMA International Conference, abstract, poster presentation, Copenhagen, Denmark*, September 2012.

[99] P. A. A. I. by Charlotte Malasse, "Smil! Du er på," *DTU - Avisen, participation in interview for printed media*, January 2012. http://emagstudio.win.dtu.dk/E-books/DTU-Avisen/DTUavis0112/.

[100] D. Plackett, A. Siu, Q. F. Li, C. Pan, J. O. Jensen, S. F. Nielsen, A. A. Permyakova, and N. J. Bjerrum, "High temperature proton exchange membranes based on polybenzimidazole and clay composites for fuel cells," *Journal of Membrane Science*, vol. 383, 1-2, pp. 78–87, 2011.

[101] A. A. P. P. in video presentation of the PhD project, "Development of improved electrodes in high temperature PEM fuel cells," *PhD project for the DTU Chemistry PhD School Symposium 2011, Copenhagen, Denmark*, October 2011. http://www.youtube.com/watch?v=7Owp7MVKMOc.

[102] A. A. Permyakova, Q. F. Li, J. O. Jensen, and N. J. Bjerrum, "Development and Characterisation of Active and Durable Electrocatalysts for HT-PEM Fuel Cells 2," *Advanced Studies of Polymer Electrolyte Fuel Cells, The book of 4th International Summer School: book article, poster presentation*, pp. 96–98, Eds: S. Mitsushima, T. Araki, K. Ota, V. Hacker, M. Siebenhofer, Yokohama, Japan. Publisher: Graz University of Technology, September 2011. ISBN: 978-3-85125-170-8.

[103] J. O. Jensen, Q. Li, C. L. N. Vassiliev, A., C. Pan, A. A. Permyakova, and N. J. Bjerrum, "HT - PEMFC in Denmark," *PROCON Summer school, oral presentation, Changchun Institute of Applied Chemistry (CIAC) Chinese Academy of Sciences, Changchun, China*, August 2011.

[104] A. A. Permyakova, Q. Li, J. O. Jensen, and N. J. Bjerrum, "Development and Characterisation of Active and Durable Electrocatalysts for HT-PEM Fuel Cells," *Hydrogen + Fuel Cells 2011 conference, abstract, poster presentation, Vancouver, British Columbia, Canada*, May 2011.

[105] A. A. Permyakova, Q. F. Li, J. O. Jensen, and N. J. Bjerrum, "Half cell characteristics of high temperature PEM Fuel cell," *DTU Chemistry PhD School Symposium 2010, abstract, poster presentation, Gentofte Denmark*, November 2010.

[106] P. J. Goodhew, J. Humphreys, and B. Richard, *Electron microscopy and analysis*. Taylor & Francis, 2001.

[107] I. Chorkendorff and J. W. Niemantsverdriet, *Concepts of Modern Catalysis and Kinetics*. WILEY-VCH Verlag GmbH & Co., 2007.

[108] D. Pletcher, R. Greef, R. Peat, L. M. Peter, and J. Robinson, *Instrumental methods in electrochemistry*. Chichester, Horwood Publishing Limited, 2001.

[109] F. G. Will, "The Voltage Sweep Method Electronic Device for Producing Triangle Pulses and Ramps," *Journal of The Electrochemical Society*, vol. 112, no. 11, pp. 1157–1159, 1965.

[110] T. R. Ralph, G. A. Hards, J. E. Keating, S. A. Campbell, D. P. Wilkinson, M. Davis, J. St-Pierre, and M. C. Johnson, "Low Cost Electrodes for Proton Exchange Membrane Fuel Cells: Performance in Single Cells and Ballard Stacks," *Journal of The Electrochemical Society*, vol. 144, no. 11, pp. 3845–3857, 1997.

[111] K. H. Kangasniemi, D. A. Condit, and T. D. Jarvi, "Characterization of Vulcan Electrochemically Oxidized under Simulated PEM Fuel Cell Conditions," *Journal of The Electrochemical Society*, vol. 151, no. 4, pp. E125–E132, 2004.

[112] D. C. Papageorgopoulos, M. Keijzer, J. B. J. Veldhuis, and F. A. de Bruijn, "CO tolerance of Pd-rich platinum palladium carbon-supported electrocatalysts - Proton exchange membrane fuel cell applications," *Journal of the electrochemical society*, vol. 149, pp. A1400–A1404, November 2002.

[113] H. Siwek, W. Tokarz, P. Piela, and A. Czerwinski, "Electrochemical behavior of CO, CO_2 and methanol adsorption products formed on Pt-Rh alloys of various surface compositions," *Journal of Power Sources*, vol. 181, no. 1, pp. 24 – 30, 2008.

[114] D. A. Stevens, J. Harlow, R. J. Sanderson, C. W. Watson, T. J. Crowtz, J. R. Dahn, G. D. Vernstrom, L. L. Atanasoska, G. M. Haugen, and R. T. Atanasoski, "Rotating Disk Electrode Techniques Designed to Simulate Fuel Cell Startup/Shut-Down Transient Conditions," *ECS Transactions*, vol. 50, no. 2, pp. 1533–1538, 2013.

[115] J. Nikolic, E. Expósito, J. Iniesta, J. González-Garcia, and V. Montiel, "Theoretical Concepts and Applications of a Rotating Disk Electrode," *J. Chem. Educ.*, vol. 77, pp. 1191–, Sept. 2000.

[116] Y. Garsany, O. Baturina, K. E. Swider-Lyons, and S. S. Kocha, "Experimental methods for quantifying the activity of platinum electrocatalysts for the oxygen reduction reaction," *Analytical chemistry*, vol. 82, pp. 6321–8, Aug. 2010.

[117] K. J. J. Mayrhofer, D. Strmcnik, B. B. Blizanac, V. Stamenkovic, M. Arenz, and N. M. Markovic, "Measurement of oxygen reduction activities via the rotating disc electrode method: From Pt model surfaces to carbon-supported high surface area catalysts," *Electrochimica Acta*, vol. 53, no. 7, pp. 3181 – 3188, 2008.

[118] V. Stamenkovic, T. J. Schmidt, P. N. Ross, and N. M. Markovic, "Surface Composition Effects in Electrocatalysis: Kinetics of Oxygen Reduction on Well-Defined Pt_3Ni and Pt_3Co Alloy Surfaces," *The Journal of Physical Chemistry B*, vol. 106, no. 46, pp. 11970–11979, 2002.

[119] K.-W. Nam, J. Song, K.-H. Oh, M.-J. Choo, H. Park, J.-K. Park, and J. Choi, "Perfluorosulfonic acid-functionalized Pt/graphene as a high-performance oxygen reduction reaction catalyst for proton exchange membrane fuel cells," *Journal of Solid State Electrochemistry*, vol. 17, no. 3, pp. 767–774, 2013.

[120] M. Okamoto, T. Fujigaya, and N. Nakashima, "Design of an assembly of poly(benzimidazole), carbon nanotubes, and Pt nanoparticles for a fuel-cell electrocatalyst with an ideal interfacial nanostructure," *Small (Weinheim an der Bergstrasse, Germany)*, vol. 5, pp. 735–40, Mar. 2009.

[121] Y. Wang, J. Ren, K. Deng, L. Gui, and Y. Tang, "Preparation of Tractable Platinum, Rhodium, and Ruthenium Nanoclusters with Small Particle Size in Organic Media," *Chemistry of Materials*, vol. 12, pp. 1622–1627, June 2000.

[122] M. R. Berber, T. Fujigaya, K. Sasaki, and N. Nakashima, "Remarkably Durable High Temperature Polymer Electrolyte Fuel Cell Based on Poly(vinylphosphonic acid)-doped Polybenzimidazole," *Sci. Rep.*, vol. 3, May 2013.

[123] D. Larcher and R. Patrice, "Preparation of Metallic Powders and Alloys in Polyol Media: A Thermodynamic Approach," *Journal of Solid State Chemistry*, vol. 154, no. 2, pp. 405 – 411, 2000.

[124] P. Musto, F. Karasz, and W. MacKnight, "Hydrogen bonding in polybenzimidazole/polyimide systems: a Fourier-transform infra-red investigation using low-molecular-weight monofunctional probes," *Polymer*, vol. 30, no. 6, pp. 1012 – 1021, 1989.

[125] U. A. Paulus, T. J. Schmidt, H. A. Gasteiger, and R. J. Behm, "Oxygen reduction on a high-surface area Pt/Vulcan carbon catalyst: a thin-film rotating ring-disk electrode study," *Journal of Electroanalytical Chemistry*, vol. 495, pp. 134–145, Jan. 2001.

[126] T. J. Schmidt, H. A. Gasteiger, G. D. Stäb, P. M. Urban, D. M. Kolb, and R. J. Behm, "Characterization of High-Surface-Area Electrocatalysts Using a Rotating Disk Electrode Configuration," *Journal of The Electrochemical Society*, vol. 145, no. 7, pp. 2354–2358, 1998.

[127] M. J. Larsen, *Ivvestigation of alternative carbon materials for fuel-cell catalyst support*. PhD thesis, 2010.

[128] H. A. Gasteiger, N. Markovic, P. N. Ross, and E. J. Cairns, "Carbon monoxide electrooxidation on well-characterized platinum-ruthenium alloys," *The Journal of Physical Chemistry*, vol. 98, no. 2, pp. 617–625, 1994.

[129] S. W. Lee, S. Chen, W. Sheng, N. Yabuuchi, Y.-T. Kim, T. Mitani, E. Vescovo, and Y. Shao-Horn, "Roles of Surface Steps on Pt Nanoparticles in Electro-oxidation of Carbon Monoxide and Methanol," *Journal of the American Chemical Society*, vol. 131, no. 43, pp. 15669–15677, 2009.

[130] T. H. M. Housmans and M. T. M. Koper, "Methanol Oxidation on Stepped Pt[n(111) x (110)] Electrodes: A Chronoamperometric Study," *The Journal of Physical Chemistry B*, vol. 107, no. 33, pp. 8557–8567, 2003.

[131] S. Lai, N. Lebedeva, T. Housmans, and M. Koper, "Mechanisms of Carbon Monoxide and Methanol Oxidation at Single-crystal Electrodes," *Topics in Catalysis*, vol. 46, no. 3-4, pp. 320–333, 2007.

[132] G. Chen, Q. Yuan, H. Li, and S. Li, "CO selective oxidation in a microchannel reactor for PEM fuel cell," *Chemical Engineering Journal*, vol. 101, pp. 101 – 106, 2004.

[133] Y. J. Zhang, A. Maroto-Valiente, I. Rodriguez-Ramos, Q. Xin, and A. Guerrero-Ruiz, "Synthesis and characterization of carbon black supported Pt-Ru alloy as a model catalyst for fuel cells," *Catalysis Today*, vol. 93-95, no. 0, pp. 619 – 626, 2004.

[134] M. Arenz, K. J. J. Mayrhofer, V. Stamenkovic, B. B. Blizanac, T. Tomoyuki, P. N. Ross, and N. M. Markovic, "The Effect of the Particle Size on the Kinetics of CO Electrooxidation on High Surface Area Pt Catalysts," *Journal of the American Chemical Society*, vol. 127, no. 18, pp. 6819–6829, 2005. PMID: 15869305.

[135] J. N. Tiwari, T.-M. Chen, F.-M. Pan, and K.-L. Lin, "Ordered silicon nanocones as a highly efficient platinum catalyst support for direct methanol fuel cells," *Journal of Power Sources*, vol. 182, pp. 510–514, Aug. 2008.

[136] B. Liu, J. H. Chen, X. X. Zhong, K. Z. Cui, H. H. Zhou, and Y. F. Kuang, "Preparation and electrocatalytic properties of Pt-O_2 nanocatalysts for ethanol electrooxidation," *Journal of Colloid and Interface Science*, vol. 307, no. 1, pp. 139 – 144, 2007.

[137] X. Su, K. LÜ, Y. Chang, Y. Zhang, and C. Wang, "Immersion Deposition of Pt Nanoparticles on Porous Silicon for Methanol Oxidation," *Chinese Journal of Chemistry*, vol. 27, no. 9, pp. 1682–1686, 2009.

[138] J. Cechal and T. Sikola, "A study of the formation and oxidation of PtSi by SR-PES," *Surface Science*, vol. 600, no. 20, pp. 4717 – 4722, 2006.

[139] D. S. Strmcnik, D. V. Tripkovic, D. van der Vliet, K.-C. Chang, V. Komanicky, H. You, G. Karapetrov, J. P. Greeley, V. R. Stamenkovic, and N. M. Markovic, "Unique Activity of Platinum Adislands in the CO Electrooxidation Reaction," *Journal of the American Chemical Society*, vol. 130, no. 46, pp. 15332–15339, 2008.

[140] R. Parsons and T. VanderNoot, "The oxidation of small organic molecules: A survey of recent fuel cell related research," *Journal of Electroanalytical Chemistry and Interfacial Electrochemistry*, vol. 257, no. 1-2, pp. 9 – 45, 1988.

[141] J. D. Morse, A. F. Jankowski, R. T. Graff, and J. P. Hayes, "Novel proton exchange membrane thin-film fuel cell for microscale energy conversion," vol. 18, pp. 2003–2005, AVS, 2003(2000).

[142] S. Tominaka, H. Nishizeko, S. Ohta, and T. Osaka, "On-chip fuel cells for safe and high-power operation: investigation of alcohol fuel solutions," *Energy Environ. Sci.*, vol. 2, pp. 849–852, 2009.

[143] S. Tominaka, S. Ohta, T. Osaka, and R. Alkire, "Prospects of on-chip fuel cell performance: improvement based on numerical simulation," *Energy Environ. Sci.*, vol. 4, pp. 162–171, 2011.

[144] V. A. Grinberg and A. M. Skundin, "Microfuel cells: Modern state and future development (Review)," *Russian Journal of Electrochemistry*, vol. 46, no. 9, pp. 963–978, 2010.

[145] R. G. Hockaday, "Micro-fuel cell power devices," 2001.

[146] S. Tominaka, M. Shigeto, H. Nishizeko, and T. Osaka, "Synthesis of mesoporous PtCu film modified with Ru submonolayer as catalyst for methanol electrooxidation," *Chem. Commun.*, vol. 46, pp. 8989–8991, 2010.

[147] A. Kloke, C. Kohler, R. Gerwig, R. Zengerle, and S. Kerzenmacher, "Cyclic Electrodeposition of PtCu Alloy: Facile Fabrication of Highly Porous Platinum Electrodes," *Advanced Materials*, vol. 24, no. 21, pp. 2916–2921, 2012.

[148] M. P. Lepselter, "Beam-Lead Technology," *Bell System Technical Journal*, vol. 45, pp. 233–253, 1966.

[149] T. Kawamura, D. Shinoda, and H. Muta, "Oriented growth of the interfacial PtSi layer or between Pt and Si ," *Applied Physics Letters*, vol. 11, no. 3, pp. 101–103, 1967.

[150] A. Hiraki, E. Lugujjo, M.-A. Nicolet, and J. W. Mayer, "Low-temperature migration of silicon through metal films importance of silicon-metal interface," *physica status solidi (a)*, vol. 7, no. 2, pp. 401–406, 1971.

[151] J. Drobek, R. C. Sun, and T. C. Tisone, "Interdiffusion and compound formation in thin films of Pd or Pt on si single crystals," *physica status solidi (a)*, vol. 8, no. 1, pp. 243–248, 1971.

[152] D. Shinoda, "Physico-chemical studies of platinum-silicon interfaces," *The Physico-Chemical Society of Japan*, vol. 42, pp. 94–102, 1972.

[153] S. P. Murarka, E. Kinsbron, D. B. Fraser, J. M. Andrews, and E. J. Lloyd, "High temperature stability of PtSi formed by reaction of metal with silicon or by cosputtering," *Journal of Applied Physics*, vol. 54, no. 12, pp. 6943–6951, 1983.

[154] V. Miikkulainen, M. Leskela, M. Ritala, and R. L. Puurunen, "Crystallinity of inorganic films grown by atomic layer deposition: Overview and general trends," *Journal of Applied Physics*, vol. 113, no. 2, p. 021301, 2013.

[155] T. Aaltonen, M. Ritala, T. Sajavaara, J. Keinonen, and M. Leskela, "Atomic Layer Deposition of Platinum Thin Films," *Chemistry of Materials*, vol. 15, no. 9, pp. 1924–1928, 2003.

[156] S. Sun, G. Zhang, N. Gauquelin, N. Chen, J. Zhou, S. Yang, W. Chen, X. Meng, D. Geng, M. N. Banis, R. Li, S. Ye, S. Knights, G. A. Botton, T.-K. Sham, and X. Sun, "Single-atom Catalysis Using Pt/Graphene Achieved through Atomic Layer Deposition," *Sci. Rep.*, vol. 3, pp. –, 2013.

[157] R. J. Nemanich, T. W. Sigmon, N. M. Johnson, M. D. Moyer, and S. S. Lau, "Raman Spectroscopic Evaluation of Silicides Formed with A Scanned Electron Beam," *MRS Online Proceedings Library*, vol. 1, 0 1980.

[158] J. C. Tsang, R. Matz, Y. Yokota, and G. W. Rubloff, "Raman spectroscopy of silicide formation at the Pt/crystalline Si interface," *Journal of Vacuum Science & Technology A: Vacuum, Surfaces, and Films*, vol. 2, no. 2, pp. 556–560, 1984.

[159] J. C. Tsang, Y. Yokota, R. Matz, and G. Rubloff, "Raman spectroscopy of PtSi formation at the Pt/Si(100) interface," *Applied Physics Letters*, vol. 44, no. 4, pp. 430–432, 1984.

[160] K. A. Stoerzinger, M. Risch, J. Suntivich, W. M. Lu, J. Zhou, M. D. Biegalski, H. M. Christen, Ariando, T. Venkatesan, and Y. Shao-Horn, "Oxygen electrocatalysis on (001)-oriented manganese perovskite films: Mn valency and charge transfer at the nanoscale," *Energy Environ. Sci.*, vol. 6, pp. 1582–1588, 2013.

[161] J. Suntivich, Z. Xu, C. E. Carlton, J. Kim, B. Han, S. W. Lee, N. Bonnet, N. Marzari, L. F. Allard, H. A. Gasteiger, K. Hamad-Schifferli, and Y. Shao-Horn, "Surface Composition Tuning of Au-Pt Bimetallic Nanoparticles for Enhanced Carbon Monoxide

and Methanol Electro-oxidation," *Journal of the American Chemical Society*, vol. 135, no. 21, pp. 7985–7991, 2013.

[162] H. A. Gasteiger, N. Markovic, P. N. Ross, and E. J. Cairns, "Temperature-Dependent Methanol Electro-Oxidation on Well-Characterized Pt-Ru Alloys," *Journal of The Electrochemical Society*, vol. 141, no. 7, pp. 1795–1803, 1994.

[163] A. V. Tripkovic, K. D. Popovic, B. N. Grgur, B. Blizanac, P. N. Ross, and N. M. Markovic, "Methanol electrooxidation on supported Pt and PtRu catalysts in acid and alkaline solutions," *Electrochimica Acta*, vol. 47, no. 22–23, pp. 3707 – 3714, 2002.

[164] D. Strmcnik, M. Uchimura, C. Wang, R. Subbaraman, N. Danilovic, van der Vliet Dennis, A. P. Paulikas, V. R. Stamenkovic, and N. M. Markovic, "Improving the hydrogen oxidation reaction rate by promotion of hydroxyl adsorption," *Nat Chem*, vol. 5, pp. 300–306, Apr. 2013.

A major challenge facing our planet today relates to the raising of energy demands and directly connected to population growth, which recently surpassed 7 billion of people for the first time in the world history and prognoses to reach 9 billion by 2040. Expanding energy demands (35% by 2040) put pressure on the fossil fuel resources on earth and cause enormous amounts of gas emissions such as SO2, NOx, CO2. Together, these factors are major contributors to eco-system degradation. Thus, alternative sources of energy have to be found. The key energy solution of the future is widely regarded to fuel cells.

Fuel cells have number of benefits such as: low to zero emissions, high efficiency, and wide range of applications, starting from micro-devises up to, for example, cars or space ships. It is also quite and can eventually substitute batteries. The type of fuel cell is defined by fuel type, catalysts or membranes used. Proton exchange electrolyte (PEMFC) and methanol (DMFC) fuel cells use hydrogen or methanol as a fuel and work in the range of 0 to 200°C. To facilitate the electrochemical reactions on the cathode side (oxygen reduction reaction) and on the anode side (methanol electrooxidation reaction), a catalyst layer used.

The state-of-the-art catalyst for these reactions is platinum based. It is highly desirable to increase a catalyst activity and stability towards the severe electrochemical conditions of these reactions to minimize the cost and maximize the life time of a fuel cell. This thesis describes investigations conducted for supported nano-particulate, bulk and thin film electrocatalysts used in PEMFCs and DMFCs. The effects of different factors and conditions on the reactions involved in oxygen reduction, carbon monoxide and methanol electro-oxidation reactions are explored.

The electrochemical and physiochemical characterization exploring the activity, stability and durability of electrocatalsysts is presented.

Department of Energy Conversion and Storage
Technical University of Denmark
Risø Campus
Frederiksborgvej 399
4000 Roskilde
Denmark
www.ecs.dtu.dk

ISBN 978-87-92986-13-9